**UNIVERSIDADE FEDERAL DE JUIZ DE FORA**

**FACULDADE DE ENGENHARIA**

**PROGRAMA DE PÓS-GRADUAÇÃO EM MODELAGEM COMPUTACIONAL**

**Jhuan Barbosa da Silva e Cedro**

# Mathematical and Computational Analysis of Mechanistic Models for Foam Flow in Porous Media

Juiz de Fora

2025

**Jhuan Barbosa da Silva e Cedro**

# Mathematical and Computational Analysis of Mechanistic Models for Foam Flow in Porous Media

Tese apresentada ao Programa de Pós-Graduação em Modelagem Computacional da Universidade Federal de Juiz de Fora, como requisito parcial à obtenção do título de Doutor em Modelagem Computacional.

Orientador: Grigori Chapiro

Juiz de Fora

2025

Ficha catalográfica elaborada através do Modelo Latex do CDC da UFJF
com os dados fornecidos pelo autor

Cedro, Jhuan Barbosa da Silva.
Mathematical and Computational Analysis of Mechanistic Models for Foam Flow in Porous Media / Jhuan Barbosa da Silva e Cedro. – 2025.
108 f. : il.

Orientador: Grigori Chapiro
Tese (Doutorado) – Universidade Federal de Juiz de Fora, Faculdade de Engenharia. Programa de Pós-Graduação em Modelagem Computacional, 2025.

1. Escoamento em meios porosos. 2. Espumas. 3. Ondas viajantes. 4. Fluido não newtoniano. 5. Permeabilidade. I. Chapiro, Grigori, orient. II. Título.

**Jhuan Barbosa da Silva e Cedro**

**Mathematical and Computational Analysis of Mechanistic Models for Foam Flow in Porous Media**

Tese apresentada ao Programa de Pós-graduação em Modelagem Computacional da Universidade Federal de Juiz de Fora como requisito parcial à obtenção do título de Doutor em Modelagem Computacional. Área de concentração: Modelagem Computacional.

Aprovada em 20 de março de 2025.

BANCA EXAMINADORA

**Prof. Dr. Grigori Chapiro** - Orientador
Universidade Federal de Juiz de Fora

**Prof. Dr. William R. Rossen**
Delft University of Technology, Países Baixos

**Prof. Dr. Anthony R. Kovscek**
Stanford University, EUA

**Dr. Vinicius Luiz Santos Silva**
Imperial College London, Reino Unido

**Dr. Weslley S. Pereira**
National Renewable Energy Laboratory, EUA

Juiz de Fora, 13/03/2025.

Documento assinado eletronicamente por **Anthony R Kovscek**, **Usuário Externo**, em 20/03/2025, às 15:03, conforme horário oficial de Brasília, com fundamento no § 3º do art. 4º do Decreto nº 10.543, de 13 de novembro de 2020.

Documento assinado eletronicamente por **Grigori Chapiro**, **Professor(a)**, em 20/03/2025, às 15:06, conforme horário oficial de Brasília, com fundamento no § 3º do art. 4º do Decreto nº 10.543, de 13 de novembro de 2020.

Documento assinado eletronicamente por **Vinicius Luiz Santos Silva**, **Usuário Externo**, em 20/03/2025, às 15:24, conforme horário oficial de Brasília, com fundamento no § 3º do art. 4º do Decreto nº 10.543, de 13 de novembro de 2020.

Documento assinado eletronicamente por **William R. Rossen**, **Usuário Externo**, em 20/03/2025, às 18:42, conforme horário oficial de Brasília, com fundamento no § 3º do art. 4º do Decreto nº 10.543, de 13 de novembro de 2020.

Documento assinado eletronicamente por **Weslley da Silva Pereira**, **Usuário Externo**, em 20/03/2025, às 20:00, conforme horário oficial de Brasília, com fundamento no § 3º do art. 4º do Decreto nº 10.543, de 13 de novembro de 2020.

A autenticidade deste documento pode ser conferida no Portal do SEI-Ufjf (www2.ufjf.br/SEI) através do ícone Conferência de Documentos, informando o código verificador **2289857** e o código CRC **B387E47D**.

## ACKNOWLEDGMENTS

I would like to express my deepest gratitude to my family for their unconditional support and for always believing in me. To my wife, for her constant presence, love, and wisdom, and for being by my side throughout every stage of this journey. To my friends for their companionship and support during my years at university.

I also want to thank the professors of the Graduate Program in Computational Modeling, who were not only academic guides but also friends who shared their experience and wisdom with patience and dedication. A special thank you to my advisor for his attention, patience, and dedication, beyond guiding this work, offering invaluable advice and encouragement at every step of my academic journey.

Finally, I would like to thank the members of my thesis committee, who greatly contributed to the development of this work through their valuable insights and constructive feedback. Their expertise and thoughtful suggestions were crucial in refining this research and elevating its quality.

I gratefully acknowledge support from Shell Brasil through the project "Avançando na modelagem matemática e computacional para apoiar a implementação da tecnologia 'Foam-assisted WAG' em reservatórios do Pré-sal" (ANP 23518-4) at UFJF and the strategic importance of the support given by ANP through the R&D levy regulation.

**RESUMO**

Há um interesse renovado no estudo do escoamento de espuma em meios porosos, especialmente em aplicações de engenharia ambiental e de petróleo. Diversas observações experimentais relatam perfis de saturação que mantêm uma forma consistente durante o deslocamento no meio poroso, motivando a investigação de soluções na forma de ondas viajantes para modelos de espuma. Neste trabalho, analisamos três modelos de escoamento de espuma com abordagens distintas para reologia e balanço de bolhas, incluindo um modelo não newtoniano para o qual demonstramos a existência de soluções em onda viajante. Validamos nossa solução semi-analítica por meio de simulações numéricas, que apresentaram boa concordância com os dados experimentais. Mostramos que, para meios homogêneos em regime de espuma forte, todos os modelos resultam na mesma solução quando ajustados para condições experimentais típicas. As diferenças entre os modelos foram exploradas por meio de simulações bidimensionais em campos heterogêneos de permeabilidade, revelando uma divergência significativa na descrição da distribuição de bolhas. O modelo que incorpora uma taxa de destruição da espuma dependente da permeabilidade apresenta maior densidade de bolhas em regiões mais permeáveis, em conformidade com observações reportadas na literatura. Apesar dessas diferenças, todos os modelos preveem com precisão o tempo de *breakthrough*, as curvas de produção e o formato da frente de gás. Nossos resultados confirmam a aplicabilidade da abordagem de onda viajante para obtenção de soluções semianalíticas em modelos de espuma newtonianos e não newtonianos e fornecem uma ferramenta para auxiliar na seleção de modelos apropriados para aplicações específicas.

Palavras-chave: Escoamento em meios porosos. Espumas. Ondas viajantes. Fluido não newtoniano. Permeabilidade.

**ABSTRACT**

There has been a renewed interest in studying foam flow in porous media, particularly in environmental and petroleum engineering applications. Several experimental observations reported saturation profiles maintaining a consistent shape during displacement through the medium, motivating the investigation of solutions for foam models in the form of traveling waves. In this work, we analyze three foam flow models with distinct approaches to rheology and bubble balance, including a non-Newtonian model for which we demonstrate the existence of traveling wave solutions. We validated our semi-analytical solution with numerical simulations, and both agreed well with the experimental data. We show that, for homogeneous media under the strong foam regime, all models yield the same solution when fitted to typical experimental conditions. We explored model differences through two-dimensional simulations in heterogeneous permeability fields, revealing a significant divergence in describing bubble distribution. The model featuring a permeability-dependent foam destruction rate exhibits higher bubble density in more permeable regions, consistent with observations reported in the literature. Despite these differences, all models accurately predict breakthrough time, production curves, and the shape of the foamed gas front. Our findings confirm the applicability of the traveling wave approach in obtaining semi-analytical solutions for Newtonian and non-Newtonian foam models and provide a tool to aid in selecting appropriate models for specific applications.

Keywords: Flow in porous media. Foam. Traveling waves. Non-Newtonian fluid. Permeability.

## LIST OF FIGURES

## LIST OF ABBREVIATIONS AND ACRONYMS

| | |
|---|---|
| CMC | Critical micelle concentration |
| EOR | Enhanced Oil Recovery |
| FAWAG | Foam-assisted water-alternating-gas |
| ODE | Ordinary Differential Equation |
| PDE | Partial Differential Equation |
| WAG | Water-alternating-gas |

## LIST OF SYMBOLS

### Foam modeling

| | |
|---|---|
| $w$, $g$, $i$ | Subscripts for phases water, gas, and $i$ |
| $S_w$, $S_g$, $S_i$ | Saturations |
| $S_{wc}, S_{gr}, S_{ir}$ | Residual saturations |
| $S_w^*$ | Limiting water saturation |
| $f_w$, $f_g$, $f_i$ | Fractional flow |
| $\lambda_w$, $\lambda_g$, $\lambda_i$ | Phase mobilities |
| $\lambda_{rw}, \lambda_{rg}, \lambda_{ri}$ | Relative phase mobilities |
| $\mu_w$, $\mu_g$, $\mu_i$ | Phase viscosities |
| $\mu_f$ | Foamed gas apparent viscosity |
| $\mu_{\text{app}}$ | Flow apparent viscosity |
| $p_w$, $p_g$, $p_i$ | Partial phase pressures |
| $P_c$ | Capillary pressure |
| $P_c^*$ | Limiting capillary pressure |
| $n_f$ | Foam texture |
| $n_{\max}$ | Maximum foam texture |
| $n_D$ | Dimensionless foam texture |
| $n_D^{\text{LE}}$ | Dimensionless foam texture at local equilibrium |
| $\phi$ | Porosity |
| $\mathbf{k}$, $k$ | Permeability |
| $k_{rw}, k_{rg}, k_{ri}$ | Relative permeabilities |
| $k_{rw}^0$, $k_{rg}^0$ | Relative permeability end-point constants |
| $n_w$, $n_g$ | Relative permeability exponent constants |
| $\mathbf{u}$, $u$ | Total superficial velocity |
| $u_w$, $u_g$, $u_i$ | Phase superficial velocities |
| $\mathbf{v}$ , $v$ | Total interstitial velocity |
| $\mathbf{v}_i$, $v_w$, $v_g$ | Phase interstitial velocities |
| $\Phi$ | Foam balance source term |
| $r_g$, $r_c$ | Foam generation and destruction rates |
| $\sigma_{wg}$ | Surface tension between water and gas |
| $\alpha$ | Foam rheological parameter |
| $\eta$ | Variable of the traveling wave system |
| $v$ | Traveling wave propagation velocity |

### Model A

| | |
|---|---|
| $A$ | Sharpness parameter |
| $K_c$ | Foam kinetic parameter |
| $C_{\text{MRF}}$ | Constant of mobility reduction factor |

## LIST OF SYMBOLS

### Model B

| | |
|---|---|
| $X_f, X_t$ | Flowing and trapped gas fraction |
| $X_{t,\max}$ | Maximum trapped gas fraction |
| $\beta$ | Gas trapping parameter |
| $k_1^0, k_{-1}^0$ | Generation and destruction constants |

### Model C

| | |
|---|---|
| $K_g\,, K_d$ | Generation and destruction constants |
| $\omega$ | Pore-size-distribution parameter |
| $\theta$ | Contact angle between wetting phase and porous walls |
| $r$ | Mean pore radius |
| $\xi$ | Capillary pressure coefficient |

## CONTENTS

# 1 INTRODUCTION

The study of foam flow in porous media primarily finds application in environmental remediation and reservoir engineering. In soil remediation, foam mobilizes hydrophobic contaminants (Hirasaki et al., 1997; Mulligan and Eftekhari, 2003; Wang and Mulligan, 2004; Couto et al., 2009) and redirects groundwater flow to avoid contaminated areas (Davarzani et al., 2021, 2022). Foam is also utilized in advanced agricultural practices for delivering liquid fertilizers and agrochemicals (Shojaei et al., 2022), as well as for improving the stability of solid waste landfills (Hu et al., 2023).

In the petroleum industry, foam is a valuable tool for enhancing the sweep efficiency of oil recovery in reservoirs. Reservoirs are porous rock formations filled with hydrocarbons, and maximizing oil recovery from these formations is challenging. Oil recovery methods are generally classified into three main types (Lake, 1989). Primary recovery relies on the reservoir's natural pressure, typically recovering around 15% to 30% of the total oil in place (Chen et al., 2006). Secondary recovery techniques, such as water or gas flooding, help maintain reservoir pressure and extract additional oil. Tertiary or enhanced oil recovery (EOR) methods are more advanced and include techniques such as thermal processes – *in situ* combustion (Chapiro et al., 2012; Chapiro and Bruining, 2015), electromagnetic heating (Abernethy, 1976; Paz et al., 2017), and steam injection (Willman et al., 1961; Willhite, 1967) – as well as chemical methods like foam injection (Kovscek and Radke, 1994; Rossen, 1996; Ma et al., 2015; Hematpur et al., 2018), which is the focus of this work.

Figure 1.1 – Representation of a secondary recovery in oil reservoir.

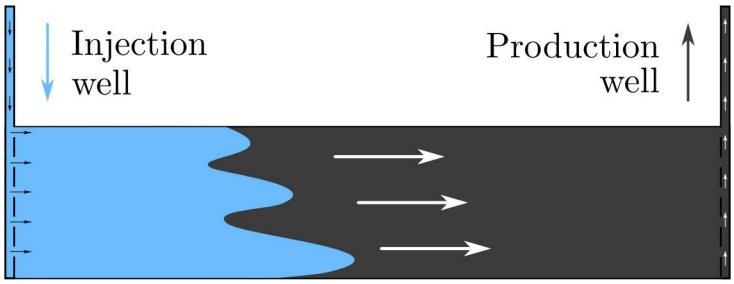


Source: Elaborated by the author (2020).

One of the challenges associated with multiphase flow in porous media is the fluid dynamics involved in the process. In a porous medium, when a more mobile fluid displaces a less mobile fluid, the more mobile fluid tends to flow through the least resistant pathways, forming channels within the less mobile phase. This phenomenon is called fingering, as the advancing front exhibits finger-like structures as it propagates through the media. This phenomenon can significantly affect the efficiency of fluid displacement efficiency in processes like enhanced oil recovery or groundwater remediation. Figure 1.1 illustrates

water flooding in an oil reservoir for EOR applications, where oil trapped between the gas fingers is not displaced and remains in the reservoir. Another issue to consider in oil recovery applications is the density of the fluids involved in the process. A less dense fluid injected into the reservoir tends to rise to the top due to the gravity effect, leaving behind a layer of oil at the bottom. Similarly, fluids injected that are denser than those present in the medium tend to move to lower regions of the reservoir. This phenomenon is called gravity override and becomes more pronounced as the reservoir thickness increases and the distance between the injection and production wells grows. As with fingering, when the injected fluid reaches the production well, the efficiency of the process decreases significantly (Lake, 1989; Bear, 2018).

Some EOR techniques aim to reduce the mobility of the injected fluid to avoid sweep efficiency loss. One of them is water-alternating-gas (WAG) injection, which alternates between injecting water (denser than oil) and gas (less dense than oil) into the reservoir to yield a more uniform sweep, improving recovery efficiency. One strategy adopted in WAG techniques is the re-injection of carbon dioxide ($CO_2$), which is present in high concentrations in many oil reservoirs. For example, some Brazilian pre-salt fields re-inject about 45% of produced $CO_2$ (Ministry of Mines and Energy et al., 2020). This technique reduces greenhouse gas emissions, one of the main goals of the Paris Agreement, which Brazil signed in 2016 (United Nations Framework Convention on Climate Change, 2020; Ministry of the Environment, 2020). Additionally, reducing gas mobility makes foams highly useful for carbon dioxide sequestration in natural rock formations (Rossen et al., 2024), which also helps mitigate gas emissions by trapping them underground.

Even with superior efficiency compared to conventional injection techniques, WAG methods are still limited by the gas's high mobility and low density. One option that has been studied is to inject surfactant diluted in the aqueous phase so that the flow within the porous medium creates foam, hindering the gas flow and reducing its mobility (Ma et al., 2015). This strategy is frequently referred to in the literature as foam injection or foam-assisted WAG (FAWAG). Figure 1.2 illustrates the efficiency of foam injection, through which the reservoir is swept more uniformly compared to, for example, gas injection. The development of the injection techniques mentioned motivates the study of multiphase flow dynamics in porous media and, in this particular work, the study of foam flow. While the presence of oil and other nonaqueous phase liquids can significantly alter foam dynamics, studying the displacement of water and foamed gas is a foundational scenario for all the above-mentioned applications and is the focus of this work.

The necessity of precisely describing the behavior of foam in porous media has led to the development of various mathematical models. Comprehensive reviews of these models are available in the works by Ma et al. (2014a) and by Hematpur et al. (2018). Equilibrium-type models consider that foam generation and destruction rates are equal,

Figure 1.2 – Representation of a reservoir comparing recovering through gas injection versus foam injection.

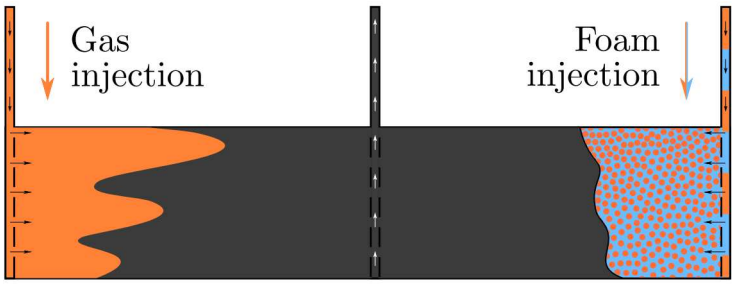


Source: Cedro and Chapiro (2024).

*i.e.*, foam is always in local equilibrium (LE). These models typically feature an algebraic equation describing foam texture or an implicit-texture approach. In the latter, foam effects are represented by a mobility reduction factor dependent on flow parameters, such as phase saturations (Hematpur et al., 2018). Implicit-texture models are commonly employed in most commercial simulators – *e.g.*, STARS (CMG, 2019), UTCHEM (Cheng et al., 2000), and ECLIPSE (Schlumberger, 2010). In contrast, mechanistic (or population-balance) models describe foam texture using an independent variable governed by generation and coalescence rates, as in the models presented by Falls et al. (1988); Kovscek et al. (1995); Zitha and Du (2010); Kam (2008); Ashoori et al. (2011). This characteristic makes mechanistic models more complex and accurate when describing transient scenarios (Kam et al., 2007; Hematpur et al., 2018).

The mathematical modeling of foam displacement is challenging due to the complexity of its governing partial differential equations (PDEs), which often prevent the derivation of analytical solutions. As a result, researchers commonly use numerical methods to obtain approximate solutions for these models. One approach to address specific PDEs is to search for solutions in the form of traveling waves, which are static profiles that propagate over time. This method introduces a symmetry that reduces the problem to a system of ordinary differential equations (ODEs) connecting two equilibrium states (Volpert et al., 2000; Ghazaryan et al., 2022). Several studies have applied this theory to specific EOR methods (Rossen and Bruining, 2007; Rossen et al., 2011; Bruining and Van Duijn, 2000; Chapiro and Bruining, 2015). Experimental studies have observed foam displacement through porous media as a piston-like shape, with water saturation profiles maintaining this form (Chen et al., 2010; Simjoo and Zitha, 2015; Janssen et al., 2020). These findings motivated the search for analytical solutions in the form of traveling waves for foam flow in porous media (Ashoori et al., 2011; Cedro et al., 2019; Lozano et al., 2021, 2022; Vásquez et al., 2022; Zavala et al., 2022).

Additionally, foam flow in porous media was reported as non-Newtonian by Bretherton (1961) and later by several authors (Marsden and Khan, 1966; Heller and Kunta-

mukkula, 1987; Falls et al., 1989; Rossen, 1991; Alvarez et al., 2001; Fernø et al., 2016). Hirasaki and Lawson (1985) proposed a shear-thinning formulation for foam's apparent viscosity. In the context of fractional flow, this formula defines foam viscosity implicitly, as it depends on gas velocity, which itself is a function of foam viscosity. That implicit relation makes the traveling wave analysis challenging. Pereira and Chapiro (2023) addressed this issue by expressing foam viscosity explicitly through a cubic equation, enabling the authors to obtain traveling wave solutions for a non-Newtonian foam model in local equilibrium. In the first part of this work, we derive a traveling wave solution for the foam flow model proposed by (Kovscek et al., 1995; Chen et al., 2010), which describes foam as a shear-thinning fluid following the formulation by Hirasaki et al. (1997). The semi-analytical solution profiles closely align with the experimental data from Chen et al. (2010), reproducing the same wavefront propagation velocity. This study was published in (Cedro and Chapiro, 2022, 2024).

Despite the variety of approaches to modeling foam flow, several validated foam models yield similar solutions when describing strong foam flow, typically exhibiting a piston-like saturation profile. Lotfollahi et al. (2016) calibrated multiple implicit-texture and mechanistic foam models using experimental data from Moradi-Araghi et al. (1997) and Alvarez et al. (2001), demonstrating that these models effectively capture the steady-state mobility of strong foam. In the field of analytical solutions, Ashoori et al. (2011) conducted a traveling wave analysis for their first-order kinetic model, using parameters fitted to the experimental data from Persoff et al. (1989), and the model by Kam (2008). Expanding on this, Lozano et al. (2021) classified all possible traveling wave solutions of the first-order kinetic model (for a given set of parameters) based on the equilibria of the system's ODEs, presenting the classification as a function of upstream saturation and the model's generation rate coefficient. In a subsequent study (Lozano et al., 2022), we explored how simplifications in foam displacement through capillary pressure affected the results. Pereira and Chapiro (2023) explored traveling wave solutions in a non-Newtonian adaptation of the model by Ashoori et al. (2011), incorporating the shear-thinning behavior described by Hirasaki and Lawson (1985). Zavala et al. (2022) analyzed traveling wave solutions for a Newtonian variation of the model by Zitha and Du (2010), using experimental data from Simjoo and Zitha (2015) and classifying traveling wave solutions. Building on these contributions, Fritis et al. (2022) demonstrated that the models proposed by Ashoori et al. (2011) and Zitha and Du (2010) yield identical solutions when both are fitted to the experimental data by Simjoo and Zitha (2015). In the second part of this work, we adjust the foam model by Chen et al. (2010) to the same experimental data to identify traveling wave solutions under these parameters. We observe that all investigated models exhibit the same classification of traveling wave solutions and piston-like saturation profiles. This observation motivates us to explore the conditions under which these models diverge.

In the last part of this work, we focus on numerically studying the behavior of

these three foam models (by Ashoori et al. (2011); Chen et al. (2010); and Zitha and Du (2010)) in a two-dimensional heterogeneous porous medium, a scenario closer to practical applications. Specifically, we investigate how the models describe bubble distribution in heterogeneous media. Experimental studies face challenges in clearly visualizing foam behavior in heterogeneous media. The contemporary approach to measuring foam flow in porous media in laboratory coreflood experiments relies on a CT-scan technology (Chen et al., 2010; Simjoo et al., 2013a; Shah et al., 2020; Zavala et al., 2022). However, a CT scan cannot directly determine foam density, given that foam and gas exhibit nearly identical densities. Consequently, most assessments of foam strength are carried out indirectly by monitoring pressure drop, which provides only overall information across the core or its regions, assuming homogeneity within these areas. Some authors opted to approximate characterization of the foam present at the end of the core by connecting a camera to the outlet of a core flooding system, as demonstrated by studies such as (Hou et al., 2013; Li et al., 2019; Chen et al., 2010). However, this foam results from dynamics occurring throughout the core, and specific contributions from different regions are not easily distinguished. Despite this limitation, several authors have reported stronger foam generation in higher permeable cores (Moradi-Araghi et al., 1997; Li et al., 2019; Zeng et al., 2020; Shah et al., 2020), as reviewed by Abdelgawad et al. (2022). Coreflood experiments were also employed to fit parameters of the foam model (CMG, 2019), resulting in higher foam strength parameters in more permeable media (Farajzadeh et al., 2015; Kapetas et al., 2017; Gassara et al., 2020). Microfluidic experiments, on the other hand, provide complete visualization of foam generation and propagation throughout the media at the cost of not representing the complexity of a realistic rock. In this context, Lv et al. (2020) reported experiments within a chip featuring higher and lower permeability zones, illustrating that higher permeable regions tend to exhibit more bubbles. Conn et al. (2014) performed similar experiments with a microchip featuring a fracture between low and high-permeability regions and observed that the high-permeability regions were more gas-rich. In the same line, Li et al. (2021) reported that foams are denser in fractures, which have significantly higher permeability compared to the matrix. The numerical study we present in this work indicates that, despite variations in rheology, the foam model that accounts for permeability in bubble generation and coalescence rates better represents foam behavior in heterogeneous media, exhibiting a strong positive correlation between bubble density and permeability. Nevertheless, even in heterogeneous media, all simulated models successfully predict key quantities of interest under steady-state strong foam conditions, such as breakthrough time, production curves, and foam front position. For more details, see (Cedro et al., 2025).

Additionally, in Appendix A, we briefly present a study applying traveling wave analysis to the model by Ashoori et al. (2011) to evaluate the impact of three simplifications on capillary effects in foam displacement. We show that, although the simplifications

result in significantly different foam texture profiles, the extent of the differences is not measurable in laboratory experiments, meaning the results can be considered equivalent. This study is not, however, in the main line of this thesis; for more details, see (Lozano et al., 2022).

## 1.1 WORK STRUCTURE

This work is structured as follows. Chapter 2 introduces the key characteristics of foam flow in porous media and presents the mathematical modeling approach for this phenomenon. In Chapter 3, we investigate traveling wave solutions for a non-Newtonian foam model with shear-thinning behavior presented by Chen et al. (2010). Chapter 4 compares the traveling wave solutions in foam models by Ashoori et al. (2011), Chen et al. (2010), and Zitha and Du (2010), fitted to experimental data from Simjoo and Zitha (2015). Chapter 5 describes the behavior of the above-mentioned models in two-dimensional heterogeneous permeability media, focusing on bubble distribution. Finally, Chapter 6 presents discussions and conclusions.

In addition, Appendix A briefly discusses simplifications on capillary pressure in the model by Ashoori et al. (2011). Appendix B presents the numerical approach employed in one- and two-dimensional simulations. Appendices C to D provide further considerations about Chapter 5.

# 2 THEORETICAL FOUNDATION

## 2.1 FRACTIONAL FLOW THEORY

The fractional flow theory describes the flow dynamics of miscible and immiscible fluids in porous media (Dholkawala et al., 2007; Buckley and Leverett, 1942). This name is due to the analysis of functions that describe the fraction of the total flow corresponding to each phase. The fractional flow theory has several constraints that do not apply to foam flow (Collins, 1976; Lake, 1989). However, some works show how this theory is also useful in explaining the complex mechanisms involved in foam flow in porous media (Rossen and Zhou, 1995; Zhou and Rossen, 1995; Rossen et al., 1999).

This chapter elucidates the fundamental principles of multiphase flow in porous media and introduces the governing equations of this phenomenon. We will also describe the fundamental concepts of foam dynamics and explore their integration into multiphase flow models. Finally, we present the typical modeling approach for foam flow, described in terms of fractional flow functions.

### 2.1.1 Flow in porous media

Porous media refers to materials or substances that contain interconnected voids, pores, or cavities, allowing the flow or passage of fluids or gases through them (Bear, 2018). Examples of porous media include soil, sand, rocks (such as sandstone or limestone), sponges, and filters. Figure 2.1 shows some of these examples. Next, we will define some essential physical quantities in modeling these phenomena.

Porous volume ($V_p$) is the total volume of interconnected voids within a porous

Figure 2.1 – Examples of porous media. (a) Microscopic image of a ceramic. (b) Simplified representation of a porous medium.

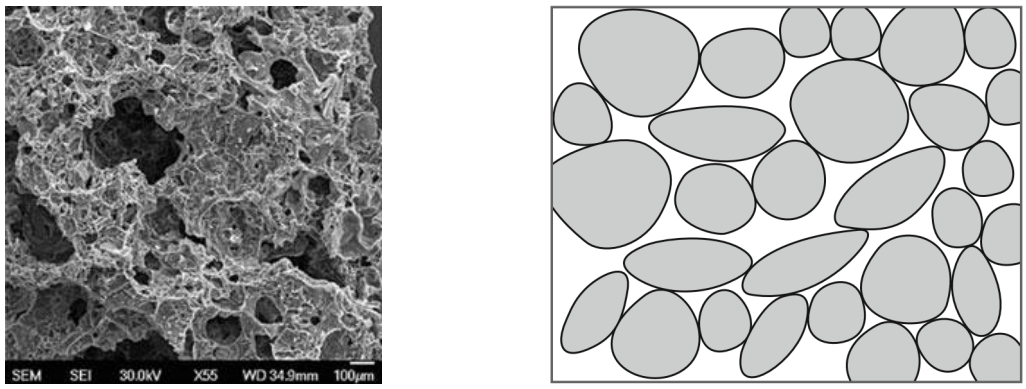


(a) (b)

Source: Bear (2018).

medium that fluid can occupy. Porosity ($\phi$) in a specific region is the ratio of the porous volume to the total volume ($V$) in that region:

$$\phi = \frac{V_p}{V} \,. \tag{2.1}$$

It is worth noting that the continuum hypothesis is commonly employed for mathematical modeling and considering the scale of the problem domain to pore size (Bruining, 2021). Under this assumption, porosity is treated as a point-wise property, assigning a porosity value to each point within the physical domain. This implies that solid material and pores coexist at any point in a proportion represented by $\phi$.

In this study, we aim to investigate the dynamics of multiphase flow involving immiscible phases. Saturation ($S_i$) is defined as the ratio of the volume ($V_i$) occupied by a specific phase $i$ to the porous volume:

$$S_i = \frac{V_i}{V_p} \,. \tag{2.2}$$

Assuming the continuum hypothesis, saturations are considered point-wise values, suggesting that each portion of the domain contains a fraction of each phase. Full saturation of a porous medium occurs when the porous volume is completely filled with the phases included in the model, satisfying the condition:

$$\sum_i (S_i) = 1 \,. \tag{2.3}$$

However, it may not always be possible to displace a phase entirely from a region due to various factors, including the medium's and fluids' properties. In such cases, the residual saturation ($S_{ir}$) describes the minimum amount of phase $i$.

Permeability ($k$), also known as absolute permeability, quantifies the medium's ability to facilitate fluid flow based on the geometric attributes of the pores. Similar to the previous definitions, permeability is treated as a scalar point-wise quantity. In multiphase flow scenarios, the permeability of a phase is generally lower compared to single-phase flow (Chen et al., 2006). Thus, we define effective permeability ($k_i$) as the flow capacity of phase $i$ in the presence of the other phases. Moreover, relative permeability ($k_{ri}$) is the ratio of the effective permeability to the absolute permeability, so that:

$$k_i = k_{ri}\, k \,. \tag{2.4}$$

Several models of relative permeabilities describe them as functions of the phase saturations (Brooks and Corey, 1966; Mualem, 1976; van Genuchten, 1980; Chierici, 1984; Lomeland et al., 2005).

Viscosity ($\mu_i$) characterizes the resistance a fluid presents to flow. Considering the medium and all fluid properties involved in the flow, we describe the ability of phase $i$ to

move through the medium as mobility ($\lambda_i$). Mobility is the ratio of effective permeability $k_i$ to viscosity $\mu_i$. Additionally, we define total mobility ($\lambda$) and relative mobility ($\lambda_{ri}$) as follows:

$$\lambda_i = \frac{k_i}{\mu_i}\,, \quad \lambda_{ri} = \frac{k_{ri}}{\mu_i} \quad \text{and} \quad \lambda = \sum_i \lambda_i\,. \tag{2.5}$$

Finally, we define fractional flow ($f_i$) as the volumetric fraction of the displacement in a specific direction composed of phase $i$. This flow is equivalent to ratio of phase mobility $\lambda_i$ to total mobility (Buckley and Leverett, 1942; Lake, 1989):

$$f_i = \frac{\lambda_i}{\lambda} \;\Rightarrow\; \sum_i f_i = 1\,. \tag{2.6}$$

### 2.1.2 Darcy's law

Darcy's law is a constitutive equation experimentally inferred by Henry Darcy (Darcy, 1856), which describes the hydrodynamic behavior of single-phase flow in porous media. This equation establishes a proportional relationship between the flow velocity $\mathbf{u}$ and the pressure gradient in the reservoir ($\nabla p$). In the absence of gravitational effects, the relationship is given by:

$$\mathbf{u}(\mathbf{x}) = -\frac{\mathbf{k}(\mathbf{x})}{\mu}\nabla p\,, \tag{2.7}$$

where, for an $n$-dimensional medium, $\mathbf{u}(\mathbf{x}) \in \mathbb{R}^n$ is the velocity at a point $\mathbf{x} \in \mathbb{R}^n$, and $\mathbf{k}(\mathbf{x}) \in \mathbb{R}^n \times \mathbb{R}^n$ is the permeability tensor at $\mathbf{x}$. Each component $k_{i,j}$ in the tensor $\mathbf{k}$ represents the ease of fluid displaces in the $i$ direction due to a pressure gradient in the $j$ direction. In certain cases, it is possible to assume a diagonal tensor, *i.e.*, $k_{i,j} = 0$ for $i \neq j$ (Chen et al., 2006). In isotropic media, permeability is independent of direction, resulting in $k_{ii} = k$. In homogeneous media, permeability is constant, meaning it does not vary with $\mathbf{x}$

The superficial velocity $\mathbf{u}$, or Darcy velocity, is the effective fluid flow velocity through a porous medium on a macroscopic scale. It represents the overall rate of mass displacement across a section. On the other hand, interstitial velocity $\mathbf{v}$, or actual velocity, refers explicitly to the fluid movement occurring within the pores of the porous medium:

$$\mathbf{u} = \phi\mathbf{v}\,. \tag{2.8}$$

Muskat and Meres proposed adapting Darcy's law to describe the dynamics of multiphase flows in porous media (Muskat and Meres, 1936). For each phase $i$, partial Darcy velocity $\mathbf{u}_i$ and partial pressure $p_i$ are defined. Thus, we have:

$$\mathbf{u}_i(\mathbf{x}) = -\mathbf{k}(\mathbf{x})\lambda_{ri}\nabla p_i\,, \quad \mathbf{u} = \sum_i \mathbf{u}_i\,. \tag{2.9}$$

The partial Darcy velocity $\mathbf{u}_i$ considers only the portion of the interstitial phase velocity ($\mathbf{v}_i$) corresponding to the volumetric fraction occupied by phase $i$ in the medium:

$$\mathbf{u}_i = \phi S_i \mathbf{v}_i \,. \tag{2.10}$$

The relation between each phase pressure $p_i$ and global pressure $P$ is presented by (Chavent and Jaffré, 1986; Chen et al., 2006) and briefly discussed in Appendix B.2.

### 2.1.3 Conservation laws

A conservation law is a partial differential equation (PDE) that describes the behavior of a specific quantity that remains constant over time (LeVeque, 2002). We can express the conservation law for a quantity $\nu$ as the following differential equation:

$$\frac{\partial \nu}{\partial t} + \nabla \cdot \mathbf{f}(\nu) = 0 \,, \tag{2.11}$$

where, $\mathbf{f}$ is the volumetric flux of $\nu$ per unit area. Equation (2.11) asserts that, in any bounded region, the temporal variation of the quantity $\nu$ depends solely on the flux of this quantity entering or leaving that region.

The principle of mass conservation plays a crucial role in fluid dynamics. Regarding flow in porous media, we can express this conservation law in terms of phase saturations. Since we are dealing with immiscible fluids, there is no mass transfer between the phases. Consequently, we can establish a separate conservation law for the mass of each phase. Considering the mass $m_i$ of phase $i$ with density $\rho_i$ within the pores of a region with volume $V$, we obtain:

$$m_i = \rho_i (V \phi S_i) \,.$$

Hence, we can derive the conservation law for mass in porous media for phase $i$ from (2.11) by setting $\nu = m_i$ and defining the mass flux per unit area as $\mathbf{f}(m_i) = m_i \mathbf{v}_i$. Thus, we have:

$$\frac{\partial}{\partial t} (\rho_i \phi S_i) + \nabla \cdot (\rho_i \mathbf{u}_i) = 0 \,. \tag{2.12}$$

In the case of incompressible phases, the density $\rho_i$ remains constant and is independent of position or time, simplifying the equation. Moreover, the porosity $\phi$ is also constant for homogeneous media.

### 2.1.4 Two-phase flow

In this work, we use water-gas flow as the foundation for developing foam flow models. This model considers $i = w$ for the aqueous phase and $i = g$ for the gaseous phase. According to (2.6) and (2.9):

$$f_g + f_w = 1 \quad \text{and} \quad \mathbf{u}_g + \mathbf{u}_w = \mathbf{u} \,. \tag{2.13}$$

Figure 2.2 – Capillary effects in tubes of different thicknesses, where the gray fluid is wetting on the red surface and non-wetting on the blue surface.

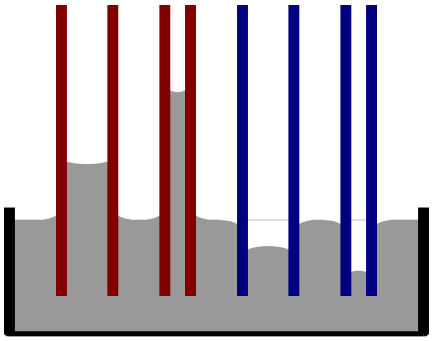

Source:
https://commons.wikimedia.org/wiki/File:CapillaryAction.svg

When dealing with multiphase problems, the interaction between the phases' interfaces significantly influences the hydrodynamics. Different substances interact differently with surfaces, exhibiting varying levels of molecular attraction to the surface. The wetting phase, which experiences more significant attraction, tends to form a larger contact area with the surface, causing it to move toward the non-wetting phase. This phenomenon, known as capillarity, becomes more pronounced when the wetting fluid's contact area with the solid surface is larger compared to the total fluid quantity. Figure 2.2 illustrates the intensified capillary action in narrower tubes, where the fluid portion is reduced in relation to the contact surface area. This emphasizes the importance of capillary effects in porous media flow, as they possess extensive surface contact with the fluid. Therefore, we define capillary pressure ($P_c$) as the difference between the pressures of the non-wetting and wetting phases at these interfaces. A phase's wetting or non-wetting nature depends on the phases involved in the interaction and the medium with which they interact (Cassie and Baxter, 1944; Hirasaki, 1991). In our problem, the aqueous phase is wetting, while the gas phase is non-wetting. Hence:

$$P_c = p_g - p_w \,. \tag{2.14}$$

Capillary pressure $P_c$ is commonly described as a function of saturation through the Leverett J-function (Leverett, 1941), which incorporates porosity and permeability, thereby connecting macroscopic properties of the porous medium to capillary behavior:

$$J(S_w) = \frac{P_c}{\sigma}\sqrt{\frac{k}{\phi}}\,, \tag{2.15}$$

where $\sigma_{wg}$ is the interfacial tension. This function provides a normalized framework to analyze capillary pressure across different porous media. Later, in Section 2.4, we present the J-function for the models we study in this work.

Using the capillary pressure definition (2.14) we can derive the relationship between the partial velocities $\mathbf{u}_w$ and $\mathbf{u}_g$ and the total velocity $\mathbf{u}$ from Eqs. (2.9) and (2.4)-(2.6) (Chen et al., 2006):

$$\begin{aligned} \mathbf{u}_w &= \mathbf{u} f_w + \mathbf{k}\lambda_{rg} f_w \nabla P_c \,, \\ \mathbf{u}_g &= \mathbf{u} f_g - \mathbf{k}\lambda_{rw} f_g \nabla P_c \,. \end{aligned} \tag{2.16}$$

By combining the mass conservation law (2.12) with the velocity expression (2.16), derived from Darcy's law, we obtain the following expression for the aqueous phase (Barenblatt et al., 1989):

$$\frac{\partial}{\partial t}\left(\rho_w \phi S_w\right) + \nabla \cdot \left(\rho_w \mathbf{u} f_w\right) + \nabla \cdot \left(\rho_w \mathbf{k}\lambda_{rg} f_w \nabla P_c\right) = 0 \,. \tag{2.17}$$

There is no need to derive an equivalent expression for the gas phase in two-phase flow through a saturated porous medium since $S_g + S_w = 1$.

## 2.2 FOAM FLOW IN POROUS MEDIA

This section highlights the main characteristics of foam flow in porous media. Its modeling extends the fractional flow theory by incorporating the effects of foam on flow behavior. This work defines foam as an aggregation of gas bubbles separated by a liquid film called lamella (Bikerman, 1973; Hirasaki, 1989; Hematpur et al., 2018). However, achieving this bubble structure is difficult when the lamellae consist solely of water because water's surface tension makes them kinetically unstable. To obtain stable bubbles in an aqueous medium, surfactants are added to the solution, reducing surface tension (Wang and Li, 2016).

### 2.2.1 Surfactants

*Surfactants* are molecules that reduce the surface tension of aqueous solutions (Evans and Wennerström, 1999). These molecules have a structure with one hydrophilic and one hydrophobic end. This structural arrangement causes surfactants to accumulate at the interface between the aqueous solution and other phases, reducing the surface tension of water and facilitating the formation of stable lamellae (Ma et al., 2014b; Wang and Li, 2016). Figure 2.3 illustrates the composition of a lamella in a porous rock medium during three-phase flow, showing surfactant molecules at the liquid film's surface, which stabilize the lamella structure.

Increasing the surfactant concentration in the medium decreases the solution's surface tension as the surfactant molecules deposit at the aqueous surface. However, when the surface becomes saturated with the surfactant, the molecules aggregate within the liquid, forming spherical conformations called micelles. We refer to the concentration at which

Figure 2.3 – Representation of bubbles in a porous rock medium with a three-phase flow of water, gas, and oil. Surfactant molecules are at the interface between water and gas, based on the properties of their hydrophilic and hydrophobic parts (Farajzadeh et al., 2012; Fejoli and Romero, 2014).

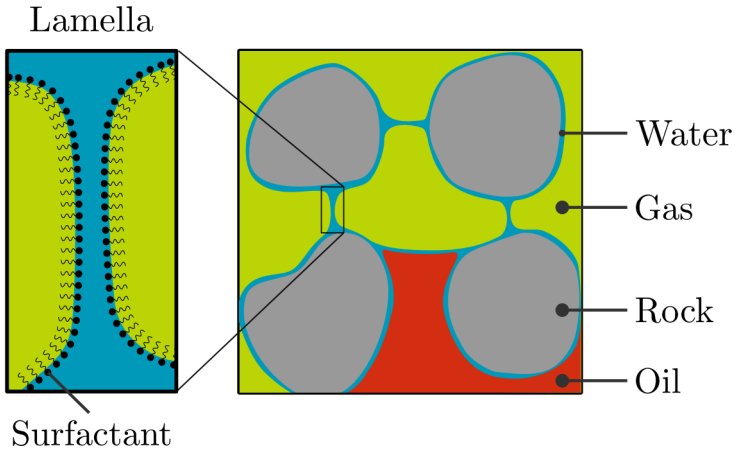


Source: Adapted from Farajzadeh et al. (2012).

this occurs as the *critical micelle concentration* (CMC). Concentrations above the CMC do not significantly affect the surface tension (Kile and Chiou, 1989; Evans and Wennerström, 1999). Figure 2.4 illustrates the relationship between surfactant concentration and surface tension.

Figure 2.4 – Water surface tension as a function of surfactant concentration.

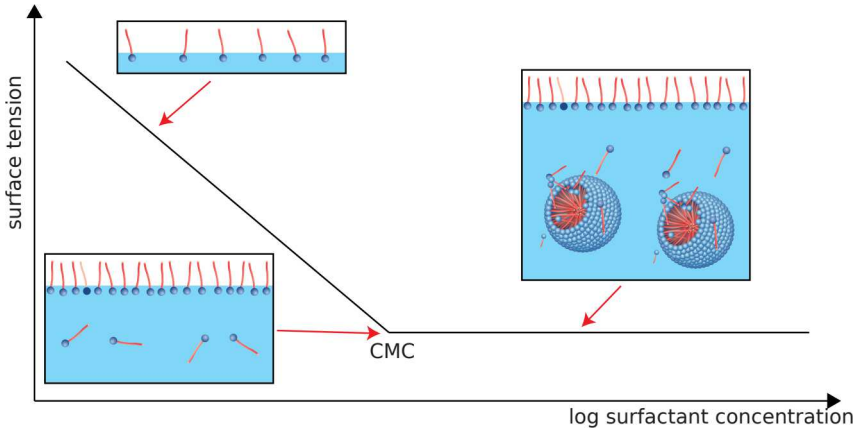


Source: DataPhysics Instruments (2020).

### 2.2.2 Creation and destruction mechanisms

Foam flow in porous media applications involves the introduction of surfactant solutions with gases to generate bubbles. This process can occur before injection (pre-generated foam) or after surfactant injection (*in-situ* generation) (Zhang et al., 2009;

Figure 2.5 – Bubble generation mechanisms in porous media: (a) leave-behind, (b) snap-off, and (c) division (Hematpur et al., 2018).

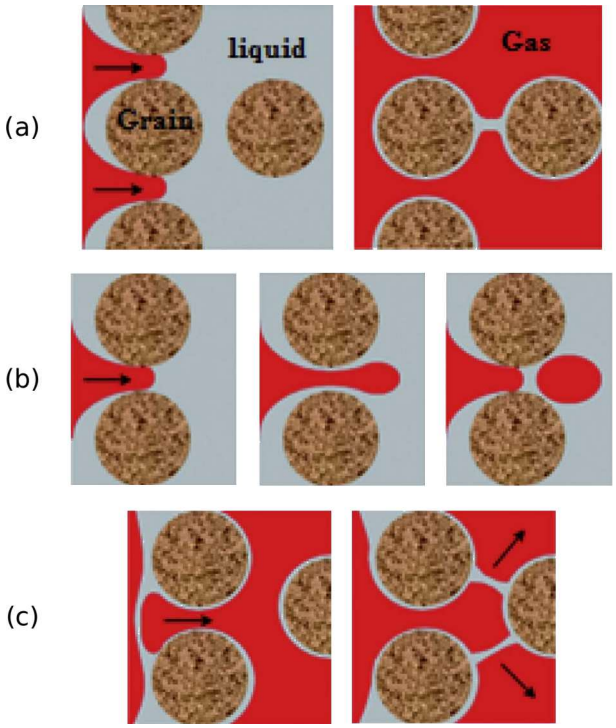


Source: Hematpur et al. (2018).

Afsharpoor et al., 2010; Hematpur et al., 2018). In porous media, we traditionally describe bubble formation through three main mechanisms. The first mechanism, *leave-behind*, occurs when the gas displaces the initially water-filled region, leaving a residual liquid solution between the pores that form lamellae. The second mechanism, *snap-off*, happens when an individual gas bubble detaches from a continuous gas phase. The third mechanism is the *lamella division*, in which lamellae divide into smaller ones. Figure 2.5 illustrates these three generation mechanisms. Researchers have recently observed two other lamellae creation phenomena: *neighbor-wall pinch-off* and *neighbor-neighbor pinch-off* (Liontas et al., 2013). These occur when a bubble splits in two due to pressure from pore walls or other bubbles.

When the liquid film's thickness becomes too thin to support the lamella structure, the bubble collapses in a phenomenon called coalescence (Bikerman, 1973; Kovscek and Radke, 1994; Rossen, 1996). The foam structure becomes unstable under high capillary pressure, resulting in a sudden rupture of the lamellae. Various multiphase models assume capillary pressure can be described based on phase saturations. Khatib et al. (1988) demonstrated the existence of a limiting capillary pressure threshold ($P_c^*$) beyond which bubbles collapse. Consequently, a limiting water saturation value ($S_w^*$) is associated with foam instability since capillary pressure can be described as a function of water saturation. Figure 2.6 shows this behavior. It also follows that permeability should influence the rate

Figure 2.6 – Relationship between capillary pressure and water saturation. Bubbles become unstable below the limiting water saturation $S_w^*$ (or above a limiting pressure $P_c^*$).

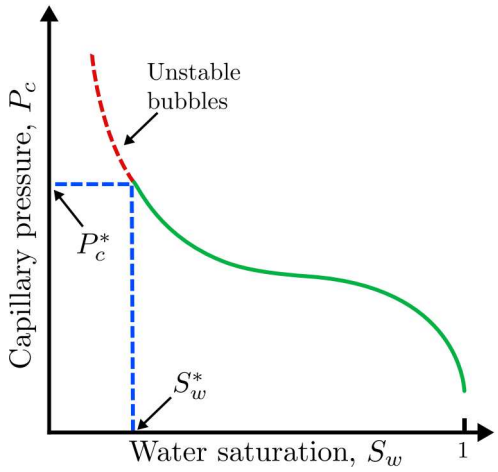


Source: Adapted from Khatib et al. (1988).

of foam destruction, as lower permeability levels tend to elevate capillary pressure, thereby facilitating foam destruction as it approaches the limiting capillary pressure. In Chapter 5, we study the impact of permeability on foam generation rates driven by capillarity for the foam models introduced in Section 2.4.

### 2.2.3 Foam texture

Some foam structures are more efficient than others in reducing gas mobility. In general, foams with a higher number of bubbles and more lamellae are more effective in reducing gas mobility (Afsharpoor et al., 2010). Hence, we classify foams with numerous lamellae as *strong* and ones with few as *weak* (Figure 2.7). We define the concept of *foam texture* ($n_f$) to quantify the number of lamellae or bubbles per unit area or volume. Hence, a higher foam texture (or finer texture) leads to a greater gas mobility reduction and a stronger foam.

## 2.3 MODELING

There are two main types of models for foam flow dynamics: empirical and mechanistic. Commercial software primarily employs empirical models (CMG, 2019; Cheng et al., 2000; Schlumberger, 2010). These models mathematically define the foam quantity using algebraic relationships derived from empirical correlations without considering it as an unknown variable in the equations. In contrast, mechanistic models treat the foam quantity as an independent variable and include it explicitly in the problem equations. From a physical perspective, mechanistic models are considered more accurate (Hematpur

Figure 2.7 – Representation of strong and weak foams in a porous medium.

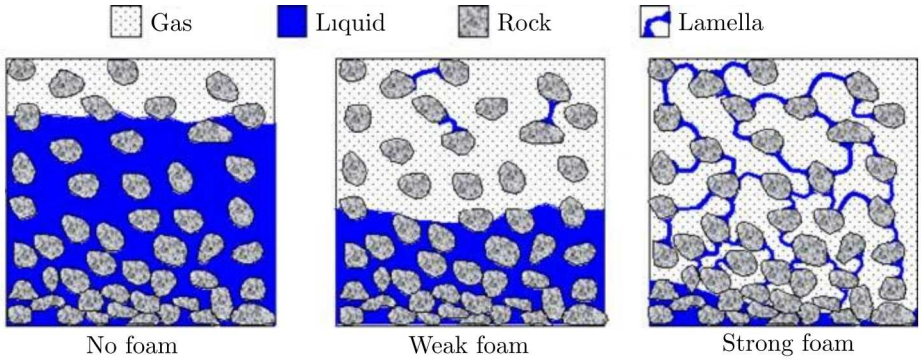


Source: Dholkawala et al. (2007).

et al., 2018). However, some mechanistic models, when in local equilibrium (steady-state foam), yield results similar to those of empirical models. In this work, we focus on mechanistic models.

As mentioned, we can quantify foam's strength by the foam texture ($n_f$). However, due to the high magnitude of bubble density in many applications, it is common to represent foam texture normalized to a reference foam texture constant ($n_{\max}$). We define the dimensionless foam texture value ($n_D$) as follows:

$$n_D = \frac{n_f}{n_{\max}} \,. \tag{2.18}$$

We can model foam transport using a balance law for the foam amount. Balance laws differ from conservation laws in that they describe situations where a quantity may not be conserved, resulting in the inclusion of a source term in the equation. In this case, the source term is proportional to the bubble creation and destruction rate. Since $n_D$ represents the density of lamellae in the gaseous phase, we consider a balance law for the product ($S_g n_D$) with a source function $\Phi$ describing the creation and destruction of bubbles per unit gas volume ($\phi S_g$). Gathering Eqs. (2.9) and (2.12) with a bubble balance equation and assuming incompressible flow (constant phase densities), the governing equations for water-gas foam flow in porous media are expressed as:

$$\mathbf{u}_i = -\lambda_i \nabla p_i \,, \tag{2.19}$$

$$\frac{\partial}{\partial t}(\phi S_i) + \nabla \cdot \mathbf{u}_i = 0 \,, \tag{2.20}$$

$$\frac{\partial}{\partial t}(\phi S_g n_D) + \nabla \cdot (\mathbf{u}_g n_D) = \phi S_g \Phi \,, \tag{2.21}$$

where Eq. (2.19) is Darcy's law adapted for multi-phase flow (with $i = w$ for the water solution and $i = g$ for the gaseous phase), Eq. (2.20) is the mass conservation of each phase, and Eq. (2.21) is the population balance of foam texture. The partial Darcy velocities are given in Eq. (2.16).

The specifics of the foam generation rate $\Phi$ vary depending on the model employed to describe bubble generation and destruction mechanisms, as elaborated in subsequent sections. Empirical models only consider foam texture in equilibrium, *i.e.*, with $\Phi = 0$. The models we deal with in this work assume a sufficiently high surfactant concentration to ensure no interference in the foam dynamics.

The main purpose of using foams in porous media is the reduction of gas mobility. This behavior is commonly incorporated into multiphase flow models by modifying either the relative permeability of gas ($k_{rg}$) or the gas viscosity ($\mu_g$) in the presence of foam. In this work, we denote $\mu_f$ as the apparent gas viscosity in the presence of foam. Therefore, in a foam flow, gas mobility ($\lambda_g$) becomes dependent on the foam texture ($n_D$).

Another essential aspect in the physics of foam flow is the concentration of surfactant in the aqueous phase, as it is one of the main factors determining foam creation. Some mechanistic models consider surfactant concentration as a variable of the problem (Trogus et al., 1977; Chen et al., 2010; Thorat and Bruining, 2016). Other models assume that surfactant concentration is constant and sufficiently high not to affect the bubble creation and destruction rate (Kovscek et al., 1995; Kam, 2008; Zitha and Du, 2010; Ashoori et al., 2011), based on the concept of critical micelle concentration. Some models also consider the transport of surfactant particles, including phenomena such as surfactant adsorption on the walls of the porous medium, which influences foam generation and destruction (Thorat and Bruining, 2016; Trogus et al., 1977). In this work, we neglect variations in surfactant concentration in the flow.

Researchers often report the flow behavior of foam flow as shear-thinning (non-Newtonian) in various studies (Bretherton, 1961; Hirasaki and Lawson, 1985; Khatib et al., 1988; Falls et al., 1989; Alvarez et al., 2001). This means that foam's apparent viscosity should decrease as gas velocity increases. Several foam models in the literature account for this behavior, *e.g.*, Kovscek et al. (1995); Kam (2008); Chen et al. (2010); Thorat and Bruining (2016). However, due to mathematical complexity, the non-Newtonian behavior of foam flow is often neglected in analytical investigations. In Chapter 3, we address this gap by employing an explicit formulation of foam apparent viscosity proposed by Hirasaki and Lawson (1985).

## 2.4 FOAM MODELS

In this section, we present the foam models used in this work: Model A, introduced by Ashoori et al. (2011); Model B, presented by Chen et al. (2010); and Model C, developed by Zitha and Du (2010). In the following chapters, we study these models using the same relative permeability and capillary functions described by Chen et al. (2010). The relative

permeability is built upon Brooks and Corey (1964):

$$k_{rw} = \begin{cases} 0 & , \quad 0 \leq S_w < S_{wc} \\ k^0_{rw} \left( \dfrac{S_w - S_{wc}}{1 - S_{wc}} \right)^{n_w} & , \quad S_{wc} \leq S_w \leq 1 \end{cases} , \tag{2.22}$$

$$k_{rg} = \begin{cases} k^0_{rg} \left( \dfrac{X_f S_g}{1 - S_{wc}} \right)^{n_g} & , \quad 0 \leq S_g \leq 1 - S_{wc} \\ 0 & , \quad 1 - S_{wc} < S_g \leq 1 \end{cases} , \quad S_g = 1 - S_w \, . \tag{2.23}$$

Parameters $k^0_{rw}$ and $k^0_{rg}$ are the end-point relative permeabilities, while $n_w$, $n_g$ represent model constants, and $S_{wc}$ is the connate or residual water saturation. Model B incorporates the fraction $X_f$, indicating the proportion of the gaseous phase that actively flows through the pores, *i.e.*, there is a fraction of gas $X_t = 1 - X_f$ which remains immobile. This fraction was introduced in the model by Kovscek et al. (1995) as depending on foam texture and later assumed as constant by Chen et al. (2010). Models A and C do not account for trapped foam; therefore, for these models, we assume $X_f = 1$.

The capillary pressure between water and gas is based on the J-Leverett function Eq. (2.15) (Leverett, 1941; Kovscek et al., 1995):

$$P_c(S_w) = \sigma_{wg} \sqrt{\frac{\phi}{k}} \left( \frac{0.022}{S_w - 0.15} \right)^{0.2} , \tag{2.24}$$

where $\sigma_{wg}$ is the interfacial tension between water and gas. The above capillary pressure function was fitted specifically for Boise sandstone, as reported by Kovscek et al. (1995).

Foam flow dynamics are incorporated into the model by defining the foam apparent viscosity $\mu_f$ and the source term $\Phi$ in the population balance of foam texture. In the following sections, we outline the definitions of these terms as presented in the foam models by Ashoori et al. (2011), by Chen et al. (2010), and by Zitha and Du (2010), which we denoted by models A, B, and C, respectively.

### 2.4.1 Model A

Ashoori et al. (2011) introduced the first-order kinetic model, referred to here as Model A, which establishes a linear correlation between gas mobility reduction in the presence of foam and foam texture. The apparent viscosity of foamed gas is defined as:

$$\mu_f = \mu_g \left( 1 + C_{\mathrm{MRF}} n_D \right) , \tag{2.25}$$

where $C_{\mathrm{MRF}}$ is a reference mobility reduction factor for strong foam. Since this model does not consider the hypothesis of trapping gas, we take $X_f = 1$ for the gas' relative permeability function (2.23).

The generation and coalescence of foam are represented by the source term $\Phi$ in (2.21), which for Model A is given by:

$$\Phi = K_c \left( n_D^{\mathrm{LE}} \left( S_w \right) - n_D \right) , \tag{2.26}$$

where $n_D^{\mathrm{LE}}$ denotes the local equilibrium foam texture, *i.e.*, the value at which foam generation and coalescence rates are equal, leading to a dynamic equilibrium state. The constant $K_c$ controls how fast foam reaches equilibrium (the foam creation and destruction rates).

Model A incorporates the concept of limiting capillary pressure (discussed in Section **2.2.2**) into the expression for the local equilibrium foam texture:

$$n_D^{\mathrm{LE}}(S_w) = \begin{cases} \tanh\left( A \left( S_w - S_w^* \right) \right) , & S_w > S_w^* \\ 0 , & S_w \leq S_w^* \end{cases} , \tag{2.27}$$

where $S_w^*$ is the limiting water saturation below which foams become unstable, and $A$ is a model parameter that controls the sharpness of the transition region from weak to strong foam near $S_w^*$. For higher values of $A$, such as adopted by Ashoori et al. (2011), the transition zone of $n_D^{\mathrm{LE}}$ becomes sharper, resembling a step function. Consequently, except for a small region near $S_w = S_w^*$, $n_D^{\mathrm{LE}}$ is approximately either zero or one.

### 2.4.2 Model B

The foam model introduced by Chen et al. (2010), based on the earlier work by Kovscek et al. (1995), is designated as Model B in this study. This model incorporates a non-Newtonian behavior for foam flow by using the foam's apparent viscosity as described by Hirasaki and Lawson (1985):

$$\mu_f = \mu_g + \alpha \frac{n_D \, n_{\max}}{\| \mathbf{v}_g \|^{1/3}} \quad \text{with} \quad \mathbf{v}_g = \frac{\mathbf{u}_g}{\phi S_g X_f} , \tag{2.28}$$

Here, $\alpha$ represents a proportionality constant. This relation indicates a shear-thinning behavior for foam flow, as the foam apparent viscosity ($\mu_f$) decreases with the foamed gas velocity ($\| \mathbf{v}_g \|$).

The foam source term $\Phi$ is expressed as:

$$\begin{cases} \Phi = r_g - r_c \, , \\ r_g = \dfrac{k_1^0}{n_{\max}} \left( 1 - n_D^3 \right) \| \mathbf{v}_w \| \, \| \mathbf{v}_g \|^{\frac{1}{3}} \, , \\ r_c = k_{-1}^0 \left( \dfrac{P_c}{P_c^* - P_c} \right)^2 \| \mathbf{v}_g \| \, n_D \, , \end{cases} \tag{2.29}$$

where $k_1^0$ and $k_{-1}^0$ are model constants, and $P_c^*$ is the limiting capillary pressure above which bubbles abruptly collapse.

In Eq. (2.29), the generation rate $r_g$ models bubble formation through snap-off, with the bubble generation frequency in a pore being directly proportional to the liquid velocity and to the gas velocity raised to the power of a third (Kovscek and Radke, 1994; Kovscek et al., 1995). The factor $(1 - n_D^3)$ accounts for the limiting role of pre-existing bubbles on foam-generation sites. The motivation is that more than one foam bubble per pore is not typically expected (Bertin et al., 1998), and this one-bubble-per-pore limit is represented by the reference foam texture $n_{\max}$ that we used to normalize the foam texture. Note that in both Eqs. (2.28) and (2.29), the explicit appearance of $n_{\max}$ is due to the normalization of foam texture $n_D = n_f/n_{\max}$.

The coalescence rate $r_c$ in Eq. (2.29) presents a pore-level factor for foam lamellae destruction, where the destruction rate is proportional to their flux, $\|\mathbf{v}_g\| n_D$ (Kovscek et al., 1995). The coalescence rate also asymptotically increases with capillary pressure $P_c$ up the its limiting value $P_c^*$, as predicted by Khatib et al. (1988). Notice that, in contrast, Model A (Section **2.4.1**) incorporates this concept indirectly through limiting water saturation $S_w^*$. That difference makes the presence of foam in Model B more sensitive to changes in absolute permeability. Both Kovscek et al. (1995) and Chen et al. (2010) consider $P_c^*$ to be dependent on surfactant concentration $C_s$. Following these authors, we assume that the surfactant concentration is significantly above the critical micelle concentration, meaning that $C_s$ do not influence foam generation and stability (Kile and Chiou, 1989). This hypothesis allows us to analyze the results, excluding the influence of surfactant concentration leading to constant $P_c^*$. Additionally, Khatib et al. (1988) demonstrated that limiting capillary pressure can vary with permeability. However, we follow Chen et al. (2010) and assume that $P_c^*$ is independent of permeability variation.

### 2.4.3 Model C

Model C, introduced by Zitha and Du (2010), describes foam flow as a yield stress fluid following a Herschel-Bulkley rheological model. However, as discussed by the authors, during transient foam flow, this behavior can be approximated using the Hirasaki and Lawson relation (2.28).

Unlike Model B, Model C does not include an explicit term for the trapped foam fraction. Consequently, for this model, we assume $X_f = 1$ in the superficial velocity expression (2.28) and in the gas relative permeability formulation in (2.23), following an approach similar to Model A discussed in Section **2.4.1**.

Following Zavala et al. (2022), foam texture source term proposed by Zitha and

Du (2010) can be written as:

$$\Phi = (K_g + K_d)(n_D^{\mathrm{LE}} - n_D)\,, \quad \text{where} \quad n_D^{\mathrm{LE}} = \frac{K_g}{K_g + K_d}\,. \tag{2.30}$$

Following previous works (Zitha et al., 2006; Simjoo et al., 2013b; Simjoo and Zitha, 2015), we assume foam destruction is negligible by setting $K_d = 0$. Under this assumption, the local equilibrium foam texture simplifies to $n_D^{\mathrm{LE}} = 1$, reducing the complexity of bubble generation dynamics and making the source term of Model C a particular case of Model A's source term (2.26)-(2.27). In this case, foam texture described by Model C always tends to local equilibrium $n_D^{\mathrm{LE}} = 1$. In essence, Model C features a simpler source term than Model A while retaining foam rheology as complex as Model B.

# 3 TRAVELING WAVE SOLUTION FOR NON-NEWTONIAN FOAM

In this chapter, we find a traveling wave solution for the non-Newtonian proposed by Chen et al. (2010), which incorporates the foamed gas apparent viscosity defined by Hirasaki and Lawson (1985). We refer to this model as Model B, as described in Section **2.4.2**. We validate our semi-analytical solution with numerical simulations and experimental data. The methodology and results presented in this chapter were published in (Cedro and Chapiro, 2022, 2024).

## 3.1 FOAM FLOW MODEL

In this chapter, we deal with a one-dimensional form of governing equations (2.19)-(2.21), assuming incompressible flow and constant total Darcy velocity in a rigid and homogeneous porous matrix, where $\rho_w$, $\rho_g$, $u$, $\phi$, and $k$ are constants. Thus, we can write the governing equations as:

$$\begin{cases} \phi \dfrac{\partial S_w}{\partial t} + \dfrac{\partial u_w}{\partial x} = 0 \,, \\ \phi \dfrac{\partial}{\partial t}(S_g n_D) + \dfrac{\partial}{\partial x}(u_g n_D) = \phi S_g \Phi \,. \end{cases} \tag{3.1}$$

We seek to study solutions in the form of a traveling wave for Model B (see Section **2.4.2**). In Chen et al. (2010), the authors assumed a constant trapped gas fraction, $X_t$. In this chapter, we consider $X_t$ as increasing with foam texture, as proposed by Kovscek et al. (1995):

$$X_t = X_{t,\max}\left(\frac{\beta n_t}{1+\beta n_t}\right), \qquad X_t + X_f = 1\,, \quad n_t \approx n_f\,, \tag{3.2}$$

where $X_{t,\max}$ is the maximum trapped gas fraction, $n_t$ is the trapped texture, and $\beta$ is a trapping parameter.

### 3.1.1 Explicit foam's apparent viscosity formula

A semi-analytical traveling wave solution for Model B described in Section **2.4.2** requires dealing with the foam's apparent viscosity $\mu_f$ from Eq. (2.28). In this equation, $\mu_f$ depends on gas velocity $v_g$, which itself depends on $\mu_f$, making the foam's apparent viscosity formula (2.28) challenging to handle for both numerical and analytical studies. Kam (2008) introduced an iterative loop to compute $\mu_f$ and $v_g$ at each step of their numerical simulations. This approach was later adopted in developing our in-house numerical simulator (de Paula et al., 2020) (see Appendix B.2). Pereira and Chapiro (2023) showed that it is possible to use the relations (2.5)-(2.6) and (2.16) to rewrite (2.28)

as a cubic expression of $\mu_f$, and explicitly obtain a single physical root $\mu_f$ as function of $S_w$, $n_D$ and $\mathrm{d}P_c/\mathrm{d}x$:

$$\begin{cases} \mu_f = \mu_g + \dfrac{3a}{\lambda_w}\Big(c_{(+)} + c_{(-)}\Big)\,, \quad c_{(\pm)} = \sqrt[3]{b \pm \sqrt[2]{b^2 - a^3}}\,, \\ a = \dfrac{\alpha n_f \lambda_w}{3}\left(\dfrac{\phi X_f S_g}{k_{rg}\left|u - k\lambda_w \frac{\mathrm{d}P_c}{\mathrm{d}S_w}\frac{\partial S_w}{\partial x}\right|}\right)^{1/3}, \qquad b = \dfrac{k_{rg} + \lambda_w \mu_g}{2}\,. \end{cases} \tag{3.3}$$

Notice that $\mu_f$ is not well defined for $S_w = 1$ in (3.3), since $k_{rg} = 0$.

Pereira and Chapiro (2023) used Eq. (3.3) to find traveling wave solutions for a variation of Model A in local equilibrium, modified by the inclusion of the non-Newtonian foam's apparent viscosity (2.28). Eq. (3.3) also enabled de Paula et al. (2023) to enhance their numerical solver. In this work, we apply the formula (3.3) to find a traveling wave solution in a more complex non-Newtonian foam model, Model B.

## 3.2 TRAVELING WAVE FORMULATION

As we introduced in this chapter, searching solutions in the form of traveling waves means actively searching for a static profile $U = (S_w, n_D)$ that displaces through the time $t$ over $x$-axis with a constant velocity $\nu$. For that, we define the change of variables:

$$\eta = x - \nu t\,, \qquad U(x,t) \equiv \tilde{U}(\eta, t)\,, \tag{3.4}$$

where $\nu$ is the constant wave velocity and $\tilde{U}$ represents the solution in the transformed coordinates $(\eta, t)$. Substituting (3.4) into the system of PDEs (3.1) and assuming $\partial\tilde{U}/\partial t = 0$ (indicating that solution is stationary in the new coordinates) reduces the problem to a system of ODEs in the variable $\tilde{U}(\eta)$ (see Volpert et al. (2000); Ghazaryan et al. (2022) for further details):

$$\begin{cases} -\nu\phi\dfrac{\mathrm{d}S_w}{\mathrm{d}\eta} + \dfrac{\mathrm{d}u_w}{\mathrm{d}\eta} = 0\,, \\ -\nu\phi\dfrac{\mathrm{d}}{\mathrm{d}\eta}(S_g n_D) + \dfrac{\mathrm{d}}{\mathrm{d}\eta}(u_g n_D) = \phi S_g \Phi\,. \end{cases} \tag{3.5}$$

For simplicity, from Eq. (3.5) onward, we omit the notation "$\sim$". To find traveling waves, we assume the following asymptotic boundary conditions for the system:

$$\lim_{\eta\to\pm\infty} U = U^{\pm} \qquad \Rightarrow \qquad \lim_{\eta\to\pm\infty} \frac{\mathrm{d}U}{\mathrm{d}\eta} = 0\,. \tag{3.6}$$

From the point of view of the ODE theory, it means that the traveling wave solution connects constant equilibria states $U^-$ to $U^+$ in the phase space $S_w \times n_D$. From now on, we use indices $+$ and $-$ to denote that the function is evaluated at the states $U^+$ and $U^-$. To find these equilibrium states, we aim to write the ODEs (3.5) in the explicit form.

From the first equation of (3.5), we obtain the invariant:

$$\frac{\mathrm{d}}{\mathrm{d}\eta}\Big(-\nu\phi S_w + u_w\Big) = 0 \quad \Rightarrow \quad -\nu\phi S_w + u_w = -\nu\phi S_w^+ + u_w^+ = -\nu\phi S_w^- + u_w^- \,. \tag{3.7}$$

Notice that, applying the limits (3.6) to phase velocities equations (2.16) results $u_w^\pm = u f_w^\pm$. Thus, the traveling wave velocity $\nu$ can be written as:

$$\nu = \frac{u}{\phi}\,\frac{f_w^+ - f_w^-}{S_w^+ - S_w^-} \,. \tag{3.8}$$

Substituting partial velocities (2.16) into (3.7) yields

$$\frac{\mathrm{d}S_w}{\mathrm{d}\eta} = \frac{\nu\phi(S_w - S_w^\pm) + u(f_w^\pm - f_w)}{k f_w \lambda_g \dfrac{\mathrm{d}P_c}{\mathrm{d}S_w}} \,. \tag{3.9}$$

Notice that (3.9) is well defined since $f_w\lambda_g \mathrm{d}P_c/\mathrm{d}S_w \neq 0$ for $P_c$ from (2.24). Applying the chain rule to the second equation of (3.5) and using (3.7), we obtain:

$$\frac{\mathrm{d}n_D}{\mathrm{d}\eta} = \frac{\phi S_g \Phi}{u(1 - f_w^\pm) - \nu\phi S_g^\pm} \,. \tag{3.10}$$

To study the traveling wave solution, we use the phase space analysis, following Lozano et al. (2021, 2022). Hence, we need the system (3.5) to be written in the standard ODE form, *i.e.*, $\mathrm{d}U/\mathrm{d}\eta$ explicitly written as a function of $U = (S_w, n_D)$. The authors Ashoori et al. (2011); Lozano et al. (2021, 2022); and Zavala et al. (2022) show how to obtain this standard form for some Newtonian models. However, it is not trivial to perform the same procedure for the present non-Newtonian model because of the intricate dependency of $\mu_f$ on $\mathrm{d}S_w/\mathrm{d}\eta$, see Eq. (3.3). A simplification we assume in this chapter consists of considering an approximated value of $\mu_f$ by considering $\mathrm{d}S_w/\mathrm{d}x = 0$ only inside the formula (3.3). Further, we show that this simplification does not affect the simulation results for the experimental parameters.

A traveling wave solution for this foam model is defined as a solution $U = (S_w, n_D)$ for the system of ODEs (3.9)-(3.10), which satisfies (3.6) for given constant states $U^-$ and $U^+$. These states must be equilibria of that system, *i.e.*, $\mathrm{d}U/\mathrm{d}\eta\,(U^\pm) = 0$. From (3.9), we know all possible equilibria must be on a straight line:

$$\frac{\mathrm{d}S_w}{\mathrm{d}\eta} = 0 \qquad \leftrightarrow \qquad \frac{f_w - f_w^\pm}{S_w - S_w^\pm} = \frac{\nu\phi}{u} \,. \tag{3.11}$$

From (3.10), an equilibrium must also satisfy:

$$\frac{\mathrm{d}n_D}{\mathrm{d}\eta} = 0 \qquad \leftrightarrow \qquad S_g = 0 \quad \text{or} \quad \Phi = 0 \,. \tag{3.12}$$

Points $(S_w, n_D)$, where $\Phi = 0$, are called local equilibria because the rates of generation and destruction of foam there are equal (Ma et al., 2014a). Differently from the Newtonian

cases treated in (Lozano et al., 2021; Zavala et al., 2022) and in Appendix A (Lozano et al., 2022), finding local equilibria as a function of $S_w$ for the non-Newtonian model studied here is challenging. That is why we numerically obtain a set of local equilibria points $(S_w, n_D)^{\mathrm{LE}}$. This set is a curve for applications studied in this chapter, similar to what happens in other foam displacement models, as described by Kam (2008); Ashoori et al. (2011); Lozano et al. (2021); and others. Notice that all equilibria of the System (3.9)-(3.10) are located at the intersection of curve $(S_w, n_D)^{\mathrm{LE}}$ with the straight line in Eq. (3.11). The graphical representation of this intersection for the experimental data by Chen et al. (2010) is shown in Section **3.3.1**.

**Remark:** *Chen et al. (2010) performed numerical simulations for a local equilibrium version of Model B, presenting a formulation for $n_D^{LE}$ that depends on phase velocities $v_w$ and $v_g$ (which we also introduce later in Section **5.1.2**). However, in the context of this chapter, where we apply fractional flow theory, explicitly evaluating $n_D^{LE}$ using that formulation is nontrivial, as $v_w$ and $v_g$ are expressed as functions of $n_D$.*

The existence of a traveling wave connecting $U^-$ to $U^+$ depends on the type of ODE system's equilibria, which are classified according to the eigenvalues of the corresponding Jacobian matrix; for more details, see (Volpert et al., 2000; Lozano et al., 2021). In this chapter, we only deal with two types of hyperbolic equilibria: the one with real and positive eigenvalues is called a source (or repeller); the other one, presenting real eigenvalues with opposite signs, is called a saddle; see (Guckenheimer and Holmes, 1986; Ghazaryan et al., 2022) for details. In this chapter, a traveling wave connects the left source to the right saddle.

In the next section, we follow the same procedure as Lozano et al. (2021) to numerically obtain the traveling wave connection by integrating the ODEs (3.9)-(3.10). A connection from equilibrium $U^-$ to $U^+$ exists if and only if there is a point $U_0$ in the phase space, such that the ODE solution starting at $U_0$ for positive $\eta$ (*i.e.*, when $\eta \to +\infty$) tends to $U^+$; and the ODE solution starting at $U_0$ for negative $\eta$ (*i.e.*, when $\eta \to -\infty$) tends to $U^-$ (Volpert et al., 2000; Ghazaryan et al., 2022). For the case this chapter investigates, $U^-$ is a source, and $U^+$ is a saddle. In the neighborhood of the equilibrium $U^+$, the direction of the solution approaching this equilibrium coincides with the eigenvector of the corresponding Jacobian matrix at $U^+$ associated with the negative eigenvalue (Guckenheimer and Holmes, 1986). That is why the starting point for the numerical integration is chosen close to $U^+$ in the direction of the later eigenvector. The solution is constructed by integrating the ODE until reaching neighborhoods of both equilibria.

Finally, for each time $t$, we obtain the solution $U = (S_w, n_D)$ changing back the variable $\eta$ to $x$ using (3.4), with the velocity $\nu$ given in (3.8).

## 3.3 MATCHING THE LABORATORY EXPERIMENT

The experiment conducted by Chen et al. (2010) involves a continuous co-injection of nitrogen gas and surfactant solution into a cylinder core of Berea sandstone, 5.08 cm in diameter and $L = 60$ cm long. The core is quite homogeneous with average porosity and permeability summarized in Table 3.1. The injecting surfactant solution is a 1.0 wt% sodium C14-16 olefin sulfonate in a 0.5 wt% sodium chloride brine. The author obtained the core characterization and the *in-situ* measurements of water saturation through an X-ray CT scanner.

In the present chapter, we use the same parameter values as Chen et al. (2010), except for $P_c^*$. The constant value of $P_c^*$ was estimated using the limiting capillary pressure equation provided by authors for high values of surfactant concentration. All parameter values are summarized in Table 3.1.

Table 3.1 – Model parameters for foam flow simulation.

| Two-phase flow | | Population balance | |
|---|---|---|---|
| Parameter | Value | Parameter | Value |
| $\phi$ | 0.18 | $\alpha$ | $7.4 \cdot 10^{-18}$ Pas$^{2/3}$m$^{10/3}$ |
| $\mu_g$ | $1.8 \cdot 10^{-5}$ Pa · s | $\beta$ | $10^{-9}$ m$^3$ |
| $\mu_w$ | $1.0 \cdot 10^{-3}$ Pa · s | $k_1^0$ | $1.65 \cdot 10^{15}$ s$^{1/3}$m$^{13/3}$ |
| $\sigma_{wg}$ | 0.033 N/m | $k_{-1}^0$ | 10 m$^{-1}$ |
| $k$ | $3 \cdot 10^{-13}$ m$^2$ | $n_{\max}$ | $10^{12}$ m$^{-3}$ |
| $k_{rg}^0$ | 1.0 | $P_c^*$ | $3 \cdot 10^4$ Pa |
| $k_{rw}^0$ | 0.7 | $X_{t,\max}$ | 0.78 |
| $n_g$ | 3 | | |
| $n_w$ | 3 | | |
| $S_{wc}$ | 0.38 | | |
| $u$ | $1.45 \cdot 10^{-5}$ m/s | | |

### 3.3.1 Finding equilibria

As explained in Section 3.2, the first step to find a traveling solution is to identify the equilibria of system (3.9)-(3.10), *i.e.*, points $(S_w, n_D)$ that satisfy conditions (3.11) and (3.12). Figure 3.1 presents the local equilibrium points $(S_w, n_D)^{\text{LE}}$ satisfying (3.12).

From experiments reported by Chen et al. (2010), we obtained the values of $S_w^-$ and $S_w^+$. Since the system of ODEs is not well defined for $S_w = 1$ (see Eq. (3.3)), we approximate the resident water saturation as $S_w^+ = 0.999$. A similar approximation was used by Zavala et al. (2022). Using the local equilibrium curve from Figure 3.1 together

Figure 3.1 – Local equilibrium points $(S_w, n_D)^{\mathrm{LE}}$ satisfying (3.12).

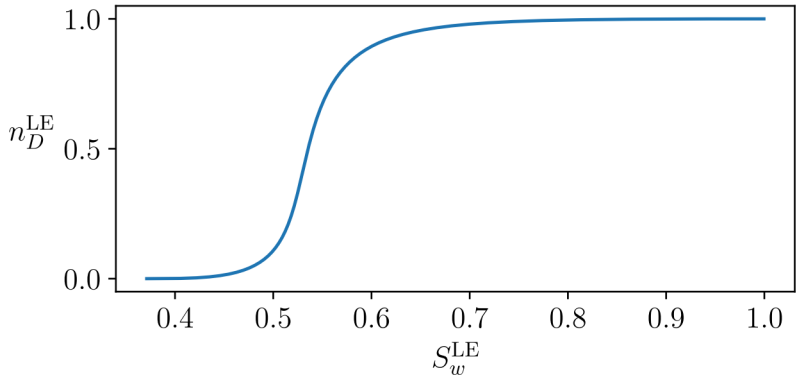


Source: Elaborated by the author (2024).

Figure 3.2 – Graphical representation of three equilibria of System (3.9)-(3.10). The blue solid curve represents the fractional flow $f_w$ for the local equilibria $(S_w, n_D)^{\mathrm{LE}}$ from Figure 3.1 (*i.e.*, condition (3.11)). The black traced line represents the condition (3.12). The black circle indicates the third equilibrium.

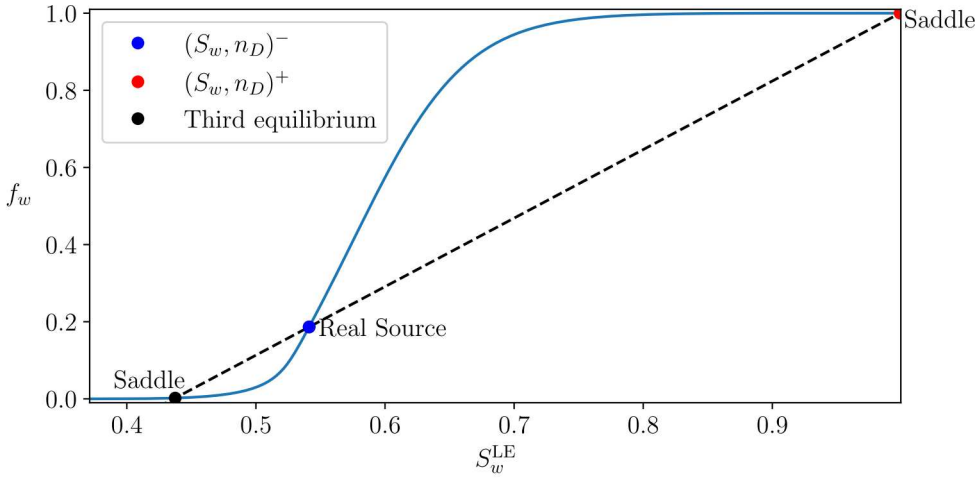


Source: Elaborated by the author (2024).

with $S_w^-$ and $S_w^+$ we find $n_D^-$ and $n_D^+$:

$$\begin{aligned} U^- &= (S_w^-, n_D^-) = (0.550,\, 0.595)\,, \\ U^+ &= (S_w^+, n_D^+) = (0.999,\, 1.000)\,. \end{aligned} \tag{3.13}$$

Using (3.13) with condition (3.12), we obtain all possible equilibria of System (3.9)-(3.10). Figure 3.2 shows three such equilibria.

### 3.3.2 Finding the traveling wave solution

Applying the procedure presented in Section 3.2, we numerically integrate the ODEs (3.9)-(3.10) to find the traveling wave path connecting left and right equilibria

Figure 3.3 – Solution of system of ODEs (3.9)-(3.10) for the case (3.13). In the left figure, the system's phase portrait shows a source-saddle connection from the left to the right state. In the right figure, we show the profiles corresponding to the black path found in the left figure.

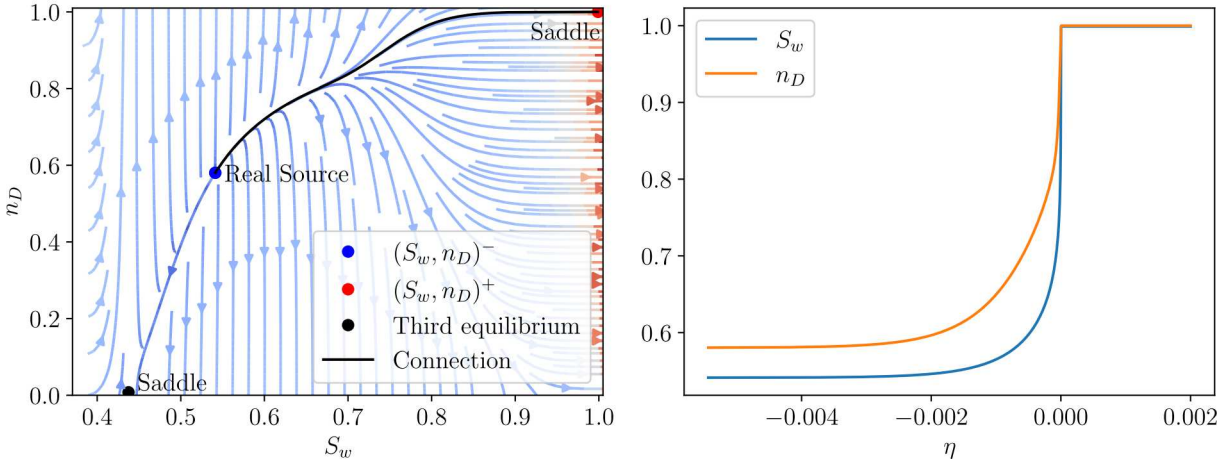


Source: Elaborated by the author (2024).

in the phase space. Figure 3.3 presents that solution both in the phase space and as a function of the traveling variable $\eta$. We also present this solution as a function of original variables $x$ and $t$ in Section **3.3.3**. Using the expression (3.8), we calculate the traveling wave velocity $v = 1.4394 \cdot 10^{-4}\,\mathrm{m/s}$, which coincides with the wavefront velocity estimated from the experimental data by Chen et al. (2010).

In this section, we validate the analytical estimates with direct numerical simulations using the method described in Appendix B.1. In these simulations, we kept the term $\mathrm{d}P_c/\mathrm{d}x$ in Eq. (3.3) one timestep behind. Notice that this is not a simplification of the model but rather a discretization choice made to align the model with the solver's standards. We set the initial and boundary conditions of the system to replicate the experiment performed by Chen et al. (2010), with the values presented in (3.13). We defined the constant initial condition $(S_w^+, n_D^+)$ of the reservoir, a Dirichlet boundary condition on the left side to simulate a fixed injection value $(S_w^-, n_D^-)$ and a homogeneous Neumann condition at the right side to simulate an infinite domain outlet condition.

### 3.3.3 Results and discussions

Figure 3.4 compares the water saturation profiles obtained from the semi-analytical traveling wave solution, the numerical simulations, and the original experimental data (Chen et al., 2010). The traveling wave solution used assumptions detailed in Section 3.2, while the numerical simulation deals with the original model without simplifications. The figure shows a perfect match between numerical and semi-analytical solutions, verifying

Figure 3.4 – Water saturation profiles of experimental (Chen et al., 2010), semi-analytical and numerical results.

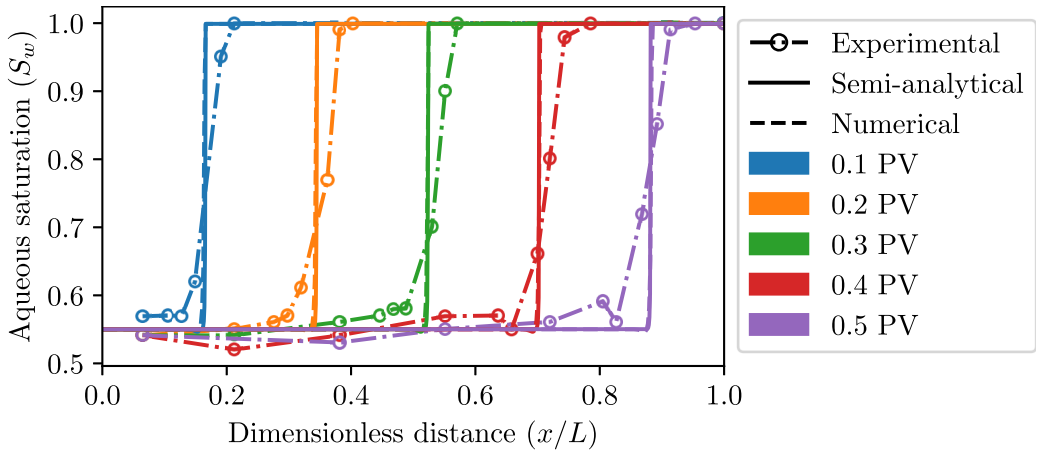


Source: Elaborated by the author (2024).

the existence of the traveling wave solution in this model. This match also evidences that the traveling wave hypothesis and the simplification made in Eq. (3.3) do not affect the solution of the model for the studied parameters. The agreement with the analytical solution evidences that the chosen numerical method can solve the investigated model accurately. On the other side, Fig. 3.4 shows good agreement of both mathematical and numerical solutions with experimental data capturing piston-like water saturation profiles. Notice that the simple incompressible one-dimensional model presented can describe the experiment's wavefront velocity. However, the model presents water saturation profiles that are sharper than those of the experiments. This may be attributed to the diffusive effects of heterogeneity, which are not captured in a one-dimensional model. The shock-like profiles Model B presented in Figure 3.4 can be obtained through other simpler models (*e.g.*, Models A, C, and others).

Figure 3.5 compares numerical and analytical results for both water saturation and foam density profiles. The latter we define as the number of bubbles per porous volume ($S_g \cdot n_D$). There is no significant difference between analytical and numerical water saturation and foam density profiles. State of the art in experimental measuring of the foam flow in porous media involves the micro CT-scan (Simjoo et al., 2013a; Simjoo and Zitha, 2015; Chen et al., 2010; Zavala et al., 2022), which cannot provide the foam density directly as the latter presents the same density as the gas phase. Most estimations are made indirectly by using the changes in pressure drop in the presence of foam. Figure 3.5 provides the foam density profiles inside the core; however, comparing them to experimental data is currently impossible.

As stated above, the match between the semi-analytical and numerical water saturation profiles evidences the existence of the traveling wave solution for the original

Figure 3.5 – Numerical simulation and the traveling wave solutions for case (3.13).

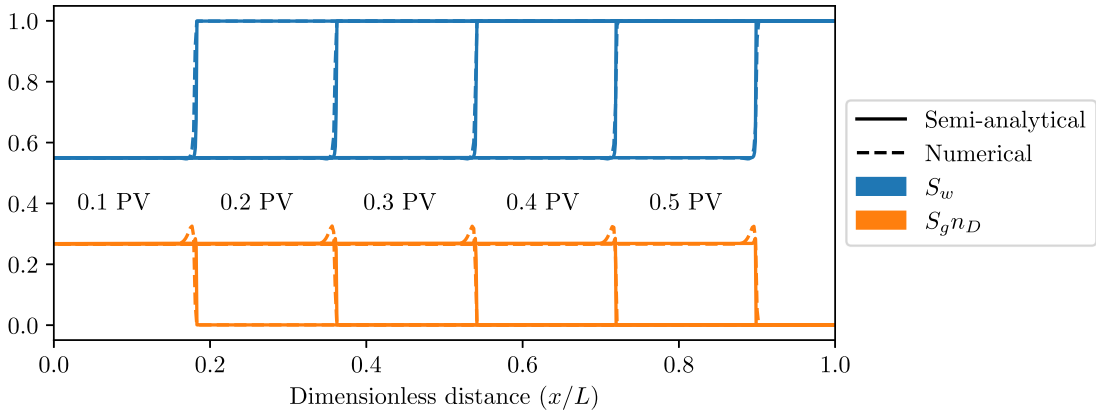


Source: Elaborated by the author (2024).

model. The same conclusion is not so obvious for the experimental data. We measure the distance between the numerical and experimental profiles using the mean percentage squared error (MPSE), defined as:

$$\text{MPSE} = \sqrt{\frac{1}{L}\int_0^L \left(\frac{\tilde{S_w}(x) - p_1(x)}{p_1(x)}\right)^2 \mathrm{d}x}\,, \qquad p_1(x) \approx S_w(x)\,, \tag{3.14}$$

where $\tilde{S_w}$ is the numerical solution and $p_1$ is the linear interpolation of experimental water saturation $S_w$. Figure 3.6 shows that the most significant values of MPSE are located close to the wavefront. Notice that the maximum relative difference is less than 6% and remains stable over time, *i.e.*, the experimental profile moves without changing its shape and can be mathematically described as a traveling wave.

Figure 3.6 – Percentage squared differences between numerical results and experimental data for water saturation.

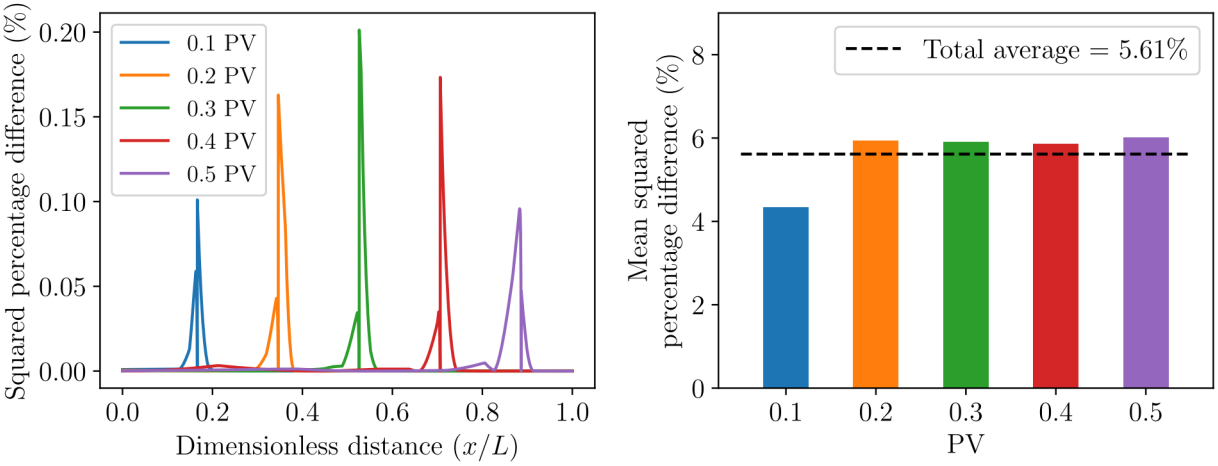


Source: Elaborated by the author (2024).

Finally, let us validate the simplification in foam apparent viscosity $\mu_f$, presented

Figure 3.7 – Comparison between the values of $\mu_f$ for original and simplified versions of Eq. (3.3), at 0.2 PV. At the right is the relative difference between the simplified solution and the original formula.

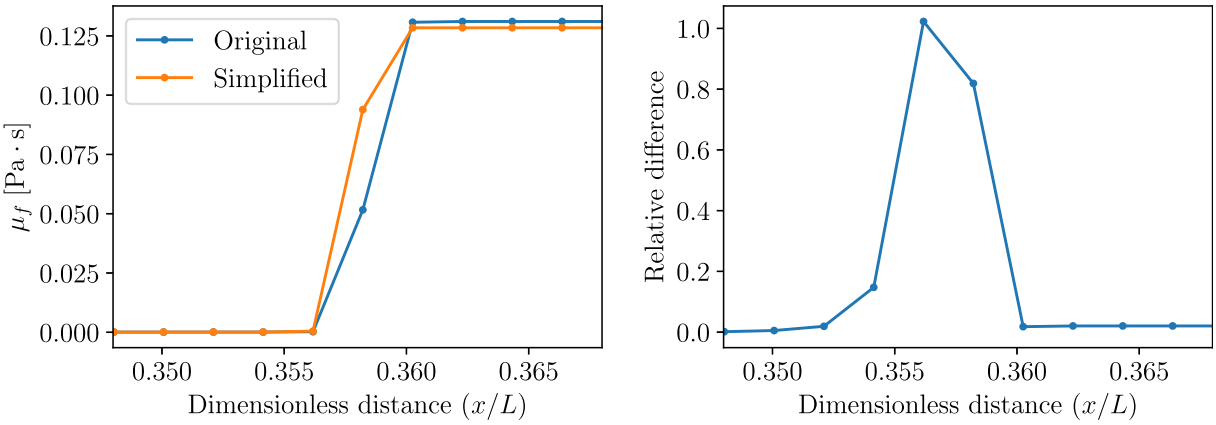


Source: Elaborated by the author (2024).

in Section 3.2, and used in the traveling wave analysis. We calculate the values of $\mu_f$ with and without such simplification for each numerical solution point and plot the results in Figure 3.7. We see that the major relative difference is located at the wavefront, affecting only a small domain region. The relative difference is lower than 2.03% except for the wavefront. As the difference between semi-analytical and numerical profiles in Figure 3.4 is negligible in most parts of the domain, this issue is not observed for the water saturation profiles. However, it can be observed in Figure 3.5 for the foam texture profiles.

## 3.4 PARTIAL CONCLUSIONS

The study presented in this chapter shows that the non-Newtonian model commonly used to describe the foam displacement in a porous medium presents a traveling wave solution. Direct numerical simulations supported our analysis.

These results agree with the experimental observations, as we verified that the experimental profile moves without changing its shape and can be mathematically described as a traveling wave. The analytically obtained traveling wave velocity estimate coincides with the experimentally obtained average wavefront velocity.

We noticed that the presented analytical solution is similar to the ones obtained by solving simpler models. The analytical profile is sharper than the experimental one.

The results of this chapter might be a starting point in the study of traveling waves for non-Newtonian foam in radial flow, which more resembles injection applications and inherently features a flow velocity decaying with radial distance.

# 4 COMPARING TRAVELING WAVE SOLUTIONS FOR THE THREE MODELS

In Chapter 3 (Cedro and Chapiro, 2024), we obtained a traveling wave solution for Model B, obtaining saturation and foam texture profiles similar to those reported by Fritis et al. (2022) and Zavala et al. (2022) for Models A and C, respectively. These two models, with parameters fitted to the experimental data from Simjoo and Zitha (2015), yield traveling wave solutions characterized by a piston-like shape. In this chapter, we adjust Model B to identify traveling wave solutions for this same data and compare them with those in the literature. Our findings show that, for parameters in Simjoo and Zitha (2015), all models present the same classification of traveling wave solutions and produce similar solution profiles.

## 4.1 ADJUSTING MODEL B

Simjoo et al. (2013b) conducted foam coreflood experiments to investigate the dependence of foam mobility on surfactant concentration and total injection velocity in natural sandstones in the absence of oil. Simjoo and Zitha (2015) performed similar experiments and fitted parameters of Model C (Section **2.4.3**) to their data. In this section, we also fit Model B (Section **2.4.2**) to these experimental data by adjusting both model descriptions on foam generation rate, gas trapping, and foam apparent viscosity.

### 4.1.1 Experimental data

Simjoo and Zitha (2015) conducted experiments using a Bentheimer sandstone core, reported as quasi-homogeneous and isotropic, with dimensions of 38.4 cm in length, and 3.8 cm in diameter. Core characterization and *in-situ* saturation measurements were performed using an X-ray CT scanner. The foam was generated by co-injecting nitrogen and a solution containing 0.5 mol/L sodium chloride and 1 wt% C14-16 AOS surfactant, with a CMC of $4.0 \times 10^{-3}$ wt%. The experiments were conducted at ambient temperature (approximately 21°C) and backpressure of 20 bar, maintaining a constant foam quality of 91%. The total superficial velocity at injection was $1.62 \cdot 10^{-5}$ m/s, and the absolute permeability was 2.5 Darcy. The authors also fitted Model C parameters to their experimental data, as summarized in Table 4.1.

Table 4.1 – Experimental and model parameters by Simjoo and Zitha (2015)

| | Parameter | Value |
|---|---|---|
| $\alpha$ | Viscosity proportionality const. | $5.8 \cdot 10^{-16}$ Pa $\cdot$ s$^{2/3}$m$^{10/3}$ |
| $\xi$ | Capillary pressure coefficient | 0.5 |
| $\theta$ | Contact angle | 0 rad |
| $\phi$ | Porosity | 0.21 |
| $\omega$ | Pore-size-distribution parameter | 5.0 |
| $\mu_g$ | Gas viscosity | $1.8 \cdot 10^{-5}$ Pa $\cdot$ s |
| $\mu_w$ | Water viscosity | $1.0 \cdot 10^{-3}$ Pa $\cdot$ s |
| $\sigma_{wg}$ | Gas-water interfacial tension | 0.03 N/m |
| $k$ | Absolute permeability | $2.5 \cdot 10^{-12}$ m$^2$ |
| $k^0_{rw}$ | Water endpoint relative perm. | 0.75 |
| $k^0_{rg}$ | Foam endpoint relative perm. | 1.0 |
| $K_d$ | Bubble coalescence coefficient | 0 s$^{-1}$ |
| $K_g$ | Bubble generation coefficient | 0.1 s$^{-1}$ |
| $n_{\max}$ | Maximum foam texture | $2.5 \cdot 10^{11}$ m$^{-3}$ |
| $r$ | Mean pore radius | $5 \cdot 10^{-6}$ m |
| $S_{wc}$ | Connate water saturation | 0.10 |
| $u_g$ | Gas velocity | $1.471 \cdot 10^{-5}$ m/s |
| $u_w$ | Water velocity | $1.446 \cdot 10^{-6}$ m/s |

### 4.1.2 Relative permeability and capillarity

In this study, we adopt the same relative permeability as Simjoo and Zitha (2015), given by:

$$k_{rw} = k^0_{rw}\left(\frac{S_w - S_{wc}}{1 - S_{wc}}\right)^{\omega} \quad \text{and} \quad k_{rg} = k^0_{rg}\left(\frac{1 - S_w}{1 - S_{wc}}\right)^{\frac{3\omega+2}{\omega}}, \quad \text{with} \quad \omega = 5\,, \tag{4.1}$$

where $\omega$ is the pore-size distribution parameter. The capillary pressure is defined based on microscopic pore-fluid interactions:

$$P_c = 2\,\xi\,\sigma_{wg}\,\frac{\cos(\theta)}{r}\left(\frac{S_w - S_{wc}}{0.5 - S_{wc}}\right)^{-1/\omega}, \tag{4.2}$$

where $\xi$ is a proportionality coefficient, $\sigma_{wg}$ is the interfacial tension between water and gas, $\theta$ is the contact angle between the wetting phase and pore walls, and $r$ is the effective pore radius. This radius is proportional to the macroscopic properties permeability ($k$) and porosity ($\phi$), with $r \propto \sqrt{k/\phi}$, which links Eq. (4.2) to the upscaled J-Leverett form (2.15).

### 4.1.3 Foam's apparent viscosity

Models B and C share the shear-thinning behavior described by the Hirasaki-Lawson relation (2.28). However, Model C does not incorporate trapped foam. The natural choice to equate the apparent viscosity between these models is to consider Model C with a foam flow fraction $X_f = 1$, *i.e.*, a particular case of Model B. By doing this, the coefficient $\alpha$ remains the same as fitted by Simjoo and Zitha (2015).

### 4.1.4 Foam generation and destruction rates

Following the approach of Model C's authors (Zitha and Du, 2010), Simjoo and Zitha (2015) also assumed a zero foam destruction rate ($K_d$), considering it negligible compared to the generation rate ($K_g$) for strong foam. Although equating the complex foam source term of Model B (2.29) with that of Model C (2.30) is challenging, we set the coalescence rate to $r_c = 0$ in Model B to match $K_d = 0$. By doing this, we avoid the need to fit a value for the limiting capillary pressure, $P_c^*$. Notice that, in Model B, if $k_{-1}^0 = 0$, then $n_D^{\mathrm{LE}} = 1$, just as Model C.

The generation rate in both models follows the idea of limiting bubble generation using a logistic term. Model C employs a classical logistic model, while Model B uses a generalized version with a cubic exponent for foam texture $n_D$. To ensure this adjustment remains independent of $n_D$, we focus on fitting only the coefficients of the growth restriction terms, $(1 - n_D)$ in Model C and $(1 - n_D^3)$ in Model B, rather than modifying the shape of these logistic factors. Doing so, from (2.29) and (2.30), we can write:

$$k_1^0 = \frac{K_g n_{\max}}{\|\mathbf{v}_w\| \, \|\mathbf{v}_g\|^{1/3}} \, . \tag{4.3}$$

Therefore, we fit the generation rate coefficient $k_1^0$ as a function of interstitial phase velocities $v_g$ and $v_w$. The experimental data by Simjoo and Zitha (2015) were obtained under fixed superficial velocities $u_g$ and $u_w$ given in Table 4.1. Thus, $v_g$ and $v_w$ can be retrieved using Eq. (2.10), for a given water saturation $S_w$.

We choose the value of $S_w$ based on the steady-state water saturation predicted by the model for the injection conditions reported in the experiments, fractional gas flow $\bar{f}_g = 91\%$. Thus we evaluate the local equilibrium fractional flow curve, following a similar approach to Section **3.3.1**, and obtain that, in local equilibrium, the experimental injection condition corresponds to steady water saturation of $\bar{S_w} = 0.4479$, *i.e.*, $f_w^{\mathrm{LE}}(\bar{S_w}) = 1 - \bar{f}_g$. For this water saturation, we obtain $k_1^0 = 3.18425 \cdot 10^{16}$ $\mathrm{s}^{1/3}\mathrm{m}^{13/3}$. Notice that, since $k_{-1}^0 = 0$, the function $f_w^{\mathrm{LE}}(S_w)$ does not depend on the parameter $k_1^0$, which we are fitting.

## 4.2 TRAVELING WAVE SOLUTION

The procedure to find a traveling wave solution for Model B was described in Sections 3.2 and 3.3. That solutions is described by the system of ODEs (3.9)-(3.10), satisfying (3.11)-(3.12). However, in this section, we find a solution for the relative permeability and capillary pressure functions given by (4.1) and (4.2), and for parameters in Table 4.1. The first step in obtaining a traveling wave solution is to determine the equilibrium points of system (3.9)-(3.10), *i.e.*, the points $U = (S_w, n_D)$ that satisfy conditions (3.11)-(3.12). Since $k_{-1}^0 = 0$, we know that $n_D^{\mathrm{LE}} = 1$ satisfies condition (3.12), for any value of $S_w$.

In our study, we assume that the porous medium is initially saturated with a surfactant solution. However, since the system of ODEs is not well-defined for $S_w = 1$ (see Eq. (3.3)), we approximate the downstream saturation as $S_w^+ = 0.999$, as done in our analysis in Section **3.3.1** and by Zavala et al. (2022). Following the procedure presented in that section, we seek traveling wave solutions for a given $S_w^-$. Depending on the chosen $S_w^-$, the set of equilibria and the existence of a solution may change. Figure 4.1 provides a graphical representation of equilibria and traveling wave connections for some values of $S_w^-$ (recall that $n_D^{\mathrm{LE}}$ is always 1), illustrating four cases:

(a) In Fig. 4.1a, there are three equilibria: the left and right states, $U^-$ and $U^+$, and a third equilibrium, $U^{\mathrm{e}}$. The phase portrait shows that no connection exists between $U^-$ and $U^+$.

(b) In Fig. 4.1b, the dashed black line is tangent to the $f_w^{\mathrm{LE}}$ curve (blue line) at $S_w^- = S_w^T = 0.4468$, meaning that the system has only the equilibria $U^-$ and $U^+$. This scenario presents a saddle-saddle connection and marks the transition between the cases shown in Figs. 4.1a ($S_w^- < S_w^T$) and 4.1d ($S_w^- > S_w^T$).

(c) In Fig. 4.1c, there are three equilibria, similar to Fig. 4.1b, but with the values of $S_w^-$ and $S_w^e$ swapped. In this case, a connection from $U^-$ to $U^+$ is possible.

(d) In Fig. 4.1d, only two equilibria exist with a source-saddle connection from $U^-$ to $U^+$.

To compare our semi-analytical solution to laboratory experiments, we set $S_w^-$ to the steady-state value $\bar{S_w} = 0.4479$, corresponding to the reported injection fractional flow $\bar{f}_g = 91\%$. This case corresponds to the one shown in Fig. 4.1c, where there is a traveling wave connection. To validate our approach, we conducted numerical simulations replicating the experiment by Simjoo and Zitha (2015), using the parameters from Table (4.1) – see the numerical methodology in Appendix B. The initial condition was set as $S_w = 1$ and

Figure 4.1 – Graphical representation of equilibria in the traveling wave ODE system for selected some of $S_w^-$ at a fixed $S_w^+ = 0.999$. The upper panels display the equilibrium conditions (3.11) (blue line) and (3.12) (black dashed line) in the $S_w \times f_w$ plane. The lower panels present the corresponding phase portraits in the $S_w \times n_D$ plane, indicating whether a connection exists between $U^-$ and $U^+$. In some cases, there is a third equilibrium denoted as $U^e$.

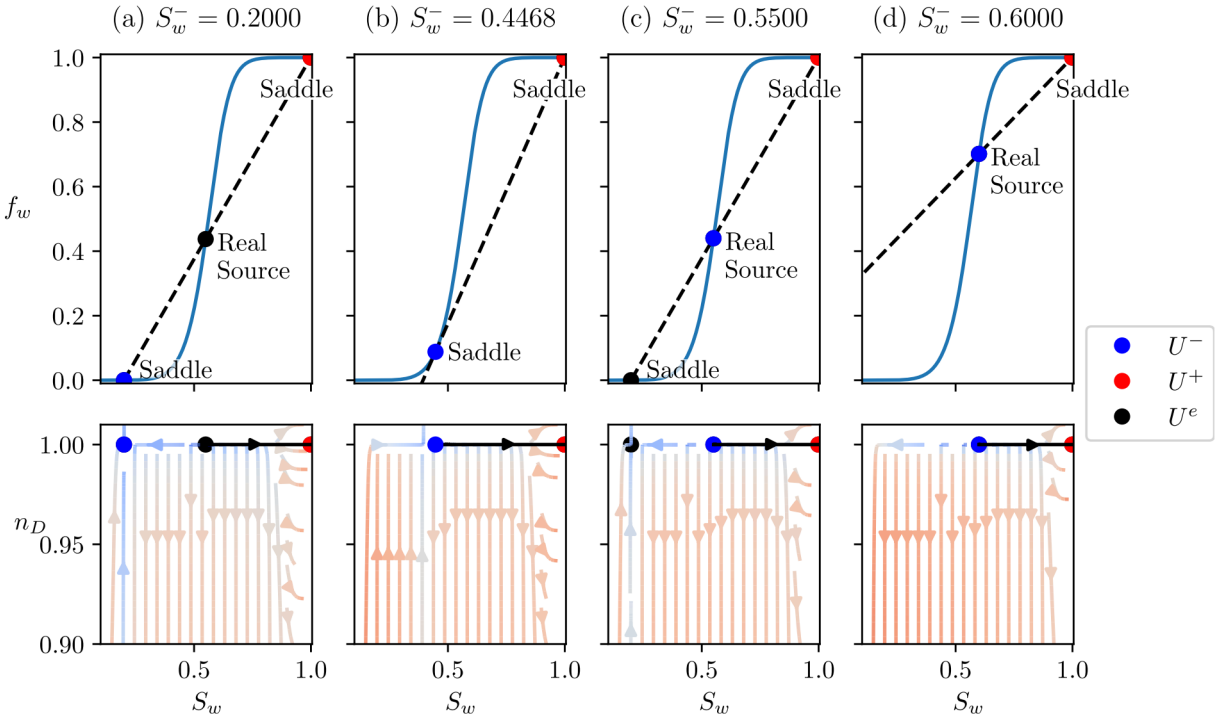


Source: Elaborated by the author (2025).

Figure 4.2 – Semi-analytical and numerical water saturation profiles for Model B fitted to experimental data by Simjoo and Zitha (2015).

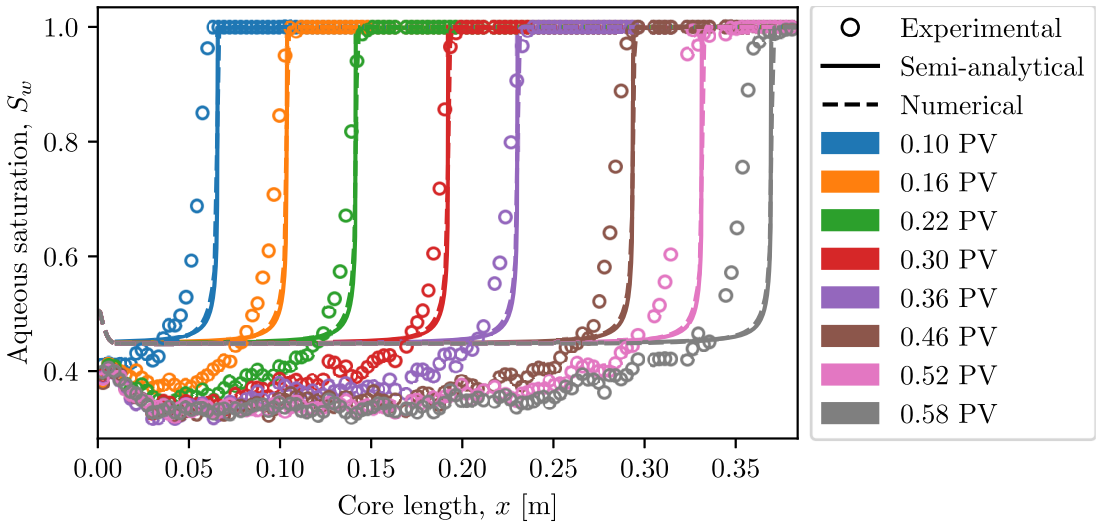


Source: Elaborated by the author (2025).

$n_D = 0$, with a fixed gas fractional flow $\bar{f}_g$ at the left boundary and a homogeneous Neumann condition at the right boundary to simulate an infinite domain outlet.

In Fig. 4.2, we present the water saturation profiles from the experiment alongside the numerical results and the traveling wave solution, plotted in the original variable $x$, with time $t$ represented by the injected porous volume (PV). In contrast to the experiment shown in Fig. 3.4, which exhibits simple piston-like profiles, the experiment in Fig. 4.2 reveals a more complex behavior. It shows an initial water saturation decay to $S_w = 0.35$ within the first 3 cm of core length, followed by a spreading wave reaching $S_w = 0.45$, and then a traveling wave to $S_w = 1$. Both numerical and semi-analytical solutions successfully capture this traveling wave and satisfactorily predict the gas front position. However, the adjusted Model B is limited in representing the profiles upstream of the traveling wave, overestimating the steady upstream water saturation. The same behavior is present in the simulations of Model C reported by Simjoo and Zitha (2015). Additionally, Zavala et al. (2022) presented numerical simulations of Model C that exhibit this spreading wave when the injection condition is set to $S_w < 0.45$.

Figure 4.3 present numerical profiles of water saturation ($S_w$) and bubble density ($S_g \cdot n_D$) for Models A, B, and C. To simulate Model A, we set $S_w^* = 0.37$ and $A = 400$ based on Ashoori et al. (2011). The generation rate coefficient is taken to be the same as in Model C, *i.e.*, $K_c = K_g = 0.1\,\mathrm{s}^{-1}$. We estimate the mobility reduction factor by equating the foam apparent viscosity $\mu_f$ in Eqs. (2.25) and (2.28), following the approach of Zavala et al. (2022). Thus, $C_{\mathrm{MRF}} = \alpha n_{\max}/(\mu_f v_g^{1/3}) = 149$, where $v_g$ is evaluated without trapped gas ($X_f = 1$) and with $S_w = 0.4479$, corresponding to the steady upstream water saturation. The profiles in Figure 4.3 show that all models, with parameters from Table 4.1, yield exactly the same solution, demonstrating the equivalence of these three models under the adjustments performed in this study.

### 4.2.1 Solution classification

In this section, we expand on the examples from Fig. 4.1 and classify the possible traveling wave solutions based on the number and type of equilibria of the system. Lozano et al. (2022) and Fritis et al. (2022) previously classified equilibria in Model A as a function of upstream water saturation $S_w^-$ and the kinetic parameter for foam generation $K_c$. Similarly, Zavala et al. (2022) made the same classification for Model C in terms of $S_w^-$ and the generation rate $K_g$. For comparison, we follow this approach and present the classification of Model B in the parameter space of $S_w^-$ and the generation coefficient $k_1^0$.

Figure 4.4 displays the equilibria classification for all models fitted to the experimental data from Simjoo and Zitha (2015). In Fig. 4.4a, the classification of Model A (Fritis et al., 2022) is shown, with a small region near $S_w^*$ highlighted by a dashed rectangle,

Figure 4.3 – Water saturation ($S_w$) and bubble density ($S_g \cdot n_D$) profiles of numerical simulations for Models A, B and C, fitted to experimental data (Simjoo and Zitha, 2015).

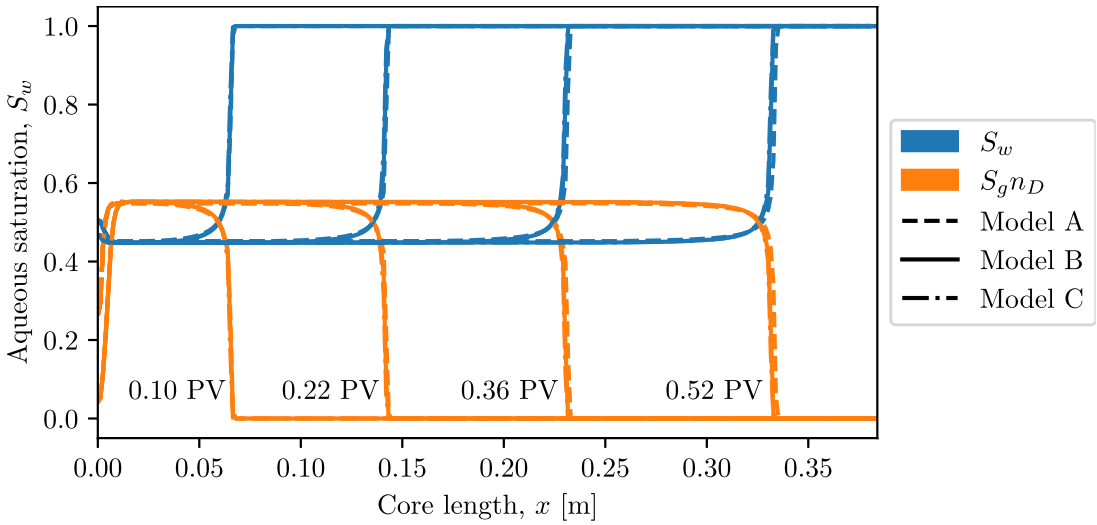


Source: Elaborated by the author (2025).

Table 4.2 – Classification regions based on equilibria types.

| **Region** | $U^-$ | $U^+$ |
|---|---|---|
| I | Real Source | Saddle |
| II | Saddle | Saddle |
| III | Complex Source | Saddle |
| IV | Complex Sink | Saddle |
| V | Real Sink | Saddle |

which is zoomed in Fig. 4.4b. Figure 4.4c presents the classification of Model C (Zavala et al., 2022), while Fig. 4.4d shows the classification of Model B. The vertical axis in all models, representing the generation rate coefficient, ranges from zero to the fitted value of each parameter – $K_c$, $K_g$, and $k_1^0$ – in their respective models.

The classifications depicted in Fig. 4.4 define five regions, which we detail in Table 4.2. In summary, all models exhibit nearly identical regions, with the exception of a small interval near $S_w^*$ in Model A, which includes Regions I, III, IV, and V. Models B and C only feature Regions I and II, where a solution exists exclusively in Region I. A solution is present in all models within Region I. In Fig. 4.4d, the solid black line represents the boundary between Region I, where a traveling wave solution exists, and Region II, where no solution is possible. This transition corresponds to the scenario illustrated in Fig. 4.1b. The dashed black line represents the transition from a region with three equilibria (*e.g.*, Fig. 4.1c) to a region with only two equilibria (*e.g.*, Fig. 4.1d). Figure 4.4 also includes points labeled with calligraphic letters to indicate numerical, analytical, or experimental cases studied by the authors (Zavala et al., 2022; Fritis et al., 2022). The experiment we investigate in this work (shown in Fig. 4.2) corresponds to point $\mathcal{A}$, near the transition between Regions I and II.

Figure 4.4 – Equilibria classification for Models A, B, and C fitted to the experimental data from Simjoo and Zitha (2015). The green point $\mathcal{A}$ in panels (a), (c), and (d) corresponds to their experiment.

(a) Model A (Fritis et al., 2022).

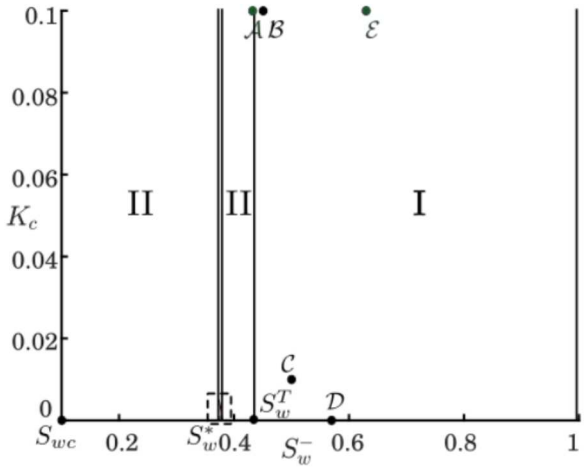


(b) Zoom at the rectangle in (a).

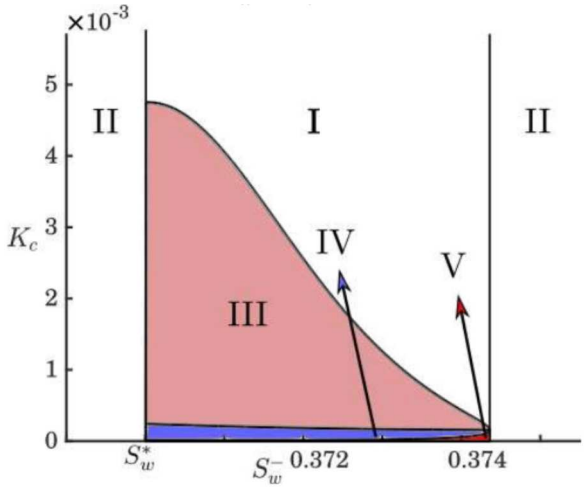


(c) Model C (Zavala et al., 2022).

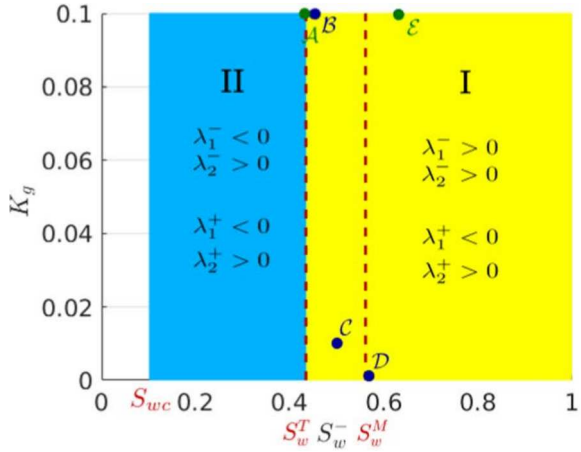


(d) Model B.

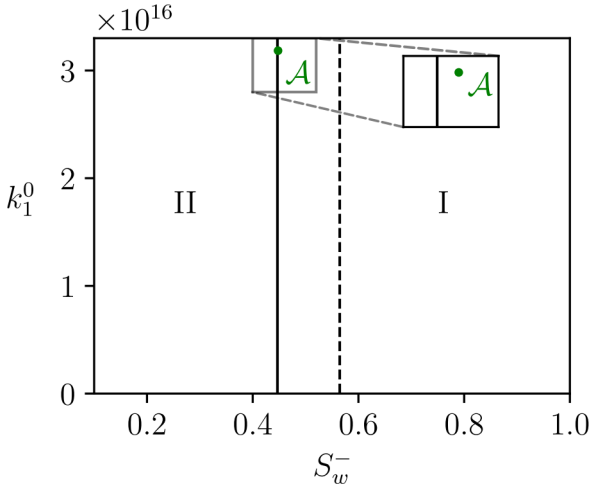


Source: Adapted from Fritis et al. (2022) and Zavala et al. (2022).

### 4.2.2 Summary of compared foam models

For a comprehensive overview of the foam flow models and analytical studies considered in this work, we present a summary in Tables 4.3 and 4.4. Table 4.3 outline the mathematical details of Models A, B, and C as proposed by the authors Ashoori et al. (2011), Chen et al. (2010), and Zitha and Du (2010), respectively. It is worth noting that we maintain the original equations governing bubble balance, foam rheology, and gas trapping throughout all numerical and analytical investigations in this work. Only the relative permeability ($k_{rg}$, $k_{rw}$) and capillary pressure ($P_c$) functions are modified when

adjusting a model to experimental measurements. For instance, in this chapter, we fitted all models to the data from Simjoo and Zitha (2015) using the same $k_{rg}$, $k_{rw}$, and $P_c$ as defined in Model C. Table 4.4 details the foam models considered in the traveling wave classification by Lozano et al. (2021), Zavala et al. (2022), and Fritis et al. (2022), along with the analyzed in the present work.

Table 4.3 – Details on foam flow Models A (Ashoori et al., 2011), B (Chen et al., 2010), and C (Zitha and Du, 2010), as originally proposed by their authors.

| | **Model A** | **Model B** | **Model C** |
|---|---|---|---|
| **Bubble Population Balance ($\Phi$)** | $K_c(n_D - n_D^{\mathrm{LE}})$ | $r_g - r_g$<br>$r_g = \dfrac{k_1^0}{n_{\max}}\left(1 - n_D^3\right)\|\mathbf{v}_w\|\,\|\mathbf{v}_g\|^{\frac{1}{3}}$<br>$r_c = k_{-1}^0\left(\dfrac{P_c}{P_c^* - P_c}\right)^2\|\mathbf{v}_g\|\,n_D$ | $K_g(1 - n_D) - K_d n_D$ |
| **Local Equilibrium Foam Texture ($\mathbf{n_D^{LE}}$)** | $\tanh(A(S_w - S_w^*))$ | $n_D^3 + \gamma n_D - 1 = 0$<br>$\gamma = n_{\max}\dfrac{k_{-1}^0\|\mathbf{v}_g\|^{2/3}}{k_1^0\|\mathbf{v}_w\|}\left(\dfrac{P_c}{P_c^* - P_c}\right)^2$ | $\dfrac{K_g}{K_g + K_d}$ |
| **Mobility Reduction Factor** | $1 + C_{\mathrm{MRF}} n_D$ | $1 + \alpha n_f / v_g^{1/3}$ | $1 + \alpha n_f / v_g^{1/3}$ |
| **Relative Permeabilities** | $k_{rw} = k_{rw}^0 {S_{wn}}^{n_w}$<br>$k_{rg} = k_{rg}^0 {S_{gn}}^{n_g}$<br>$n_w = 4.2,\ n_g = 1.3$ | $k_{rw} = k_{rw}^0 {S_{wn}}^{n_w}$<br>$k_{rg} = k_{rg}^0 (X_f S_{gn})^{n_g}$<br>$n_w = n_g = 3$ | $k_{rw} = k_{rw}^0 {S_{wn}}^{\omega}$<br>$k_{rg} = k_{rg}^0 {S_{gn}}^{\frac{3\omega+2}{\omega}}$<br>$\omega = 5$ |
| **Capillary Pressure ($\mathbf{P_c}$)** | $\sigma_{wg}\sqrt{\dfrac{\phi}{k}}\,0.022\dfrac{(1 - S_w - S_{gr})^{0.01}}{S_w - S_{wc}}$ | $\sigma_{wg}\sqrt{\dfrac{\phi}{k}}\left(\dfrac{0.022}{S_w - 0.15}\right)^{0.2}$ | $2\gamma\sigma_{wg}\dfrac{\cos(\theta)}{r}\left(\dfrac{S_w - S_{wc}}{0.5 - S_{wc}}\right)^{-1/\omega}$ |
| **Gas trapping** | None | None | $\mathbf{v}_g = \mathbf{u}_g/(\phi S_g X_f)$ |

$S_{wn} = (S_w - S_{wc})/(1 - S_{wc} - S_{gr})$ and $S_{gn} = 1 - S_{wn}$.

Table 4.4 – Details on foam models analyzed via traveling wave by Lozano et al. (2021), Zavala et al. (2022), Fritis et al. (2022), and in this work. The columns represent the analytical works, while the rows correspond to foam flow modeling components described in Table 4.3.

| | **Lozano et al. (2021)** | **Zavala et al. (2022)** | **Fritis et al. (2022)** | **This work** |
|---|---|---|---|---|
| **Bubble Population Balance (Φ)** | Ashoori et al. (2011) | Zitha and Du (2010) [1] | Ashoori et al. (2011)<br>Zitha and Du (2010)[1] | Chen et al. (2010) [2] |
| **Mobility Reduction Factor** | Ashoori et al. (2011) | Ashoori et al. (2011) | Ashoori et al. (2011) | Hirasaki and Lawson (1985) |
| **Relative Permeabilities** | Ashoori et al. (2011) | Zitha and Du (2010) | Zitha and Du (2010) | Zitha and Du (2010) |
| **Capillary Pressure ($\mathbf{P_c}$)** | Ashoori et al. (2011) | Zitha and Du (2010) | Ashoori et al. (2011) | Zitha and Du (2010) |
| **Gas trapping** | None | None | None | None ($X_f = 1$) |
| **Experimental Data Reference** | Persoff et al. (1989) | Simjoo and Zitha (2015) | Simjoo and Zitha (2015) | Simjoo and Zitha (2015) |

[1] $K_d = 0$

[2] $k_{-1}^0 = 0$

## 4.3 DISCUSSIONS

In this work, we adjusted Model B so that its equations and parameters reproduce the same behavior as Model C, allowing direct use of the experimental data provided by Zitha and Du (2010). However, this approach limits the representational capacity of Model B, as its underlying physics is more comprehensive than that of Model C. Consequently, the adjusted Model B can be considered nearly equivalent to Model C.

Zavala et al. (2022) performed numerical experiments with Model C, imposing different values of water saturation $S_w^-$ at the left boundary. They observed that for $S_w^-$ in Region II (where no traveling wave exists), a spreading wave occurs from $S_w^-$ to an intermediate saturation within Region I (where the traveling wave exists), followed by a traveling wave to $S_w^+$. This behavior is similar to the findings of Lozano et al. (2022) for Model A. In contrast, in our numerical simulations, we did not fix the water saturation at the left boundary. Instead, to replicate the experimental conditions, we conducted a simulation fixing only the gas fractional flow $f_g$, which resulted in upstream water saturation in Region I (point $\mathcal{A}$ in Fig 4.4d). Therefore, we only present results for $S_w^-$ within Region I.

However, as we discussed in Section 4.2, the model was not able to capture the steady upstream saturation precisely. In the experiments, this saturation is about 0.35, while in the analytical and numerical results, it is approximately 0.45. Notably, 0.35 is in Region II. In the experiments, a spreading wave from 0.35 to around 0.45 is observed. After this wave, the saturation profile at all times maintains a nearly identical shape, displacing with a nearly constant velocity, resembling a traveling wave. In other words, although the model does not perfectly replicate the experiment, it still captures the observed traveling wave and is able to identify the $S_w^-$ values for which traveling waves appear or not in the experiment.

## 4.4 PARTIAL CONCLUSIONS

For the core flooding experimental data we investigated, all three models produce identical results, showing piston-like traveling profiles. We observed this both through mathematical classification and numerical simulation. The classification of traveling wave solutions in Model B is nearly identical to those reported in the literature for Models A (Lozano et al., 2021) and C (Zavala et al., 2022). Although none of the models accurately captured the upstream water saturation, all exhibited a traveling wave consistent with experimental observations.

To highlight the real differences between Models A, B. and C, we propose to study their behavior in heterogeneous media, which will be explored in the next chapter.

# 5 FOAM IN HETEROGENEOUS POROUS MEDIA

In previous chapters, we presented a semi-analytical solution for Model B and compared the analytical classifications of Models A, B, and C, showing that they yield identical results in a homogeneous one-dimensional domain with a fixed total velocity. The semi-analytical solution for Model B, derived in this work, exhibits a piston-like shape, similar to that reported for Models A and C in the literature (Lozano et al., 2021; Zavala et al., 2022; Fritis et al., 2022). The natural question arising from these studies is which foam flow regimes, described by these models, result in qualitatively different behaviors. In this chapter, we show that the analyzed models describe foam flow behavior in heterogeneous porous media differently, particularly in terms of spatial bubble distribution. This difference arises primarily from the foam balance model rather than the rheological models employed. The study presented in this chapter was published in Cedro et al. (2025).

## 5.1 METHODOLOGY

We perform numerical simulations in a two-dimensional domain to study the behavior of foam models presented in Section 2.4. For this purpose, we use an in-house simulator (de Paula et al., 2020, 2023), which is detailed in Appendix B.2. Briefly, its numerical methodology combines a hybrid finite element method to solve the elliptic Darcy's equation (2.19) and a high-order finite volume method to handle the hyperbolic transport equations (2.20)-(2.21). Although the simulator can handle compressible phases and gravitational effects, in this work, we neglected these phenomena to focus on foam generation in the media. Since these effects influence fluid displacement, bubble density observations could be biased by factors such as gravity override rather than permeability. Nevertheless, numerical investigations conducted by de Paula et al. (2020) show that, in the presence of strong foam, the saturation profiles were nearly identical in simulations with and without considering gravitational effects. This suggests that the findings presented here may extend to cases where gravity is taken into account.

In all numerical experiments, the reservoir is initially fully saturated with a surfactant solution, and no foam is injected to ensure that any foam present arises solely from the generation and coalescence mechanisms. The domain is rectangular, with injection occurring along the entire left boundary, no-flow conditions enforced at the top and bottom boundaries, and an out-flow condition applied at the right boundary. A fraction of gas ($\bar{f}_g = 90\%$) and surfactant solution is injected at a constant and uniform total velocity of $\bar{u} = 1.45 \cdot 10^{-5}\,\mathrm{m/s}$ along the border. This setup replicates the experiment conducted by Chen et al. (2010). Thus, we adopt their same model parameters, detailed in Table 5.1.

Table 5.1 – Parameters for foam flow simulation.

| Two-phase flow | | Foam model parameters | | | |
|---|---|---|---|---|---|
| $\phi$ | 0.18 | Model A | | Model B | |
| $\mu_g$ | $1.8 \cdot 10^{-5}\,\mathrm{Pa \cdot s}$ | $A$ | 400 | $\alpha$ | $7.4 \cdot 10^{-18}\ \mathrm{Pa \cdot s^{2/3} m^{10/3}}$ |
| $\mu_w$ | $1.0 \cdot 10^{-3}\,\mathrm{Pa \cdot s}$ | $C_{\mathrm{MRF}}$ | 239.88 or 511.68 | $k_1^0$ | $1.65 \cdot 10^{15}\ \mathrm{s^{1/3} m^{13/3}}$ |
| $\sigma_{wg}$ | $0.033\,\mathrm{N/m}$ | $K_c$ | $6.87 \cdot 10^{-3}\,\mathrm{s^{-1}}$ | $k_{-1}^0$ | $10\,\mathrm{m^{-1}}$ |
| $k_{rg}^0$ | 1.0 | $S_w^*$ | 0.1599 | $P_c^*$ | $3 \cdot 10^4\,\mathrm{Pa}$ |
| $k_{rw}^0$ | 0.7 | Model C | | $X_t$ | 0.78 |
| $n_g$ | 3 | $\alpha$ | $2.35 \cdot 10^{-16}\ \mathrm{Pa \cdot s^{2/3} m^{10/3}}$ | | |
| $n_w$ | 3 | | $5.01 \cdot 10^{-16}\ \mathrm{Pa \cdot s^{2/3} m^{10/3}}$ | | |
| $S_{wc}$ | 0.38 | $K_d$ | $0\,\mathrm{s^{-1}}$ | | |
| $n_{\max}$ | $10^{12}\,\mathrm{m^{-3}}$ | $K_g$ | $0.1\,\mathrm{s^{-1}}$ | | |
| $\bar{u}$ | $1.45 \cdot 10^{-5}\,\mathrm{m/s}$ | | | | |
| $\bar{f}_g$ | 90% | | | | |

### 5.1.1 Permeability fields

In this study, we utilize two distinct permeability fields for numerical experimentation. Field 1 is an artificially generated field characterized by significant heterogeneity similar to one used by Lovett et al. (2015) and by Pereira and Chapiro (2017). Field 2 is a realistic benchmark from the literature (SPE10), featuring pronounced high permeability regions.

Field 1 was generated from a two-point exponentially decaying covariance model, where a field $Z$ presents exponential spatial covariation expressed as

$$\mathrm{cov_Z}(r) = \sigma_Z^2 \exp\left(-\frac{r}{l}\right), \tag{5.1}$$

where $\sigma_Z$ is the standard deviation of $Z$ values, $r$ represents the distance between two field points, and the correlation length $l$ dictates the rate of covariance decay with distance. Using this methodology, Lovett et al. (2015) generated the standard normally distributed field $Z$ ($\sigma_Z = 1$), which we adopt in this work. We obtain the log-normal permeability field $k$ [$\mathrm{m^2}$], using

$$k(\mathbf{x}) = \exp\{-28.887 + 0.32459\, Z(\mathbf{x})\}, \tag{5.2}$$

where the exponent coefficients were chosen to obtain a permeability field with a standard deviation of $\sigma_k = 1.39 \cdot 10^{-13}\,\mathrm{m^2}$ and a mean value of $\bar{k}_1 = 3 \cdot 10^{-13}\,\mathrm{m^2}$. This mean value aligns with the measurement Chen et al. (2010) reported in their experimental investigations. We set the study domain with dimensions of $5.00\,\mathrm{m} \times 1.25\,\mathrm{m}$, and the grid shape is $200 \times 50$.

Field 2 is sourced from the 10th SPE Comparative Solution Project (SPE10) (Christie and Blunt, 2001). The SPE10 Project aims to compare multiscale approaches in

a complex geological model described as a regular Cartesian grid with $220 \times 60 \times 85$ cells. The upper 35 layers out of 85 consist of a shallow-marine Tarbert formation characterized by relatively smooth permeability. Field 2 corresponds to the first layer of the SPE10's permeability field, where the permeability mean value is $\bar{k}_2 = 4.3 \cdot 10^{-12}\,\mathrm{m}^2$, ranging from $8.1 \cdot 10^{-14}$ to $3.9 \cdot 10^{-11}\,\mathrm{m}^2$. The dimensions of the field were scaled to 3.67m $\times$ 1.00m, as the focus is solely on the structure of a realistic permeability field rather than addressing upscaling challenges. A similar idea was adopted by de Paula et al. (2020, 2023). The chosen dimensions enable the numerical simulator to achieve more accurate solutions for the specified grid. Table 5.2 summarizes the main quantitative characteristics of Fields 1 and 2. The next sections provide a graphical representation of Fields 1 and 2.

Table 5.2 – Permeability fields characteristics.

| | Field 1 | Field 2 |
|---|---|---|
| Dimensions | $5.00\,\mathrm{m} \times 1.25\,\mathrm{m}$ | $3.67\,\mathrm{m} \times 1.00\,\mathrm{m}$ |
| Grid size | $200 \times 50$ | $220 \times 60$ |
| Average value ($\bar{k}$) | $3.03 \cdot 10^{-13}\,\mathrm{m}^2$ | $4.33 \cdot 10^{-12}\,\mathrm{m}^2$ |
| Standard deviation ($\sigma_k$) | $1.39 \cdot 10^{-13}\,\mathrm{m}^2$ | $4.11 \cdot 10^{-12}\,\mathrm{m}^2$ |

### 5.1.2 Adjusting models

In order to compare the foam models, we aligned the parameters of Model A ($A$, $S_w^*$, $C_{\mathrm{MRF}}$, and $K_c$) and C ($K_g$ and $[\alpha]_{\mathrm{C}}$) with those of Model B. This task is challenging due to each model's distinct physics governing gas mobility and foam generation rates. To facilitate the comparison, we assume that the foam texture is in local equilibrium for each model individually. The local equilibrium foam texture for Model A ($[n_D^{\mathrm{LE}}]_{\mathrm{A}}$) and Model C($[n_D^{\mathrm{LE}}]_{\mathrm{C}}$) are expressed in Eqs. (2.27) and (2.30), respectively. We present $[n_D^{\mathrm{LE}}]_{\mathrm{B}}$ in the following paragraph. For parameters estimation, we utilize constant water saturation $S_w = 0.55$, based on the upstream result from the experiments of Chen et al. (2010). Phase velocities $\|\mathbf{u}_g\| = 1.30 \cdot 10^{-5}\,\mathrm{m/s}$, $\|\mathbf{u}_w\| = 1.45 \cdot 10^{-6}\,\mathrm{m/s}$ is given by the experiment injection condition.

*Local equilibrium foam texture of Model B* – $[n_D^{\mathrm{LE}}]_{\mathrm{B}}$

Let us first introduce the local equilibrium of Model B by considering that foam generation and destruction rates are equal, *i.e.*, $r_g = r_c$ in (2.29):

$$\left([n_D^{\mathrm{LE}}]_{\mathrm{B}}\right)^3 + \gamma\,[n_D^{\mathrm{LE}}]_{\mathrm{B}} - 1 = 0\,, \qquad \gamma = n_{\max}\frac{k_{-1}^0\|\mathbf{v}_g\|^{2/3}}{k_1^0\|\mathbf{v}_w\|}\left(\frac{P_c}{P_c^* - P_c}\right)^2 . \tag{5.3}$$

Notice that one can approximate $[n_D^{\mathrm{LE}}]_{\mathrm{B}}$ in Eq. (5.3) as $(1-\gamma)^{1/3}$ for $\gamma \ll 1$, and as $1/\gamma$ for $\gamma \gg 1$. Due to the non-negativity of $\gamma$, the depressed cubic equation (5.3) has only

one real root $[n_D^{\mathrm{LE}}]_{\mathrm{B}} \geq 0$, given by:

$$[n_D^{\mathrm{LE}}]_{\mathrm{B}} = \sqrt[3]{\Delta_+} + \sqrt[3]{\Delta_-}\,, \qquad \Delta_\pm = \frac{1}{2} \pm \sqrt{\frac{1}{4} + \frac{\gamma^3}{27}}\,. \tag{5.4}$$

Thus, it is possible to evaluate $[n_D^{\mathrm{LE}}]_{\mathrm{B}}$ for given phase velocities and capillary pressure. Equations (5.3)-(5.4) show that in this equilibrium model, there exists an algebraic expression that correlates permeability to foam texture through capillary pressure. We employ this expression to fit the parameters of Models A and C. In the numerical experiments we perform in this study, we simulate the full Model B presented earlier without assuming local equilibrium.

#### *5.1.2.1 Adjusting Model A*

*Limiting water saturation – $S_w^*$*

We determine the limiting water saturation $S_w^*$ such that $P_c(S_w^*) = P_c^*$, aligning with the concept of limiting capillary pressure in both models. Using the $P_c^* = 3 \cdot 10^4$ Pa (Chen et al., 2010) in Eq. (2.24) we obtain $S_w^* = 0.1599$. Note that this value is lower than connate water saturation $S_{wc} = 0.38$, and it will result in the maximum local equilibrium foam texture $[n_D^{\mathrm{LE}}]_{\mathrm{A}} = 1$, since $S_w > S_{wc} > S_w^*$. It is also worth mentioning that Model B explicitly includes the limiting capillary pressure $P_c^*$ in the foam destruction rate. For high values of $S_{wc}$, which is the case, it may be effectively impossible for water saturation to decrease sufficiently for $P_c$ to approach $P_c^*$ at some permeabilities. As a result, the destruction rate $r_c$ in Eq. (2.29) can become small enough that local equilibrium foam texture in Model B is achieved with $r_g \approx 0$, *i.e.*, $[n_D^{\mathrm{LE}}]_{\mathrm{B}} \approx 1$.

**Remark:** *In this work, we choose to compute the limiting water saturation $S_w^*$ as $P_c(S_w^*) = P_c^*$, as it is a justifiable and grounded way to adjust the parameter. We recognize that this fitting may result in values lower than the connate water saturation $S_{wc}$, as is indeed the case here with $S_w^* = 0.1599 < 0.38 = S_{wc}$. This can arise due to the specific combination of the $P_c$ function and the $P_c^*$ parameter. Ma et al. (2019) have criticized this scenario as non-physical. Kovscek and Radke (1994) state that $S_w^*$ may be either smaller or larger than $S_{wc}$, depending on the surfactant formulation and the characteristics of the porous medium. However, whether $S_w^*$ is smaller or greater than $S_{wc}$ did not impact our simulations, as changes in $S_w^*$ would affect Model A only when $S_w$ is relatively close to $S_w^*$ (as discussed in Section **2.4.1**). In our case, we are not handling dry foams, as $S_w$ remained consistently above 0.50 throughout all simulations, as we show later. Furthermore, we also conducted additional simulations with $S_w^*$ varying up to 0.50 and observed no significant change in the solution. We discuss this thoroughly in Appendix D.*

*Local-equilibrium sharpness parameter – $A$*

The function of local equilibrium foam texture $n_D^{\mathrm{LE}}$ defined in (2.27) was designed to resemble a step function at $S_w^*$, transitioning between no foam and maximum foam texture. The sharpness of this transition is governed by parameter $A$. One can see that as $S_w^*$ is significantly lower than $S_{wc}$, the expected value for $n_D^{\mathrm{LE}}$ is close to 1 for $A \gg 1$. That is why we maintained $A = 400$ defined by Ashoori et al. (2011).

*Constant of mobility reduction factor – $C_{\mathrm{MRF}}$*

Zavala et al. (2022) proposed a formula for estimating $C_{\mathrm{MRF}}$ from the non-Newtonian viscosity (2.28). Following this idea, we use (2.5), (2.23), (2.25), and (2.28) to equate the foamed gas mobilities of Models A $[\lambda_g]_{\mathrm{A}}$ and B $[\lambda_g]_{\mathrm{B}}$, recalling that $X_f = 1$ in Model A:

$$[\lambda_g]_{\mathrm{A}} = [\lambda_g]_{\mathrm{B}} \quad \Rightarrow \quad \frac{k_{rg}^0 \left(\frac{S_g}{1-S_{wc}}\right)^{n_g}}{\mu_g(1 + C_{\mathrm{MRF}}[n_D^{\mathrm{LE}}]_{\mathrm{A}})} = \frac{k_{rg}^0 \left(\frac{X_f S_g}{1-S_{wc}}\right)^{n_g}}{\mu_g + \alpha[n_D^{\mathrm{LE}}]_{\mathrm{B}} n_{\max} \|\mathbf{v}_g\|^{-1/3}}\,, \tag{5.5}$$

yielding:

$$C_{\mathrm{MRF}} = \frac{1}{[n_D^{\mathrm{LE}}]_{\mathrm{A}}} \left( \frac{1}{{X_f}^{n_g}} + \frac{\alpha[n_D^{\mathrm{LE}}]_{\mathrm{B}} n_{\max}}{{X_f}^{n_g} \mu_g \|\mathbf{v}_g\|^{1/3}} - 1 \right). \tag{5.6}$$

Since $[n_D^{\mathrm{LE}}]_{\mathrm{B}}$ depends on permeability due to capillarity (see Eqs. (5.3)-(5.4)), we evaluate $C_{\mathrm{MRF}}$ using the average permeability of Fields A ($C_{\mathrm{MRF}} = 239.88$) and B ($C_{\mathrm{MRF}} = 511.68$).

*Foam kinetic parameter – $K_c$*

In Model A, the kinetic parameter $K_c$ dictates the rate at which the foam texture $n_D$ tends to local equilibrium $n_D^{\mathrm{LE}}$, see Eqs. (2.21) and (2.26). To estimate $K_c$, we consider Eq. (2.21) at a fixed position (null gradient term) and constant gas saturation, resulting in the ODE:

$$\frac{\mathrm{d}n_D}{\mathrm{d}t} = \Phi\,, \quad n_D(0) = 0\,. \tag{5.7}$$

Solving the initial value problem (5.7) for Model A (2.26) we obtain:

$$n_D(t) = [n_D^{\mathrm{LE}}]_{\mathrm{A}} \cdot (1 - \exp\{-K_c t\})\,. \tag{5.8}$$

For Model B (2.29), we can approximate the ODE solution by:

$$\begin{cases} n_D(t) = [n_D^{\mathrm{LE}}]_{\mathrm{B}}\ (1 - \exp\{-\mathcal{K}_c\, t\})\,, \\ \mathcal{K}_c = \dfrac{3k_1^0}{n_{\max}} \|\mathbf{v}_w\|\, \|\mathbf{v}_g\|^{\frac{1}{3}} {[n_D^{\mathrm{LE}}]_{\mathrm{B}}}^2 + k_{-1}^0 \left(\dfrac{P_c}{P_c^* - P_c}\right)^2 \|\mathbf{v}_g\|\,. \end{cases} \tag{5.9}$$

Further details on obtaining Eq. (5.9) are provided in C. By comparing (5.8) and (5.9), we approximate $K_c \approx \mathcal{K}_c$, ensuring that both models achieve their local equilibria in approximately the same time. The derived $\mathcal{K}_c$ also varies with absolute permeability due

to $P_c$. In our case, the $\mathcal{K}_c$ values for the average permeability in both Fields 1 and 2 are similar. Therefore, we adopt $K_c = 6.87 \cdot 10^{-3}\,\mathrm{s}^{-1}$ for both fields.

Let us summarize Section *5.1.2.1*. We proposed a method to adjust the parameters of Model A (Ashoori et al., 2011) ($A$, $S_w^*$, $C_{\mathrm{MRF}}$, and $K_c$) based on the parameters of Model B (Chen et al., 2010). The primary objective was to align similar behaviors across both models, such as the limiting capillary pressure for $S_w^*$, gas mobility for $C_{\mathrm{MRF}}$, and the time required for foam to reach local equilibrium for $K_c$. However, this approach has some limitations. The first one is that we must select a constant value for $S_w$, which, in our case, was taken from the upstream experiments by Chen et al. (2010). Another limitation to this adjustment is that it may result in the behavior of the limiting water saturation $S_w^*$ being lower than the connate water saturation $S_{wc}$. Nonetheless, the accurate value of $S_w^*$ is not crucial for the phenomena investigated in this study. We focus on observing models that describe bubble density in heterogeneous media and, in the model by Ashoori et al. (2011), the foam texture reaches $[n_D^{\mathrm{LE}}]_{\mathrm{A}} \approx 1$ for all $S_w$ slightly greater than $S_w^*$.

### *5.1.2.2 Adjusting Model C*

*Rheological parameter – $\alpha$*

Models B and C share the foam apparent viscosity equation (2.28). However, Model B incorporates the flowing foam fraction $X_f$ into the superficial velocity $\mathbf{v}_g$, whereas Model C assumes no explicit trapped foam, such that $X_f[\mathbf{v}_g]_{\mathrm{B}} = [\mathbf{v}_g]_{\mathrm{C}}$. We establish an equivalence between the gas mobilities of both models, analogously to the approach taken in Section *5.1.2.1*:

$$[\lambda_g]_{\mathrm{B}} = [\lambda_g]_{\mathrm{C}} \quad \Rightarrow \quad \frac{k_{rg}^0 \left(\frac{X_f S_g}{1-S_{wc}}\right)^{n_g}}{\mu_g + n_{\max}\left[\alpha n_D^{\mathrm{LE}} \|\mathbf{v}_g\|^{-1/3}\right]_{\mathrm{B}}} = \frac{k_{rg}^0 \left(\frac{S_g}{1-S_{wc}}\right)^{n_g}}{\mu_g + n_{\max}\left[\alpha n_D^{\mathrm{LE}} \|\mathbf{v}_g\|^{-1/3}\right]_{\mathrm{C}}}\,, \tag{5.10}$$

yielding:

$$[\alpha]_{\mathrm{C}} = \frac{X_f^{1/3-n_g}}{[n_D^{\mathrm{LE}}]_{\mathrm{C}}} \left( \frac{\mu_g (1 - X_f^{n_g})}{n_{\max} \|[\mathbf{v}_g]_{\mathrm{B}}\|^{-1/3}} + [\alpha n_D^{\mathrm{LE}}]_{\mathrm{B}} \right). \tag{5.11}$$

Notice that, in the case where $X_f = 1$, the equation would yield $[\alpha n_D^{\mathrm{LE}}]_{\mathrm{B}} = [\alpha n_D^{\mathrm{LE}}]_{\mathrm{C}}$, meaning that Models B and C would exhibit equivalent phase mobilities for the same $n_D^{\mathrm{LE}}$.

Equation (5.11) defines $[\alpha]_{\mathrm{C}}$ as a function of interstitial gas velocity, which in turn depends on permeability (see Eq. (2.28)). To account for this dependence, we fitted $[\alpha]_{\mathrm{C}}$ separately for each field using its average permeability, resulting in $[\alpha]_{\mathrm{C}} = 2.35 \cdot 10^{-16}\ \mathrm{Pa} \cdot \mathrm{s}^{2/3}\mathrm{m}^{10/3}$ for Field 1 and $[\alpha]_{\mathrm{C}} = 5.01 \cdot 10^{-16}\ \mathrm{Pa} \cdot \mathrm{s}^{2/3}\mathrm{m}^{10/3}$ for Field 2. For Model C, the parameter $\alpha$ is approximately two orders of magnitude higher than for Model B. This difference arises because the inclusion of a trapped gas fraction $X_t = 1 - X_f = 0.78$ in Model B reduces gas mobility by about a hundred times, as seen in Eq. (2.23). The magnitude of $[\alpha]_{\mathrm{C}}$ aligns with parameter fittings from models that employ the same Hirasaki-

Lawson viscosity relation and do not account for gas trapping, such as those presented by Kam (2008); Zitha et al. (2006); Simjoo and Zitha (2015)

*Generation parameter – $K_g$*

We adjust the foam generation parameter $K_g$ using the same approach described in Section *5.1.2.1* for Model A's kinetic parameter, *i.e.*, comparing the characteristic time required for foam to reach its local equilibrium value in each model by solving the ODE (5.7). Substituting Model C's source term (2.30) into (5.7) gives:

$$n_D(t) = [n_D^{\mathrm{LE}}]_{\mathrm{C}} \cdot (1 - \exp\{-K_g t\}) \ . \tag{5.12}$$

By comparing (5.12) to (5.9), we can estimate the generation parameter as $K_g = \mathcal{K}_c$.

### 5.1.3 Foam models' rheology

In the literature, several authors characterize foam flow observed in experiments or described by models using a plot of the steady-state flow apparent viscosity ($\mu_{\mathrm{app}}$) as a function of gas fractional flow ($f_g$), often referred to as foam quality (Alvarez et al., 2001; Kam, 2008; Boeije and Rossen, 2015; Farajzadeh et al., 2015; Hematpur et al., 2018). Following this approach, we use Eqs. (2.27), (5.4), and (2.30) to evaluate the local equilibrium apparent viscosity $\mu_{\mathrm{app}}^{\mathrm{LE}} = 1/\lambda^{\mathrm{LE}}$ of Models A, B, and C, for a constant interstitial velocity $\bar{u} = 1.45 \cdot 10^{-5}\,\mathrm{m/s}$, across different permeabilities, and for parameters presented in Table 5.1. Figure 5.1 shows the behavior of $\mu_{\mathrm{app}}^{\mathrm{LE}}$ for Fields 1 and 2 in the left and right panels, respectively. As previously detailed, for each field, we fitted the parameters of Model A ($C_{\mathrm{MRF}}$ and $K_c$) and Model C ($[\alpha]_{\mathrm{C}}$ and $K_g$) using the average field permeability. Since local equilibria in models A and C are independent of permeability, each panel in Figure 5.1 displays a single curve for these models (dashed lines) representing $\mu_{\mathrm{app}}^{\mathrm{LE}}$ across the entire permeability range. In contrast, using the same set of parameters, Model B exhibits $\mu_{\mathrm{app}}^{\mathrm{LE}}$ increasing with permeability (solid curves with different colors), reflecting the behavior of foam apparent viscosity $\mu_f$ described in Section **2.4.2**. The increase in $\mu_{\mathrm{app}}^{\mathrm{LE}}$ diminishes with higher permeabilities. As illustrated in Figure 5.1, $\mu_{\mathrm{app}}^{\mathrm{LE}}$ is nearly identical for $k = 4.33 \cdot 10^{-12}\,\mathrm{m}^2$ and $k = 1.00 \cdot 10^{-11}\,\mathrm{m}^2$. Figure 5.1 also shows that both models exhibit a region where apparent viscosity increases with $f_g$ (indicating a low-quality regime) and another where it decreases with $f_g$ (indicating a high-quality regime), consistent with the behavior described in the literature above.

In addition to Figure 5.1, Figure 5.2 shows the maximum $\mu_{\mathrm{app}}^{\mathrm{LE}}$ attained for the models over $f_g \in [0, 1]$ for the same range of permeabilities as in Figure 5.1, as well as for a range of total interstitial velocity $u$. The figure shows that Model A's maximum $\mu_{\mathrm{app}}^{\mathrm{LE}}$ does not vary with permeability or total interstitial velocity once the parameters are fitted. In

Figure 5.1 – Local equilibrium apparent viscosity $\mu_{\text{app}}^{\text{LE}} = 1/\lambda^{\text{LE}}$ versus gas fractional flow $f_g$ at interstitial velocity $\bar{u} = 1.45 \cdot 10^{-5}\,\text{m/s}$, for different permeabilities $k$, with parameters given in Table 5.1. The left and right panels correspond, respectively, to Fields 1 and 2 (Section **5.1.1**) where Models A and C were fitted (Section **5.1.2**). The black circle represents the constant values of $f_g$ and $k$ assumed in the fitting (and consequently where all models coincide). Models A and C were fitted with permeability reference values $\bar{k}_1 = 3 \cdot 10^{-13}\,\text{m}^2$ and $\bar{k}_2 = 4.3 \cdot 10^{-12}\,\text{m}^2$ for Fields 1 and 2, respectively.

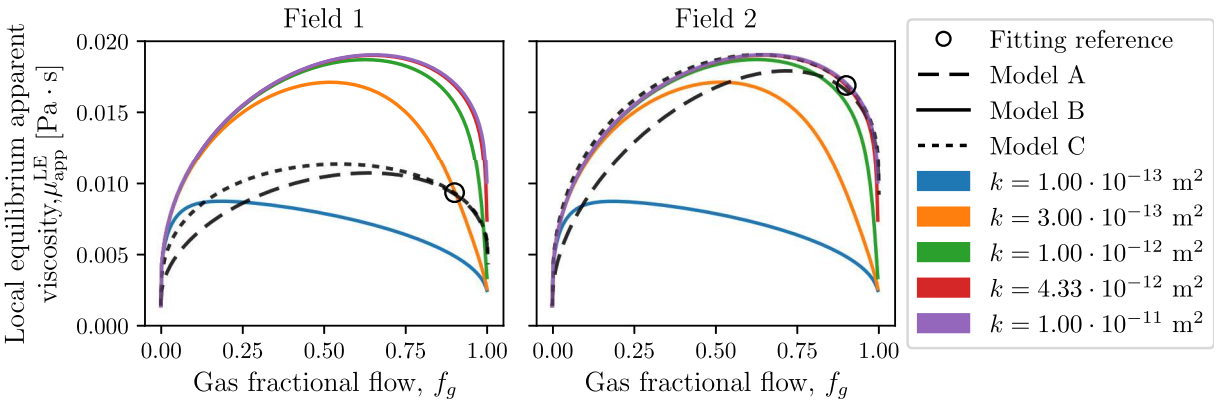


Source: Elaborated by the author (2025).

contrast, Figure 5.2 shows that for Model B, $\mu_{\text{app}}^{\text{LE}}$ increases with permeability and decreases with increasing velocity, exhibiting the shear thinning behavior incorporated in the model through Eq. (2.28). Additionally, propagation velocity's effect on apparent viscosity depends on permeability. For example, at $k = 1 \cdot 10^{-13}\,\text{m}^2$, velocity has minimal impact on $\mu_{\text{app}}$. However, as $k$ increases, the influence of velocity becomes more pronounced. It is worth also mentioning that within the velocity and permeability ranges shown in Figure 5.2, changes in both velocity and permeability lead to variations in $\mu_{\text{app}}^{\text{LE}}$ of similar magnitude, suggesting that both have comparable impacts on Model B's foam flow mobility. Finally, Fig. 5.2 shows that Model C allows $\mu_{\text{app}}$ to vary with velocity due to foam's shear-thinning behavior, as in Model B. However, unlike Model B, the local equilibrium foam texture (and consequently the apparent viscosity) does not depend on permeability.

Figure 5.3 presents a contour plot of the pressure gradient at steady-state foam flow ($\nabla p = \mu_{\text{app}}^{\text{LE}}(u_w + u_g)/k$) as a function of phase velocities $u_w$ and $u_g$, predicted by Models A, B, and C at $k = 3 \cdot 10^{-13}\,\text{m}^2$ (Field 1 average permeability). The difference between the contour lines for Models A, B, and C in Fig. 5.3 arises from discrepancies between the models. However, all models exhibit a low-quality regime (low $f_g$, where $\nabla p$ is nearly independent of $u_w$) and a high-quality regime (high $f_g$, where $\nabla p$ is nearly independent of $u_g$), although the high-quality regime is less pronounced for Models A and C. The fitting procedure adopted for Models A and C, described in Section **5.1.2**, is based on constant values $\bar{u}$ and $\bar{f}_g$ (Table 5.1). The black circle in the figure represents this fitting reference and, consequently, the point where all models coincide.

Figure 5.2 – Maximum local equilibrium apparent viscosity $\mu_{\text{app}}^{\text{LE}} = 1/\lambda^{\text{LE}}$, for different permeabilities $k$ and total interstitial velocities $u$. The left and right panels correspond, respectively, to Fields 1 and 2 (Section **5.1.1**). Parameters of Models A and C were fitted from Model B in Section *5.1.2.1*. Models A and C were fitted with permeability reference values $\bar{k}_1 = 3 \cdot 10^{-13}\,\text{m}^2$ and $\bar{k}_2 = 4.3 \cdot 10^{-12}\,\text{m}^2$ for Fields 1 and 2, respectively.

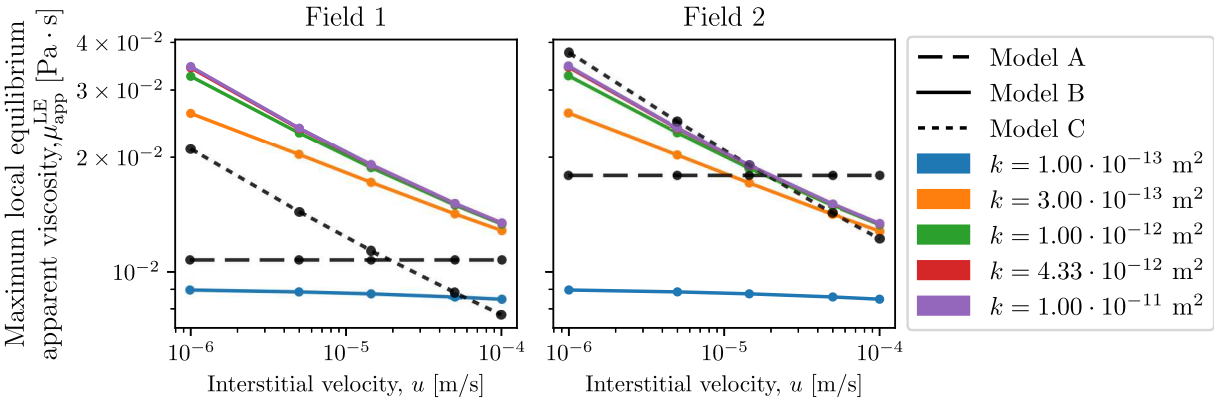


Source: Elaborated by the author (2025).

Figure 5.3 – Contour of pressure gradients (kPa/m) of steady-state foam flow predicted by Models A, B, and C for $k = 3 \cdot 10^{-13}\,\text{m}^2$ (Field 1 average permeability) with parameter values from Table 5.1. The black circle represents the constant values $\bar{u}$ and $\bar{f}_g$ assumed in the fitting of Models A and C from Model B (and consequently where all models coincide).

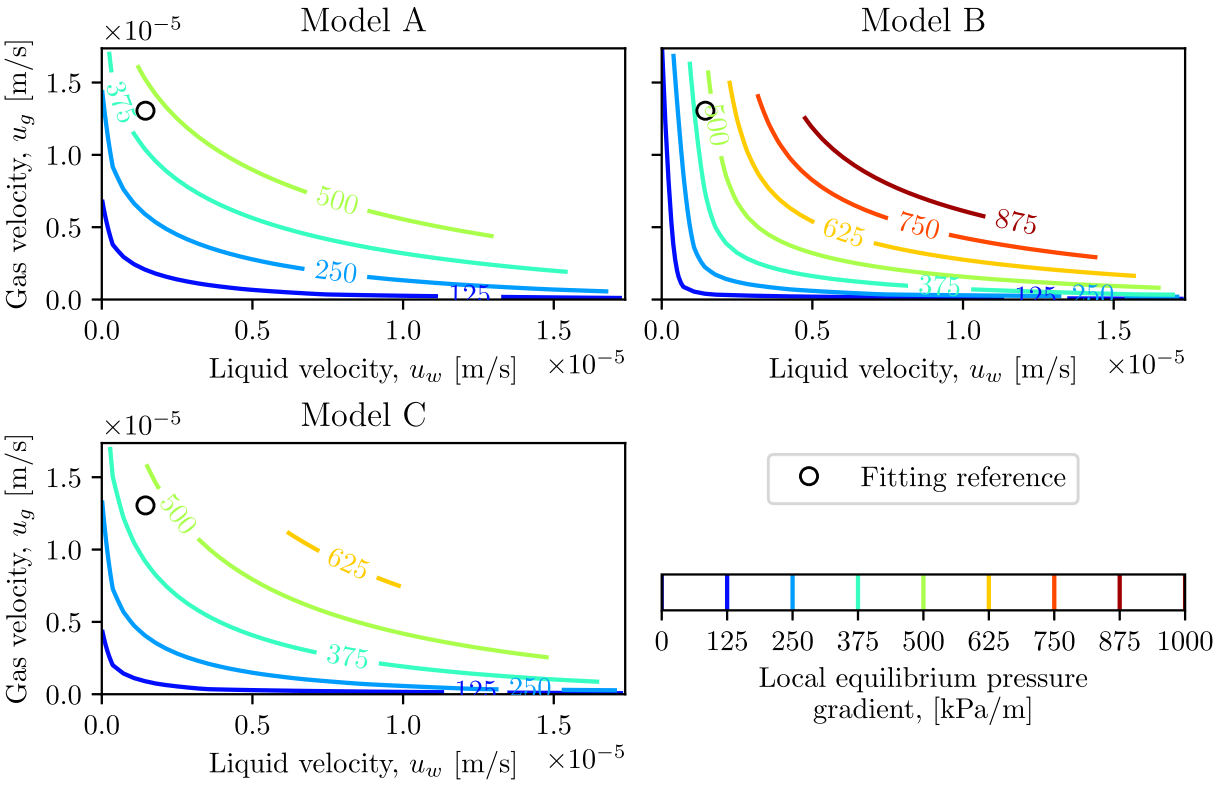


Source: Elaborated by the author (2025).

Figure 5.4 – Comparison of foam behavior for both models in Field 1 at 0.45 PV.

(a) Permeability Field 1.

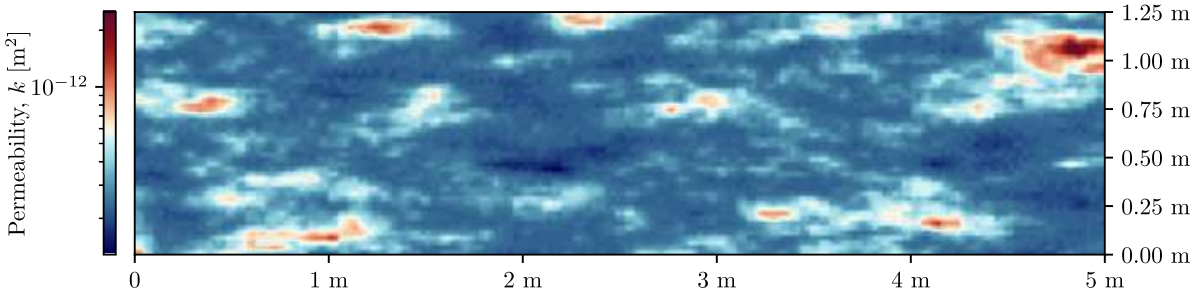


(b) Bubble density $S_g \cdot n_D$ predicted by Model A for Field 1.

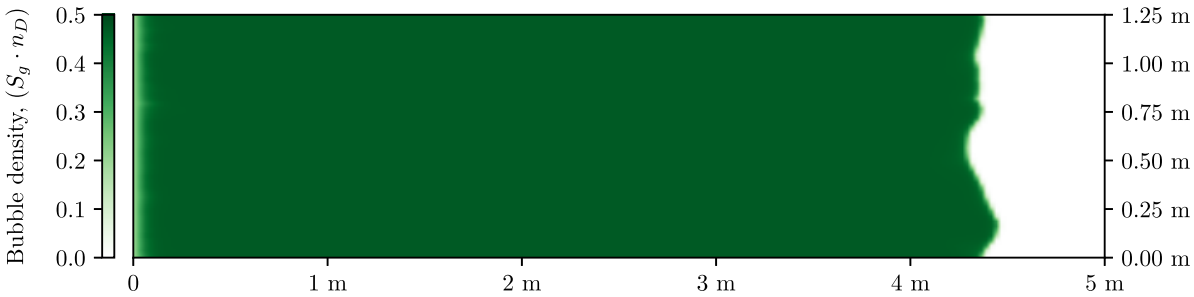


(c) Bubble density $S_g \cdot n_D$ predicted by Model B for Field 1.

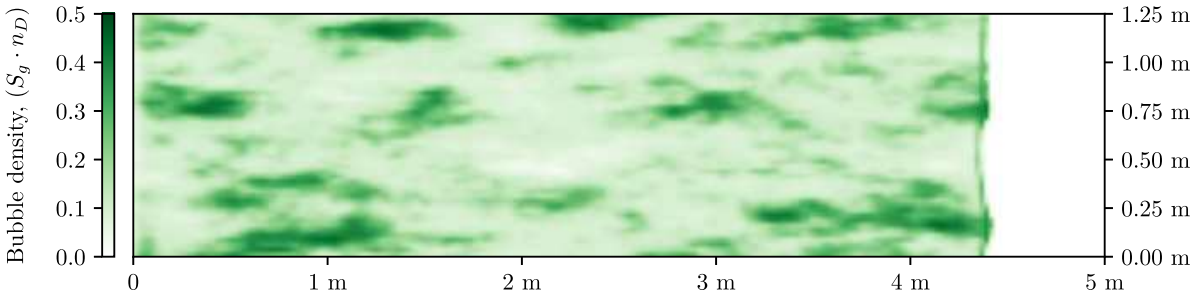


(d) Bubble density $S_g \cdot n_D$ predicted by Model C for Field 1.

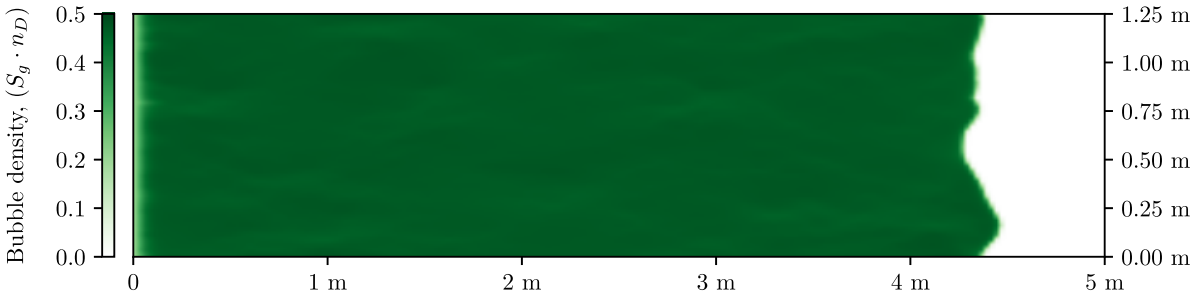


Source: Elaborated by the author (2025).

## 5.2 RESULTS

This section discusses the simulation results of foam models A, B, and C for permeability fields 1 and 2 presented above. Figures 5.4 and 5.5 illustrate both fields alongside the obtained bubble density ($S_g \cdot n_D$) for all models. Figure 5.4 shows the simulated bubble density for Models A (Fig. 5.4b), B (Fig. 5.4c), and C (Fig. 5.4d) in

Field 1 at 0.45 PV injected. Figure 5.4b shows that Model A exhibits a constant bubble density between the entrance region and the gas front. As the foam generation depends on the difference between water saturation $S_w$ and the limiting water saturation $S_w^*$, the foam texture tends to its maximum value since $S_w^*$ is much lower than the connate water, as pointed out in Sections **2.4.1** and *5.1.2.1*. The absolute permeability did not directly influence foam dynamics in this model.

In the simulation of Model B (Fig. 5.4c), it is evident that areas with more bubbles correspond to regions with higher permeability in Fig. 5.4a, suggesting a correlation between bubble density and permeability in this model. Furthermore, a high bubble density front is aligned with the injected gas front, indicating that foam is primarily generated at this location and subsequently tends to coalesce in regions with low permeability, as pointed out in Section **2.4.2**. This peak in foam front is also noticeable in the one-dimensional simulation of Model B we performed in Chapter 3 (see Fig. 3.5) and in the simulations reported by Chen et al. (2010). Appendix A shows this same peak in semi-analytical solutions of Model A, for different simplifications of the capillary pressure gradient (Lozano et al., 2022).

The simulation of Model C presents results similar to Model A, with an almost constant upstream bubble density, due to the fact that foam texture tends over time to the maximum value $n_D^{\mathrm{LE}} = 1$. However, a slight reduction in bubble density is noticeable in regions with higher permeability. This effect can be attributed to the shear-thinning behavior of foam. Under the same pressure gradient, fluids move faster in more permeable regions. For a shear-thinning foamed gas, this results in reduced mobility and an increased flowing gas fraction ($f_g$). At higher $f_g$, the steady gas saturation ($S_g$) is also higher (see Fig. 3.2). In all simulations of Model C, foam texture ($n_D$) remained nearly constant upstream of the gas front. Therefore, we attribute the slight decrease in bubble density ($S_g \cdot n_D$) with permeability to the shear-thinning behavior of the foam. Although Model B exhibits similar rheological behavior, its foam source term has a stronger influence on bubble density variation with permeability.

Figure 5.5 presents Field 2 and all models' simulated bubble density at 0.50 PV. This field exhibits a more even distribution of high and low permeability regions across the domain. It also features a large interconnected high permeability zone, with smaller low permeability zones inside. In this field, the simulation results of Model A (Fig. 5.5b) and C (Fig. 5.5d) are similar to the observed in Field 1, suggesting no significant correlation between bubble density and permeability in these models.

The simulation of Model B on Field 2 presented an elevated bubble density in the majority of the upstream domain, as depicted in Figure 5.5c. This phenomenon occurs because the field exhibits a high average permeability, resulting in lower capillary pressure. As a result, there is a more prominent bubble density throughout the domain. Comparing

Figure 5.5 – Comparison of foam behavior for both models in Field 2 at 0.50 PV.

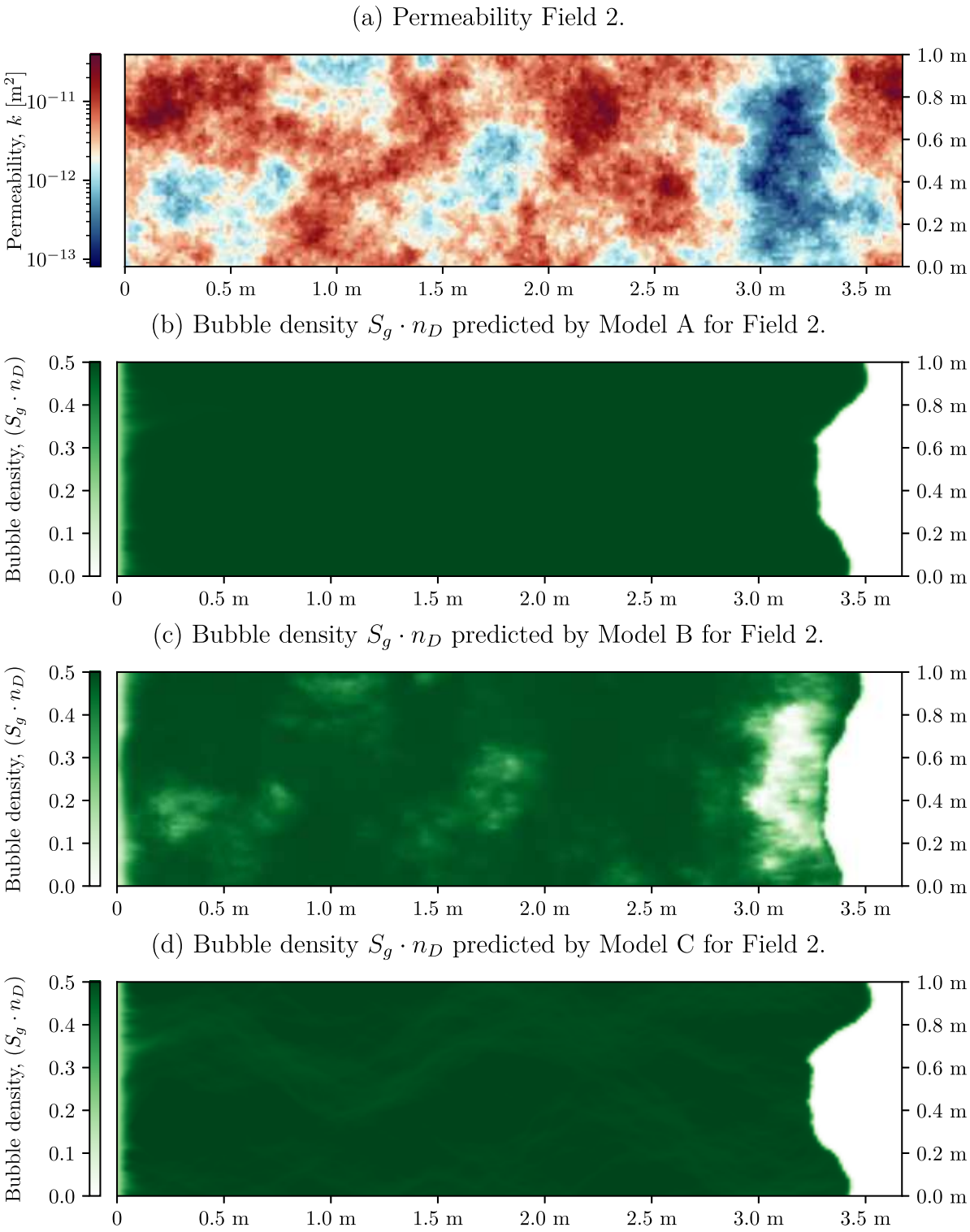


(a) Permeability Field 2.

(b) Bubble density $S_g \cdot n_D$ predicted by Model A for Field 2.

(c) Bubble density $S_g \cdot n_D$ predicted by Model B for Field 2.

(d) Bubble density $S_g \cdot n_D$ predicted by Model C for Field 2.

Source: Elaborated by the author (2025).

Table 5.3 – Mean and Standard Deviation of $n_D/n_D^{\mathrm{LE}}$ for Models A, B, and C in Fields 1 and 2 at 0.6 PV.

| Foam model | Mean ($n_D/n_D^{\mathrm{LE}}$) | | Standard deviation ($n_D/n_D^{\mathrm{LE}}$) | |
|---|---|---|---|---|
| | Field 1 | Field 2 | Field 1 | Field 2 |
| Model A | 1.0000 | 1.0000 | $8.5837 \cdot 10^{-5}$ | $2.9536 \cdot 10^{-4}$ |
| Model B | 0.9975 | 1.0083 | $6.5284 \cdot 10^{-2}$ | $1.0892 \cdot 10^{-1}$ |
| Model C | 1.0000 | 1.0000 | $1.2594 \cdot 10^{-4}$ | $6.0685 \cdot 10^{-4}$ |

Fig. 5.5c and 5.5a also reveals a clear correlation between bubble density and permeability. This correlation can be attributed to the model's representation of foam generation and destruction mechanisms, as discussed in Section **2.4.2**. Basically, low permeability slows propagation velocity, which diminishes foam generation. It also increases capillary pressure, bringing it closer to the threshold for foam instability. In contrast, high permeability enhances foam generation by increasing phase velocities and reducing foam destruction via lower capillary pressure. Model B captures this dependence of bubble density on permeability due to its foam source term, which accounts for phase velocities, capillary pressure, and absolute permeability.

### 5.2.1 Local equilibrium deviation

In all the experiments depicted in Figures 5.4 and 5.5, the foam texture remained practically unchanged upstream the gas front, *i.e.*, the foam was in local equilibrium. Figure 5.6 presents a scatter plot of the foam texture ($n_D$) obtained from simulations versus the local equilibrium foam texture ($n_D^{\mathrm{LE}}$) of Models A (Eq. (2.27)), B (Eq. (5.4)), and C (Eq. (2.30)). The figure shows that while Models A and C present $n_D$ and $n_D^{\mathrm{LE}}$ as nearly constant and close to 1, Model B exhibits a linear correlation between $n_D$ and $n_D^{\mathrm{LE}}$. The data presented in Figure 5.6 is summarized in Table 5.3 as mean and standard deviations of $n_D/n_D^{\mathrm{LE}}$ values. The table shows that all models' simulations presented foam texture close to the local equilibrium (*i.e.*, average close to one and a standard deviation close to zero). This suggests that Model B can be closely approximated by the local equilibrium model described in Section **5.1.2**, consistent with the findings of Chen et al. (2010). This approximation may explain the observed correlation between bubble density and permeability in Model B, as the local equilibrium model presents a dependence of $n_D^{\mathrm{LE}}$ on permeability.

### 5.2.2 Correlation between bubble density and permeability

Figure 5.7 displays scatter plots illustrating the relationship between bubble density and permeability for all cases. In simulations, we observed a consistent entrance region within the domain where foam still forms, leading to a bubble density that does not depend

Figure 5.6 – Scatter plot depicting the correlation between simulated foam texture $n_D$ and local equilibrium foam texture $n_D^{\mathrm{LE}}$ for Models A, B, and C. Each dot corresponds to a mesh point, with $n_D$ obtained from simulations at 0.6 PV and $n_D^{\mathrm{LE}}$ determined by applying Eqs. (5.3)-(5.4) to the simulated data.

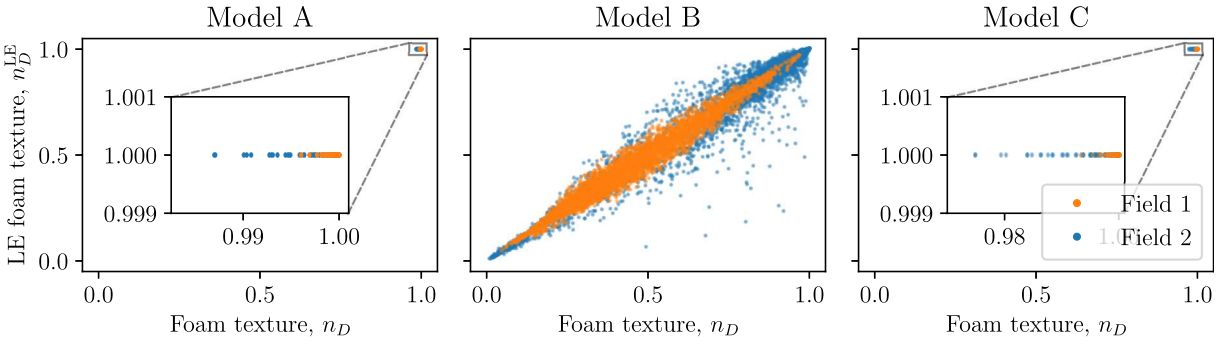


Source: Elaborated by the author (2025).

Figure 5.7 – Scatter plots depicting the relationship between dimensionless bubble density $S_g \cdot n_D$ and permeability $k$ for every mesh point at 0.6 PV.

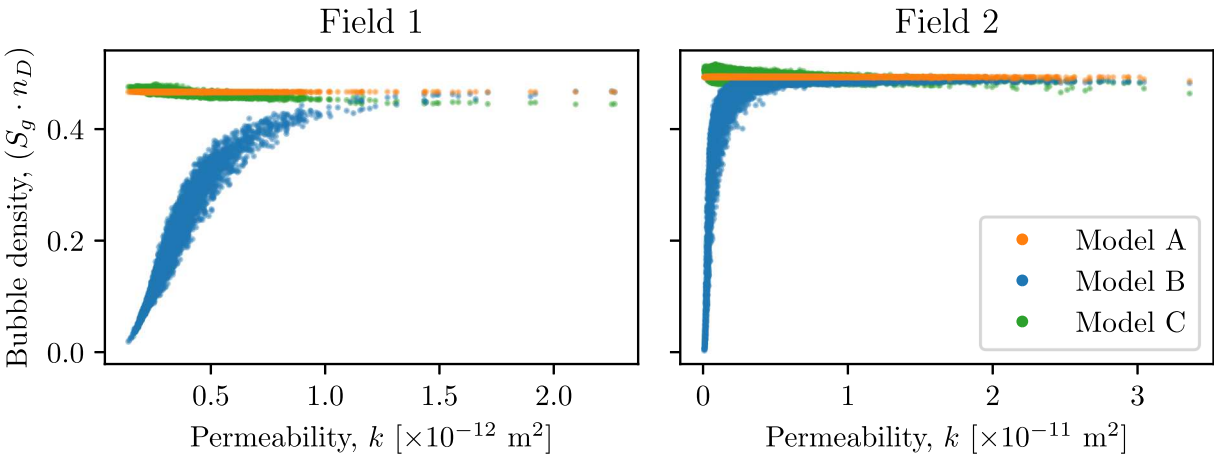


Source: Elaborated by the author (2025).

solely on field properties. The entrance region extends approximately 0.1 m, as shown in Figures 5.4 and 5.5. Hence, for the correlation analysis, we excluded the initial 0.2, m length to better clarify the correlation in the remaining domain.

Figure 5.7 shows that bubble density increases noticeably with permeability in Model B, while in Model C, it exhibits a slight decrease. In contrast, Model A shows no variation in bubble density with permeability. We also observed that bubble density in Model B tends to plateau for permeabilities higher than $10^{-11}$ m$^2$, suggesting that correlation diminishes for higher permeabilities.

Although the existence of a correlation between bubble density and permeability is evident in Figures 5.4, 5.5, and 5.7, we decided to quantify it for a more accurate and systematic analysis. To do this, we employ Spearman's coefficient of rank correlation –

see Kendall (1943). This coefficient is well-suited for detecting monotonic associations, providing a measure that does not depend on linearity assumptions. It ranges from $-1$ to 1, where a value of 1 indicates a perfect positive monotonic correlation, $-1$ indicates a perfect negative monotonic correlation, and 0 indicates no monotonic correlation. The $p$-value associated with Spearman's coefficient indicates the probability of obtaining that coefficient for a selected sample when there is no correlation in the population. A low $p$-value (typically less than 0.05) suggests that the observed correlation is statistically significant, implying that a monotonic relationship between variables likely exists. We computed Spearman's coefficient to assess the correlation between permeability $k$ and bubble density $S_g \cdot n_D$ for all simulations. These values are summarized in Table 5.4. The data used for this analysis were obtained from simulations at 0.6 PV, which corresponds to shortly after the breakthrough occurred in all cases.

Table 5.4 – Spearman's correlation coefficient between permeability $k$ and bubble density $S_g \cdot n_D$ for simulations at 0.6 PV, using the parameters provided in Table 5.1.

| Foam model | Spearman's coefficient | | $p$-value | |
|---|---|---|---|---|
| | Field 1 | Field 2 | Field 1 | Field 2 |
| Model A | $-0.18863$ | $-0.22846$ | $< 10^{-15}$ | $< 10^{-15}$ |
| Model B | 0.98737 | 0.92538 | $< 10^{-15}$ | $< 10^{-15}$ |
| Model C | $-0.73587$ | $-0.59442$ | $< 10^{-15}$ | $< 10^{-15}$ |

For Model A, in both fields, the absolute value of the coefficient is less than 0.25, suggesting almost no correlation. For Model B, the coefficient exceeds 0.9 in both permeability fields, indicating a strong positive monotonic relationship that supports the consistent association between permeability and bubble density seen in Figure 5.7. For Model C, there is a significant negative correlation (with the smallest coefficient around $-0.6$). However, as shown in Figure 5.6 and Table 5.3, the variation in bubble density is quite small, indicating that, despite the correlation, the overall impact on foam behavior is less significant compared to Model B. Particularly, in Models A and C, $n_D^{\mathrm{LE}}$ is generally close to unity, leading $n_D$ to be near unity. Consequently, the variations in bubble density, $S_g \cdot n_D$, observed in Table 5.4, primarily reflect variations in gas saturation, $S_g$. In Model C, these variations are likely driven by its shear-thinning foam behavior.

In all cases, the associated $p$-value was less than the machine precision, indicating a high level of statistical significance.

### 5.2.3 Water production

In Figure 5.8, we present the cumulative water production for simulations of all models for both permeability Fields 1 and 2. In all these cases, the breakthrough

Figure 5.8 – Cumulative water production for Models A, B, and C for both permeability fields.

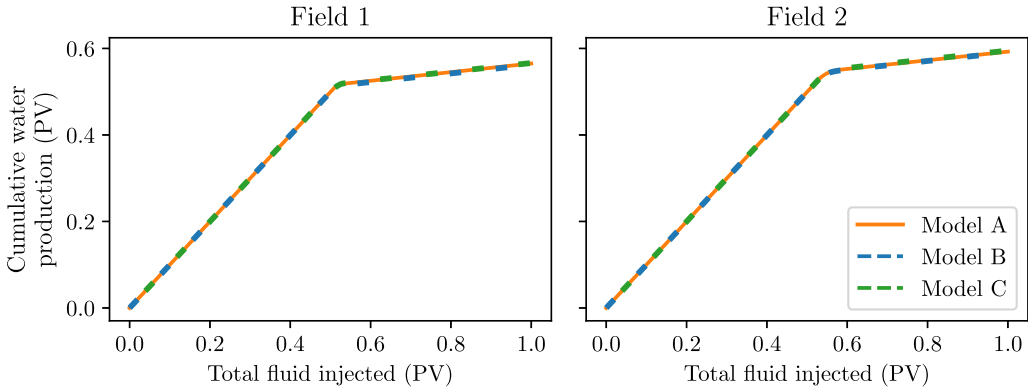


Source: Elaborated by the author (2025).

occurs approximately at the total injection of 0.5 PV. In simulations conducted in both Fields 1 and 2, all models exhibit similar production, with Model C showing slightly higher production and Model B slightly lower. In our examples, the maximum relative difference between the models' production curves until 1.0 PV is lower than 0.71%. Therefore, we believe that the difference in productions, in this case, is more due to the fitting technique than to the physical properties of each model.

This close resemblance of production curves suggests a good fit between the models. However, it's important to note that these curves do not capture the diverging behaviors of the models with respect to permeability heterogeneity. Therefore, Models A and C are capable of capturing this result of interest, similar to Model B, by appropriately adjusting their parameters to reflect the physical characteristics of the models.

### 5.2.4 Pressure profiles

In this section, we show pressure profiles and pressure drops for all simulations. This pressure data provides a meaningful connection between theoretical studies and experimental data, as pressure drops are directly measurable in laboratory experiments. Figures 5.9 and 5.10 display the pressure distributions for Fields 1 and 2, respectively. The pressure profiles were obtained by averaging the pressure at each point $x$ along the core length. The pressure drop corresponds to the average inlet pressure, given that the outlet pressure is set to zero. The figures show that the variations in bubble density profiles (shown in Figs. 5.4 and 5.5) are also evident in the pressure profiles, with Models A and C producing similar results, while Model B exhibits a significant deviation. The most pronounced difference occurs in Field 2 (Fig. 5.10), which contains a large low-permeability region near $x = 3\,\text{m}$. In this region, Model B predicts fewer bubbles, leading to reduced gas mobility and a lower pressure gradient compared to Models A and C. Consequently,

Figure 5.9 – Pressure profiles and pressure drop for Models A, B, and C in Field 1 corresponding to simulations in Figure 5.4.

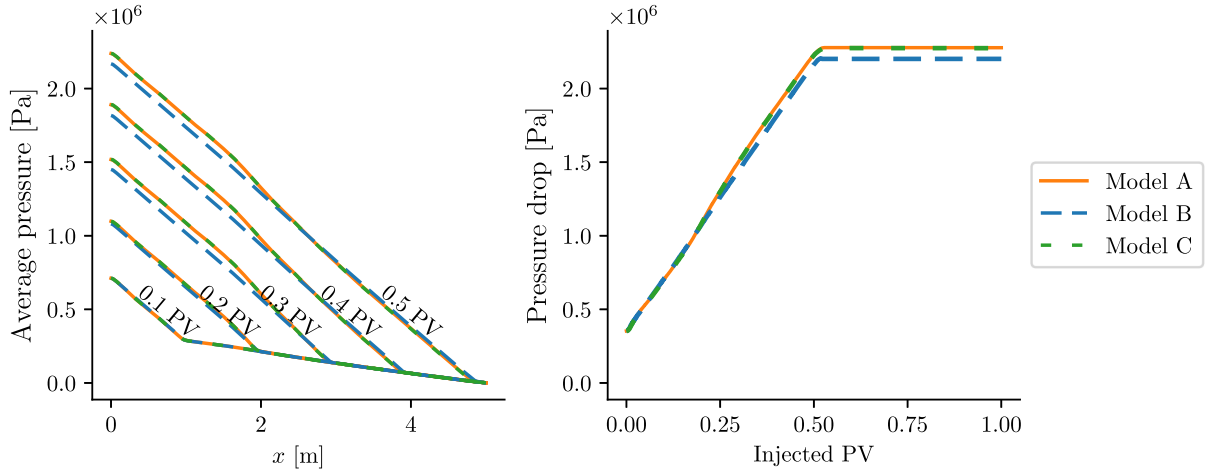


Source: Elaborated by the author (2025).

Figure 5.10 – Pressure profiles and pressure drop for Models A, B, and C in Field 2 corresponding to simulations in Figure 5.5.

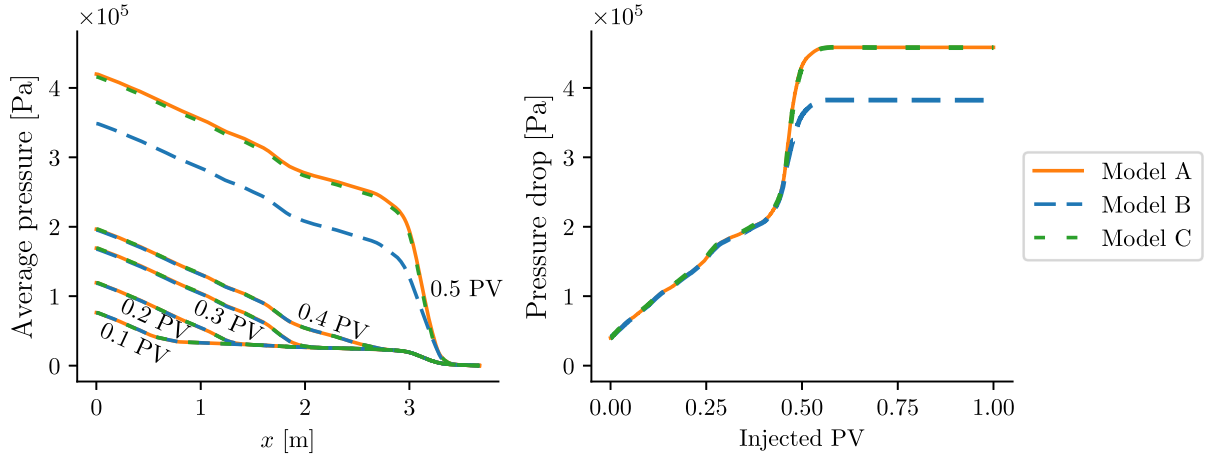


Source: Elaborated by the author (2025).

the pressure profile of Model B diverges from those of Models A and C when the gas front reaches this region, shortly after 0.4 PV injected.

## 5.3 DISCUSSIONS

The key differences between the three foam models used in this work are foam rheology and foam generation/coalescence. Model A treats foam as a Newtonian fluid, adjusting gas mobility using a linear relationship defined by Eq (2.25). In contrast, Models B and C describes foam as non-Newtonian through Eq. (2.28). As a consequence,

in more permeable regions where flow velocity is higher, the foam exhibits lower viscosity, leading to a greater fraction of flowing gas and higher gas saturation. Thus, our observations indicate that shear-thinning behavior leads to increased gas saturation in highly permeable regions. When it comes to foam generation and coalescence, Model A and C employ linear functions of foam texture (Eqs. (2.26) and (2.30), respectively), whereas Model B uses a more realistic nonlinear expression (Eq. (2.29)). The primary distinction between these models in representing bubbles in heterogeneous porous media lies in the dependency of the source term on permeability. In this context, Eqs. (5.3)-(5.4) demonstrate that Model B, in local equilibrium, correlates foam texture ($n_D^{\mathrm{LE}}$) with permeability ($k$), regardless of the $\mu_f$ formulation. We can conclude that Model B's source term significantly affects the description of bubble distribution in heterogeneous porous media. To illustrate this, consider a scenario where, initially, there is no foam in the reservoir. In heterogeneous media, higher permeabilities lead to higher phase velocities. According to Eq. (2.29), higher phase velocities and fewer bubbles result in foam generation ($r_g$). Equation (2.28) indicates that the apparent foam viscosity $\mu_f$ increases with foam texture ($n_D$), which reduces gas mobility and, consequently, gas velocity ($v_g$). As shown in Eq. (2.29), a decrease in gas velocity reduces bubble coalescence ($r_c$). This means that once foam is generated, it becomes difficult to destroy it through gas velocity ($v_g$), as $v_g$ is lower in the presence of foam. Another factor in bubble destruction is capillary pressure ($P_c$), but $P_c$ is low in high-permeability regions (see Eq. (2.24)). As a result, bubbles tend to be generated more frequently in high-permeability zones, and once foam is present, it is difficult to destroy it either through phase velocities or capillary pressure effects. This behavior leads to foam formation in high-permeability areas, which can be interpreted as trapped foam.

Several authors have reported that the limiting saturation $S_w^*$ varies with permeability, including Khatib et al. (1988); Farajzadeh et al. (2015); Kapetas et al. (2017); Gassara et al. (2020); Zeng et al. (2020), among others. Modifying Model A to allow the foam source term (specifically $S_w^*$) to vary spatially with permeability may significantly enhance its ability to represent bubble density in heterogeneous porous media, even without incorporating the complex terms used in Model B. In Model C, the generation and coalescence coefficients ($K_g$ and $K_d$) could be modified to change with permeability. Zitha and Du (2010) mention that, under certain circumstances, these coefficients are likely to depend on variables such as phase velocities. These modifications could lead to more accurate predictions of foam dynamics across diverse geological formations, improving the model's applicability to real-world scenarios where heterogeneity plays a crucial role in fluid flow dynamics.

The comparison we present in this work highlights the differences between the models and may guide the selection of a model for specific applications. Model B provides a stronger dependence of foam dynamics on phase velocities and permeability, making it suitable for highly heterogeneous reservoirs. In contrast, Models A and C, with no

direct dependence of foam on permeability and fewer parameters, are more practical for situations with nearly homogeneous media or limited data, such as early-field assessments. Factors to consider when employing one of these models include reservoir complexity, data availability, and computational resources. Despite the differences between the models, the results presented in Section 5.2 show that the simpler Models A and C, with the fitting described in Section **5.1.2**, were able to represent key application metrics, such as gas front location and water production, in heterogeneous media, as effectively as Model B.

We performed simulations in two permeability fields, with Field 2 having a greater variation in permeability than Field 1. In all simulations, the gas sweep front was relatively regular. However, the shape of the front may be significantly different when studying media with longitudinal strips with different orders of permeability, as shown in the work by de Paula et al. (2023). In that study, Model B was simulated in a field featuring a high-permeability longitudinal strip (SPE10, Layer 36), showing a non-uniform channeled foam front. In this case, the pressure profiles presented in Figs. 5.9 and 5.10 may show more significant differences between the models. Additionally, it is worth noting that the permeability distribution in Field 2 originally spans hundreds of meters in length (Christie and Blunt, 2001). In this work, this field was rescaled to a length of 3.67 m to simplify the numerical simulations for the given grid, focusing on the structure of a realistic permeability field rather than addressing upscaling challenges. Consequently, permeability variations that occur over meters in the original field occur over centimeters in the scaled Field 2, leading to a tighter range for flow to reach a steady state in each permeability region. Thus, the deviations from local equilibrium shown in Figure 5.6 and Table 5.3 may be less pronounced in the original field.

In our simulations, despite the complexity of the foam dynamics in Model B, this model exhibited the fastest simulation times among the models studied. We attribute this performance to our numerical approach rather than to any numerical advantage of Model B. Specifically, our nonlinear time-step solver (Newton-Raphson method – see Appendix B.2) tends to be less efficient when handling sharper profiles, which are more commonly observed in the simulations of Models A and C. Therefore, Model B's faster simulation times are primarily related to the type of solutions these models produce rather than the complexity of their equations. Further investigations into the numerical efficiency of these methods would be valuable for future studies.

## 5.4 PARTIAL CONCLUSIONS

One of the features of foam flow in porous media is elevated foam formation in highly permeable regions and fractures. We show how different models deal with this property. In particular, the model describing foam generation and coalescence through

complex functions depending on the phase velocities and capillary pressure can capture this phenomenon (Model B). On the other hand, simpler models (Models A and C) did not produce qualitatively similar results. We believe other models with such simple foam generation and coalescence functions will not describe this phenomenon either. Therefore, when applied to heterogeneous cases, these functions must account for variations in permeability. In Model A, this adjustment should likely be in the limiting water saturation, while in Model C, it might be incorporated into the foam destruction coefficient.

Although the investigated models produce qualitatively the same solutions for homogeneous media, suggesting no benefit from adopting more complex models in such cases, the example provided in this work highlights differences between these models in heterogeneous media. We stress that the more complex model produces results that align with laboratory experiments for heterogeneous porous media, providing higher foam texture in highly permeable regions inside the medium.

To compare Models A, B, and C, we proposed a workflow for fitting the model parameters based on the foam equilibrium estimated for each model separately. As a result, the models presented a good agreement between the gas front location, breakthrough time, and production rates.

Model B presented a strong correlation between bubble density and permeability, visually resembling trapped foam. This correlation is due to the intricate foam generation and destruction mechanisms depending on phase velocities, capillary pressure, and, consequently, absolute permeability. In our simulations, foam reached the local equilibrium between the entrance region and the gas front. Consequently, the observed positive correlation between permeability and bubble density aligns with the local equilibrium foam model. In contrast, Model A maintained nearly constant bubble density regardless of permeability heterogeneity, indicating no strong correlation between bubble density and permeability. Model C exhibited a slight reduction in bubble density in more permeable regions, likely due to its shear-thinning foam rheology, an opposite effect to that observed in Model B. The pressure drop profiles capture the differences between models, which become more pronounced in highly heterogeneous media. However, despite this discrepancy, these models accurately predicted production rates comparable to Model B. Simulations of both models rapidly achieved local equilibrium, supporting the applicability of local equilibrium models in these cases.

# 6 CONCLUSIONS

We developed a semi-analytical solution for a non-Newtonian foam flow model validated through numerical simulations. By comparing it to the other two simpler foam models, we showed that they all produce identical numerical and analytical results in one-dimensional homogeneous media when fitted to typical experimental conditions (high-quality strong foam). This suggests that in such cases, the choice of model has little impact on the overall foam displacement behavior.

In contrast, our numerical simulations in heterogeneous media revealed key differences. The model incorporating a permeability-dependent foam destruction rate exhibited higher bubble density in more permeable regions, aligning with experimental observations reported in the literature. This suggests that such models may better capture foam distribution in complex porous structures. Therefore, the simpler models, when applied to heterogeneous cases, must consider foam generation and destruction varying permeability. However, all models accurately predicted breakthrough time, production curves, and the shape of the foamed gas front, reinforcing their reliability for practical applications.

Overall, our findings validate the use of the traveling wave in obtaining solutions for both Newtonian and non-Newtonian foam models. Additionally, they provide a framework for selecting appropriate models based on the desired level of detail in describing bubble distribution in different geological formations. Furthermore, this study offers insights into foam strength in heterogeneous media, potentially aiding in the calibration of parameters in more realistic reservoir simulators.

## 6.1 FURTHER INVESTIGATIONS

Building on the methods and observations presented in this study, we outline some directions that could be explored in future extensions:

- Investigate traveling wave foam flow with variable surfactant concentration. This approach may be feasible when surfactant transport behaves as piston-like displacement (e.g., Cedro et al. (2019), Chapiro and Lozano (2022), Zavala et al. (2024)). Introducing additional equations for surfactant transport and/or adsorption would increase the dimensionality of the traveling wave ODE system, requiring seeking solutions in spaces of three or more dimensions, which is mathematically complex. To reduce complexity, equilibrium models for foam texture and/or adsorption could be considered.

- Explore the existence of traveling wave solutions for a non-Newtonian foam model for radial flow, which better represents the injection conditions in applications.

In this case, flow velocity naturally decreases with distance from the injection point. A possible approach could involve identifying a geometric symmetry that allows reformulating the governing equations to apply a conventional traveling wave framework. A similar approach was adopted by Sumnu-Dindoruk and Dindoruk (2006) for conservation laws.

- Study the ability of simple models, such as Models A and C, to represent bubble distribution in heterogeneous media when the foam source term is sensitive to permeability variations.
- Investigate the impact of bubble distribution in more realistic simulations incorporating, for instance, gravity effects, compressibility, or channelized permeability fields.
- Given the varying complexity of foam apparent viscosity and foam generation equations across models, it is worth further investigating their numerical efficiency. Our preliminary observations suggest that computational effort may be more sensitive to the sharpness of saturation and foam texture profiles than to the complexity of rheology and balance equations.

## 6.2 CONTRIBUTIONS

**Articles in scientific journals:**

- Lozano, L. F., Cedro, J. B., Zavala, R. V. Q., and Chapiro, G. (2022). How simplifying capillary effects can affect the traveling wave solution profiles of the foam flow in porous media. *International Journal of Non-Linear Mechanics*, 139:103867
- Vásquez, A. J. C., Lozano, L. F., Pereira, W. S., Cedro, J. B., and Chapiro, G. (2022). The traveling wavefront for foam flow in two-layer porous media. *Computational Geosciences*, 26(6):1549–1561
- Cedro, J. B. and Chapiro, G. (2024). Traveling wave solutions for a realistic non-newtonian foam flow model. *Geoenergy Science and Engineering*, 232:212478
- Cedro, J. B., de Paula, F. F., and Chapiro, G. (2025). On the modeling of the foam dynamics in heterogeneous porous media. *Advances in Water Resources*, 196:104882

**International conference proceedings:**

- Cedro, J. B. and Chapiro, G. (2022). Numerical observation of traveling wave solution in a non-newtonian foam model. In *XLIII Ibero-Latin-American Congress on Computational Methods in Engineering (CILAMCE)*, Foz do Iguaçu, Brazil

**Presentations in conferences:**

- *XLIII Ibero-Latin American Congress on Computational Methods in Engineering (CILAMCE)*, Foz do Iguaçu, Brazil, November 2022. Presented work: "Numerical observation of traveling wave solution in a non-Newtonian foam model".
- *SIAM Conference on Mathematical & Computational Issues in the Geosciences*, Bergen, Norway, June 2023. Presented work: "Foam traveling wave in porous media".
- *6th Brazil InterPore Chapter Conference on Porous Media*, Campinas, Brazil, August 2023. Presented work: "Foam traveling wave in porous media".

# APPENDIX A – TRAVELING WAVE STUDY ON SIMPLIFYING CAPILLARY EFFECTS IN MODEL A

In this appendix, we briefly present the findings we published in the article by Lozano et al. (2022). In this paper, we mathematically investigate the consequences of neglecting and simplifying capillary forces in the context of traveling wave solutions applied to foam displacement in porous media. We analyze three physically admissible possibilities for simplifying this term in the first-order kinetic model (Model A, presented in Section A.2). Two of these simplifications yield qualitatively inaccurate solutions regarding foam texture, while the third yields acceptable results. However, the extent of this divergence can't be measured through laboratory experiments. The results presented here are further discussed by Lozano et al. (2022), which also addresses the existence and classification of the analytical solutions presented in this chapter.

## A.1 SIMPLIFYING THE CAPILLARY DIFFUSION

In mechanistic models, foam displacement in porous media is often treated as a tracer in the gas phase (Kovscek et al., 1995; Kam, 2008; Zitha and Du, 2010; Ashoori et al., 2011). Although it is common knowledge that foam affects gas mobility, the effect of capillary forces on the foam flow is not evident and has not been widely addressed in the literature. Figure A.1 depicts the foam geometry in a capillary tube, illustrating the presence of a liquid film between the bubbles and the pore wall. Notice that the yielding of capillary force due to the contact angle is not as evident as in the case shown in Figure 2.2. This issue is also challenging in experimental studies as modern CT scans can determine water/gas saturation profiles inside porous media but not the foam texture (Simjoo and Zitha, 2015; Janssen et al., 2020). The focus in this chapter is to investigate the influence of capillary pressure on saturation and foam texture profiles by employing various simplifications in the context of mathematical analysis of traveling wave solutions.

The literature widely presents two common approaches to simplify the term involving capillary pressure. The first approach assumes that the partial pressures of the water and gas phases are equal, equivalent to neglecting the capillary pressure term $\mathrm{d}P_c/\mathrm{d}S_w = 0$. The second approach considers $f_w\lambda_g \mathrm{d}P_c/\mathrm{d}S_w$ as a constant. Further details can be found in Section **A.2.2** and (Bedrikovetsky, 1993). This approach is commonly used in conservation

Figure A.1 – Schematic representation of the gas-water flow in a pore throat. The left panel presents a typical situation without foam (Chen et al., 2006), where the arrow indicates the direction of resulting capillary forces acting at the interface. The right panel shows what happens in the presence of foam (Hematpur et al., 2018), where thin water film can form between bubbles and the pore wall.

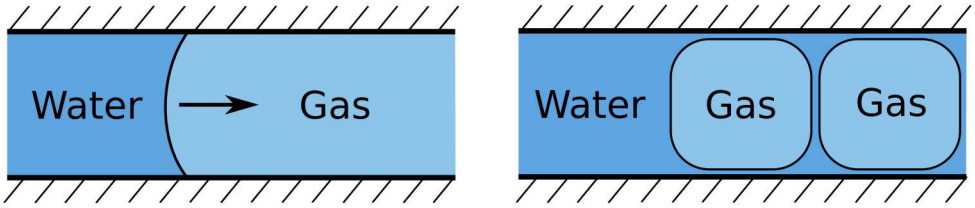


Source: Elaborated by the author (2022).

laws, such as in (Canić, 2002; Matos et al., 2015). In Lozano et al. (2022), we explore three possibilities for these simplifications applied to the first-order kinetic model (Model A) presented above.

## A.2 FIRST-ORDER KINETIC MODEL

The base of this study is Model A, presented in Section **2.4.1**. However, we analyze the model using the original relative permeability, capillary pressure, and parameter definitions proposed by its authors Ashoori et al. (2011). The relative permeability functions are based on the Brooks and Corey (1966), adjusted to experimental data (Zhou and Rossen, 1995; Persoff et al., 1991):

$$k_{rw}(S_w) = \begin{cases} 0 & , \quad 0 \leq S_w \leq S_{wc} \\ 0.20 \left( \dfrac{S_w - S_{wc}}{1 - S_{wc} - S_{gr}} \right)^{4.2} & , \quad S_{wc} < S_w \leq 1 \end{cases} , \tag{A.1}$$

$$k^0_{rg}(S_w) = \begin{cases} 0.94 \left( \dfrac{1 - S_w - S_{gr}}{1 - S_{wc} - S_{gr}} \right)^{1.3} & , \quad 0 \leq S_w < 1 - S_{gr} \\ 0 & , \quad 1 - S_{gr} \leq S_w \leq 1 \end{cases} . \tag{A.2}$$

Capillary pressure function is defined as:

$$P_c(S_w) = \sigma_{wg} \sqrt{\frac{\phi}{k}}\, 0.022 \frac{(1 - S_w - S_{gr})^c}{S_w - S_{wc}} \quad \text{e} \quad c = 0.01 \,, \tag{A.3}$$

where $\sigma_{wg}$ represents the interfacial tension between water and gas, and $c$ is a parameter used to ensure continuity of $P_c$ near $S_w = S_{wc}$.

Parameters, as defined by Ashoori et al. (2011), are presented in Table A.1.

Table A.1 – Parameter values for the foam displacement model Ashoori et al. (2011).

| Symbol | Parameter | Value |
|---|---|---|
| $S_{wc}$ | Connate water saturation | 0.2 |
| $S_{gr}$ | Residual gas saturation | 0.18 |
| $\mu_w$ | Water viscosity | $1 \cdot 10^{-3}$ Pa s |
| $\mu_g^0$ | Gas viscosity in absence of foam | $2 \cdot 10^{-5}$ Pa s |
| $k$ | Permeability of the medium | $1 \cdot 10^{-12}$ m$^2$ |
| $\phi$ | Porosity of the medium | 0.25 |
| $u$ | Total superficial velocity | $2.93 \cdot 10^{-5}$ m s$^{-1}$ |
| $n_{\max}$ | Maximum foam texture | $8 \cdot 10^{13}$ m$^{-3}$ |
| $\sigma_{wg}$ | Water/gas superficial tension | 0.03 N/m |
| $S_w^*$ | Limiting water saturation | 0.37 |
| $A$ | Foam parameter in the model | 400 |

### A.2.1 Adimensionalization of the model

To study capillary diffusion, we rewrite the system (3.1) for Model A in the dimensionless form:

$$\begin{cases} \dfrac{\partial S_w}{\partial \tilde{t}} + \dfrac{\partial f_w}{\partial \tilde{x}} &= -\dfrac{\partial}{\partial \tilde{x}}\left(\psi f_w \lambda_{rg} \dfrac{\mathrm{d}P_c}{\mathrm{d}\tilde{x}}\right), \\ \dfrac{\partial}{\partial \tilde{t}}(S_g n_D) + \dfrac{\partial}{\partial \tilde{x}}(f_g n_D) &= \dfrac{\partial}{\partial \tilde{x}}\left(\psi\, f_w \lambda_{rg} \dfrac{\mathrm{d}P_c}{\mathrm{d}\tilde{x}} n_D\right) + S_g \tilde{\Phi}\,, \end{cases} \tag{A.4}$$

with

$$\tilde{x} = \frac{x}{L}\,, \qquad \tilde{t} = \frac{ut}{L\phi}\,, \qquad \psi = \frac{k}{u\,L}\,, \quad \tilde{\Phi} = \mathcal{K}_c(n_D^{\mathrm{LE}} - n_D)\,, \quad \text{and} \quad \mathcal{K}_c = \frac{K_c L \phi}{u}\,. \tag{A.5}$$

From now on we omit the tildes in $\tilde{x}$, $\tilde{t}$, and $\tilde{\Phi}$.

### A.2.2 Simplification of diffusion

The simplifications we analyze involve approximating one or both of the following functions as constants:

$$\epsilon_w(S_w, n_D) := -\psi\, \lambda_{rg}\, f_w\, \frac{\mathrm{d}P_c}{\mathrm{d}S_w}\,, \quad \epsilon_g(S_w, n_D) := -\psi\, \lambda_{rg}\, f_w\, \frac{\mathrm{d}P_c}{\mathrm{d}S_w} n_D\,. \tag{A.6}$$

In these cases, we assume a constant value of $\epsilon = 10^{-4}$, based on the typical magnitude that the functions in (A.6) reach for a range of $S_w$ when $n_D$ is in local equilibrium.

### A.2.3 Simplification 1 ($\epsilon = \epsilon_w$, $\epsilon_g = 0$)

Simplification 1 assumes constant diffusion in the water mass balance equation and neglects diffusion in the foam balance equation. The motivation for this simplification

arises from the fact that bubbles are significantly larger than water or gas molecules. Therefore, the diffusion phenomenon, as it occurs in liquid mixtures, does not have the same effect on gas-phase foams. Thus, we can consider the diffusion rate $\epsilon_g$ of the foam to be zero. By adopting $\epsilon_g = 0$ and $\epsilon = \epsilon_w$ for the non-dimensional model (A.4), we obtain:

$$\begin{cases} \dfrac{\partial S_w}{\partial t} + \dfrac{\partial f_w}{\partial x} &= \epsilon \dfrac{\partial^2 S_w}{\partial x^2}\,, \\ \dfrac{\partial}{\partial t}(S_g n_D) + \dfrac{\partial}{\partial x}(f_g n_D) &= S_g \Phi\,. \end{cases} \tag{A.7}$$

Following a procedure similar to presented in Section 3.2, we obtain the traveling wave formulation for Simplification 1:

$$\begin{cases} \dfrac{\mathrm{d}S_w}{\mathrm{d}\eta} = H\,, \\ \dfrac{\mathrm{d}n_D}{\mathrm{d}\eta} = \dfrac{\left(\frac{\partial f_w}{\partial S_w} - v\right) H\, n_D + S_g \Phi}{M}\,, \end{cases} \tag{A.8}$$

where:

$$H(S_w, n_D) = \frac{f_w - f_w^+ - v(S_w - S_w^+)}{\epsilon} \quad \text{and} \quad M(S_w, n_D) = f_g^+ - v S_g^+ - \frac{\partial f_w}{\partial n_D} n_D\,. \tag{A.9}$$

### A.2.4 Simplification 2 ($\epsilon = \epsilon_w = \epsilon_g$)

Simplification 2 assumes constant and equal diffusion in both balance equations, *i.e.*, $\epsilon = \epsilon_w = \epsilon_g$:

$$\begin{cases} \dfrac{\partial S_w}{\partial t} + \dfrac{\partial f_w}{\partial x} &= \epsilon \dfrac{\partial^2 S_w}{\partial x^2}\,, \\ \dfrac{\partial}{\partial t}(S_g n_D) + \dfrac{\partial}{\partial x}(f_g n_D) &= \epsilon \dfrac{\partial^2 n_D}{\partial x^2} + S_g \Phi\,. \end{cases} \tag{A.10}$$

The traveling wave system of ODEs is formulated similarly as before; however, the resulting ODE is of second order. Thus, we define the auxiliary function $Z(S_w, n_D) = \frac{dn_D}{d\eta}$ to transform the system into three first-order ODEs:

$$\begin{cases} \dfrac{\mathrm{d}S_w}{\mathrm{d}\eta} = H\,, \\ \dfrac{\mathrm{d}n_D}{\mathrm{d}\eta} = Z\,, \\ \dfrac{\mathrm{d}Z}{\mathrm{d}\eta} = \dfrac{ZM - \left(\frac{\partial f_w}{\partial S_w} - v\right) H\, n_D - S_g \Phi}{\epsilon}\,. \end{cases} \tag{A.11}$$

The traveling wave solution for Simplification 2 lays in a three-dimensional phase space; see details in Lozano et al. (2022).

### A.2.5 Simplification 3 ($\epsilon = \epsilon_w$ e $\epsilon_g = n_D\epsilon_w$)

Simplification 3 considers a constant value for $\epsilon_w = \epsilon$ and define $\epsilon_g = n_D\epsilon_w$, based on Eq. (A.6). This approach is inspired by similar simplifications in the literature (Johansen and Winther, 1988). By applying this simplification to the dimensionless model (A.4), we obtain the third simplification:

$$\begin{cases} \dfrac{\partial S_w}{\partial t} + \dfrac{\partial f_w}{\partial x} = \epsilon \dfrac{\partial^2 S_w}{\partial x^2}, \\ \dfrac{\partial}{\partial t}(S_g n_D) + \dfrac{\partial}{\partial x}(f_g n_D) = -\epsilon \dfrac{\partial}{\partial x}\left(n_D \dfrac{\partial S_w}{\partial x}\right) + S_g \Phi \,. \end{cases} \tag{A.12}$$

Developing the traveling wave ODEs in a similar way to previous simplifications, we obtain the system:

$$\begin{cases} \dfrac{\mathrm{d}S_w}{\mathrm{d}\eta} = H \,, \\ \dfrac{\mathrm{d}n_D}{\mathrm{d}\eta} = \dfrac{S_g \Phi}{f_g^+ - v S_g^+ + \epsilon H} \,. \end{cases} \tag{A.13}$$

### A.2.6 Comparing simplifications

We derived the semi-analytical solution for the traveling wave ODEs of Model A (3.9)-(3.10) and its three simplifications (A.8), (A.11), and (A.13), using the following boundary conditions:

$$\begin{cases} S_w^- = 0.372 \,, \qquad S_w^+ = 0.72 \,, \\ n_D^- = 0.664 \,, \qquad n_D^+ = 1 \,. \end{cases} \tag{A.14}$$

We validated these solutions through direct numerical simulations of the corresponding PDEs, and the results agreed – see details in (Lozano et al., 2022).

Figure A.2 presents the simulations of these three simplifications and the original Model A, proposed by Ashoori et al. (2011). The simulations show that all models have the same propagation velocity for the traveling wave. It is noteworthy that simplifications 1 and 2 exhibit a sharp decrease in foam texture $n_D$ in the region where water saturation shock occurs. This phenomenon, often attributed to numerical approximation errors (Rossen, 2013; Farajzadeh et al., 2016), can also be observed as a physical result in local equilibrium foam population balance models (Kam et al., 2007; Kovscek et al., 1995). In our case, we observe this phenomenon as a semi-analytical solution of the model. Figure A.3 presents the numerical profiles of bubble density ($S_g \cdot n_D$) and apparent viscosity ($\mu_{\text{app}}$) corresponding to the simulations in Fig.A.2. In all model simulations, a peak in bubble density and apparent viscosity appears near the foam front, consistent with the experimental findings of Chen et al. (2010) and our semi-analytical and numerical observations in Chapters 3 and 5.

Figure A.2 – Numerical solution profiles for different kinetic models corresponding to a Riemann problem with $\mathcal{K}_c = 1$, for the Riemann problem (A.14). All profiles present oscillations before the traveling wave. After it simplifications 1 and 2 present a significant drop in the foam texture $n_D$. All traveling wave speeds are equal.

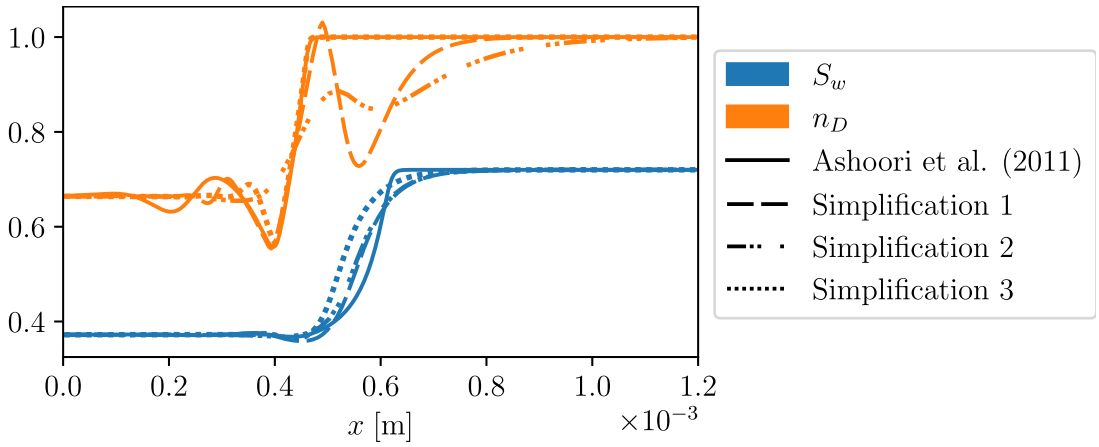


Source: Elaborated by the author (2022).

In the presented example, the original model and its simplifications demonstrate oscillations in their profiles. The oscillations are more prominent in the foam texture $n_D$ compared to the water saturation $S_w$. It is important to emphasize that directly measuring the foam texture within the core is not feasible in coreflooding experiments. Consequently, observing oscillations in $n_D$ becomes challenging in laboratory experiments. From the perspective of foam texture modeling, it is not trivial to determine which model is more suitable to describe the behavior of foam within the core. However, the water saturation profiles $S_w$ exhibit nearly identical behavior across all models. In summary, the original model and its simplifications can be considered equivalent for validating experimentally obtained saturation profiles.

## A.3 DISCUSSION

In the context of fluid displacement in porous media, the simplification or neglect of capillary pressure is a common practice in analytical estimates. We studied the impact of these simplifications in the analysis of one-dimensional incompressible two-phase gas-liquid flow in the presence of foam within a porous medium. We investigate the implications of these simplifications, particularly in the context of traveling wave analysis.

We examine three simplifications and identify two physically valid ones that result in solutions with qualitatively inaccurate foam texture profiles. These profiles deviate from those obtained using the complete original model. Additionally, we propose a simplification procedure that leads to a simplified model capable of approximating solutions with qualitative accuracy, as demonstrated in Figure A.3.

Figure A.3 – Profiles of bubble density ($S_g \cdot n_D$) and foam apparent viscosity ($\mu_{\text{app}}$) corresponding to simulations in Fig. A.2.

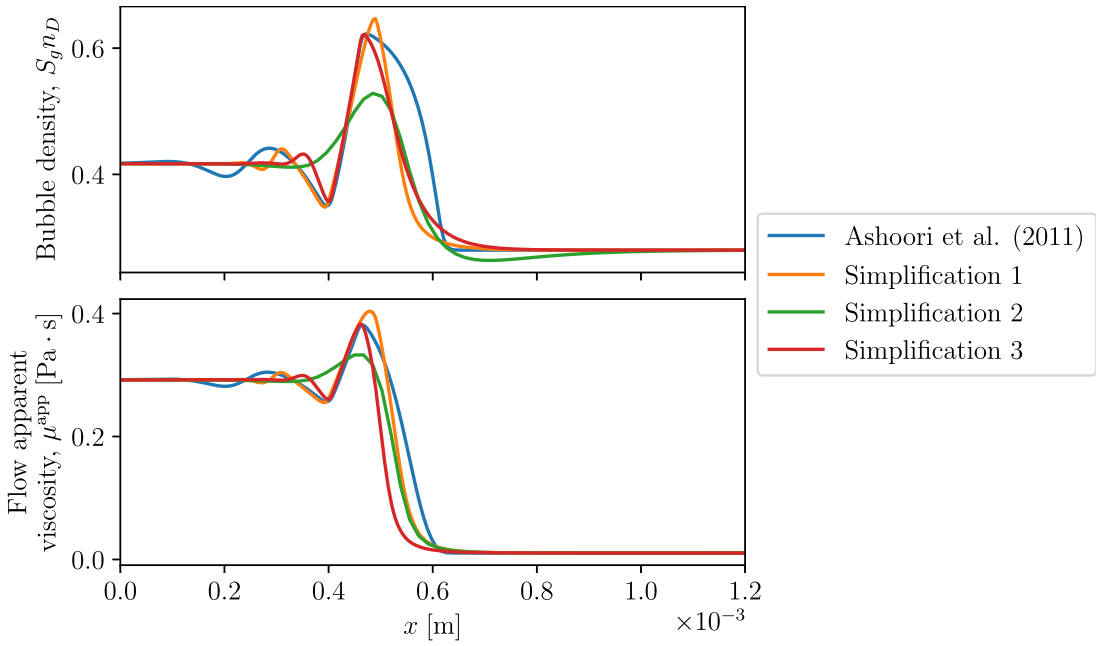


Source: Elaborated by the author (2025).

From a physical perspective, even when capillary forces have minimal impact on foam displacement in porous media, the resulting foam texture profile along the traveling front may exhibit changes. This raises the question of whether such changes can be observed in laboratory experiments.

It is worth noting that the traveling wave velocity remains constant in all simplifications, and the differences in solution profiles are attributed to the system's dynamic behavior in the phase space. The traveling wave solutions were obtained through numerical integration and analytical techniques. In all examples, the same set of parameters was used, and the injection (left state) condition exhibited oscillatory solution behavior.

# APPENDIX B – NUMERICAL METHODOLOGY

In this appendix, we present the numerical simulators employed to study the foam models introduced in Chapter 2.2. Two in-house software, RCD (Lambert et al., 2020) and FOSSIL (de Paula et al., 2020), were used to perform two types of simulations. RCD was employed for one-dimensional simulations with constant permeability, porosity, and total velocity to investigate traveling wave solutions we present in Chapter 3. FOSSIL was used for two-dimensional simulations, supporting the study of bubble density distribution in heterogeneous porous media presented in Chapter 5. The numerical schemes implemented in these simulators are briefly outlined in the following sections and further detailed in the literature Lambert et al. (2020); de Paula et al. (2020)

## B.1 REACTION-CONVECTION-DIFFUSION SIMULATOR – RCD

The Reaction-Convection-Diffusion simulator (RCD) (see Lambert et al. (2020) for details) implements a finite difference scheme to solve the following system of equations:

$$\frac{\partial}{\partial t}\mathbf{G}(\mathbf{U}) + \frac{\partial}{\partial x}\mathbf{F}(\mathbf{U}) = \frac{\partial}{\partial x}\left(\mathbf{B}(\mathbf{U})\frac{\partial \mathbf{U}}{\partial x}\right) + \mathbf{R}(\mathbf{U})\,, \tag{B.1}$$

where $\mathbf{U} \in \mathbb{R}^d$ represents the $d$ variables of the problem, and functions $\mathbf{G}, \mathbf{F}, \mathbf{R} : \mathbb{R}^d \to \mathbb{R}^d$, $\mathbf{B} : \mathbb{R}^d \to \mathbb{R}^{d\times d}$ denote the accumulation, convection, reaction, and diffusive terms, respectively. These functions have the following discretization schemes:

$$\frac{\partial \mathbf{G}}{\partial t} \approx \frac{\mathbf{G}_m^{n+1} - \mathbf{G}_m^n}{\Delta t}\,, \tag{B.2}$$

$$\begin{cases} \dfrac{\partial \mathbf{F}}{\partial x} \approx \alpha \tilde{\mathbf{F}}_m^{n+1} + (1-\alpha)\tilde{\mathbf{F}}_m^n\,, \\ \tilde{\mathbf{F}}_m = \dfrac{\mathbf{F}_{m+1} - \mathbf{F}_{m-1}}{2\Delta x}\,, \end{cases} \tag{B.3}$$

$$\begin{cases} \dfrac{\partial}{\partial x}\left(\mathbf{B}\dfrac{\partial \mathbf{U}}{\partial x}\right) \approx \alpha \tilde{\mathbf{B}}_m^{n+1} + (1-\alpha)\tilde{\mathbf{B}}_m^n\,, \\ \tilde{\mathbf{B}}_m = \dfrac{(\mathbf{B}_{m+1} + \mathbf{B}_m)(\mathbf{U}_{m+1} - \mathbf{U}_m) - (\mathbf{B}_m + \mathbf{B}_{m-1})(\mathbf{U}_m - \mathbf{U}_{m-1})}{2\Delta x^2}\,, \end{cases} \tag{B.4}$$

$$\mathbf{R} \approx \alpha \mathbf{R}_m^{n+1} + (1-\alpha)\mathbf{R}_m^n\,. \tag{B.5}$$

The indices $m$ and $n$ refer to the spatial and temporal discretizations, respectively, and $\Delta x$ and $\Delta t$ represent the spatial and temporal step sizes. Notice that the temporal discretization is fully implicit for $\alpha = 1$ and explicit for $\alpha = 0$. In this work, we adopt $\alpha = 1/2$, which is also known as the Crank-Nicolson scheme (see Crank and Nicolson (1947); LeVeque (2002)).

By substituting (B.2)-(B.5) into (B.1) and grouping the implicit and explicit terms into $\mathbb{F}$ and $\mathbb{Y}$, respectively, we obtain:

$$\underbrace{\frac{\mathbf{G}_m^{n+1}}{\Delta t} + \frac{\alpha}{2\Delta x}(\mathbf{F}_{m+1}^{n+1} - \mathbf{F}_{m-1}^{n+1}) + \dots}_{\mathbb{F}_m(\mathbf{U}_{m-1}^{n+1}, \mathbf{U}_m^{n+1}, \mathbf{U}_{m+1}^{n+1})} = \underbrace{\frac{\mathbf{G}_m^{n}}{\Delta t} + \frac{\alpha - 1}{2\Delta x}(\mathbf{F}_{m+1}^{n} - \mathbf{F}_{m-1}^{n}) + \dots}_{\mathbb{Y}_m(\mathbf{U}^n)} \tag{B.6}$$

For each meshpoint $m$, we define:

$$\mathbb{G}_m = \mathbb{F}_m - \mathbb{Y}_m = 0 \tag{B.7}$$

and numerically find the solution of the global system $\mathbb{G}(\mathbf{U}^{n+1}) = 0$. Since $\mathbf{G}$, $\mathbf{F}$, $\mathbf{B}$, and $\mathbf{R}$ are nonlinear functions, we obtain the roots of $\mathbb{G}$ using the Newton-Raphson method.

Taking the foam flow system (3.1), we substitute the partial velocities from (2.16), assuming a constant total velocity $u$ and considering $P_c$ as a function of $S_w$, allowing us to express the model in an extensive form:

$$\begin{cases} \dfrac{\partial S_w}{\partial t} + \dfrac{u}{\phi}\dfrac{\partial f_w}{\partial x} = -\dfrac{k}{\phi}\dfrac{\partial}{\partial x}\left(\left(f_w \dfrac{k_{rg}}{\mu_g}\dfrac{\mathrm{d}P_c}{\mathrm{d}S_w}\right)\dfrac{\partial S_w}{\partial x}\right), \\ \dfrac{\partial}{\partial t}(S_g n_D) + \dfrac{u}{\phi}\dfrac{\partial}{\partial x}(f_g n_D) = \dfrac{k}{\phi}\dfrac{\partial}{\partial x}\left(\left(f_w \dfrac{k_{rg}}{\mu_g}\dfrac{\mathrm{d}P_c}{\mathrm{d}S_w} n_D\right)\dfrac{\partial S_w}{\partial x}\right) + S_g\Phi\,. \end{cases} \tag{B.8}$$

The system above fits the general form given in Eq. (B.1) with the following matrices:

$$\mathbf{U} = \begin{bmatrix} S_w \\ n_D \end{bmatrix}, \quad \mathbf{G}(\mathbf{U}) = \begin{bmatrix} S_w \\ S_g n_D \end{bmatrix}, \quad \mathbf{F}(\mathbf{U}) = \frac{u}{\phi}\begin{bmatrix} f_w \\ f_g n_D \end{bmatrix}, \quad \mathbf{R}(\mathbf{U}) = \begin{bmatrix} 0 \\ S_g\Phi \end{bmatrix}, \tag{B.9}$$
$$\mathbf{B}(\mathbf{U}) = \frac{k}{\phi} f_w \frac{k_{rg}}{\mu_g}\frac{\mathrm{d}P_c}{\mathrm{d}S_w}\begin{bmatrix} -1 & 0 \\ n_D & 0 \end{bmatrix}.$$

## B.2 FOAM DISPLACEMENT SIMULATOR – FOSSIL

We perform two-dimensional numerical simulations of foam models presented in Section 2.4 by employing the in-house simulator named FOSSIL (de Paula et al., 2020, 2023). The numerical methodology of FOSSIL follows a staggered technique, employing a hybrid finite element method to solve the elliptic problem (2.19) at a fixed time and a high-order finite volume method to address the hyperbolic equations (2.20)-(2.21) for constant total velocity and pressure. Additional details regarding the numerical methodology are presented by de Paula et al. (2020, 2023).

### B.2.1 Hydrodynamic subsystem

The hydrodynamic equations describe the flow of foam in porous media using Darcy's law and the incompressibility condition:

$$\mathbf{u} = -\mathbf{k}\lambda\nabla p\,, \qquad \nabla\cdot\mathbf{u} = 0\,, \tag{B.10}$$

where $\mathbf{u}$ is the velocity field, $p$ is the global pressure, k is the permeability tensor, and $\lambda$ is the total mobility, which depends on fluids and foam properties. To deal with phase pressures, the simulator incorporates global pressure $p$ as a new variable to replace the gas and water pressure variables ($p_{\mathrm{g}}$ and $p_{\mathrm{w}}$). This variable $P$ allows the total water-gas flow to be expressed in terms of $\lambda(S_w, n_D)$, $\mathbf{u}$, and $p$ alone. This reduces the number of unknowns in the hydrodynamic problem to two: the global pressure $p$ and the total Darcy velocity $\mathbf{u}$. We can define global pressure $p$ mathematically as (Chavent and Jaffré, 1986; Chen and Ewing, 1997; de Paula et al., 2020):

$$p = \frac{1}{2}\left(p_{\mathrm{w}} + p_{\mathrm{g}}\right) + \gamma\left(S_w, n_D\right), \tag{B.11}$$

where the function $\gamma\left(S_w, n_D\right)$ is based on (Daripa and Dutta, 2017) and given by

$$\gamma\left(S_w, n_D\right) = \int_{1-S_{gr}}^{S_w}\left(\frac{1}{2} - f_w\right)\frac{\mathrm{d}P_c}{\mathrm{d}s}\mathrm{d}s + \int_{\Omega}\psi^{n_D}\left(\frac{\partial n_D}{\partial x}\mathrm{d}x + \frac{\partial n_D}{\partial y}\mathrm{d}y\right), \tag{B.12}$$

with

$$\psi^{n_D} = \int_{1-S_{gr}}^{S_w}\frac{\partial f_w}{\partial n_D}\frac{\mathrm{d}P_c}{\mathrm{d}s}\mathrm{d}s\,. \tag{B.13}$$

Physically, global pressure is defined as the pressure that drives the flow of a specific fluid (with mobility $\lambda$) in relation to the combined flow of water and gas, each with their respective mobilities (Chavent and Jaffré, 1986). To solve the hydrodynamic system (B.10), FOSSIL employs the Hybrid Mixed Finite Element Method introduced by Raviart and Thomas (1977). This method provides naturally stable approximation spaces and facilitates the use of locally conservative methods for transport equations, such as the finite volume method described below. The weak formulation for (B.10) is:

$$\begin{aligned}
&\sum_{K\in\Omega}\left[\int_K A\mathbf{u}_h\cdot\mathbf{v}_h\mathrm{d}\mathbf{x} - \int_K p_h\nabla\cdot\mathbf{v}_h\mathrm{d}\mathbf{x} + \int_{\partial K}\hat{p}_h\mathbf{v}_h\cdot\mathbf{n}_K\mathrm{d}s - \int_K q_h\nabla\cdot\mathbf{u}_h\mathrm{d}\mathbf{x}\right] = 0,\\
&\sum_{K\in\Omega}\int_{\partial K}\hat{q}_h\,\mathbf{u}_h\cdot\mathbf{n}_K\mathrm{d}s = \int_{\Gamma_N}\hat{q}_h\,\bar{u}\mathrm{d}s,
\end{aligned} \tag{B.14}$$

where $A = (\mathbf{k}\lambda)^{-1}$; the subindex $h$ indicates functions belonging to an approximation space; $\hat{p}$ represents a Lagrange multiplier that enforces pressure continuity at the interfaces; $\mathbf{v}_h$, $q_h$, and $\hat{q}_h$ are the test functions corresponding to $\mathbf{u}_h$, $p_h$, and $\hat{p}_h$; $\Omega$ and $K$ denote the problem domain and its elements, respectively; $\Gamma_N$ is the boundary region subject to a Neumann condition, where the velocity is prescribed as $\bar{u}$.

The domain is represented using an unstructured grid, $\Omega$, where continuity at element interfaces, $\partial K$, is enforced through Lagrange multipliers, $\hat{p}_h$. This approach enables FOSSIL to apply static condensation to the weak formulation (B.14), solving only for the multipliers globally while approximating the primary variables, velocity, and global pressure locally within each element $K$. By focusing on $\hat{p}_h$, the computational cost of solving the global system of equations is significantly reduced, as it avoids solving directly for $\mathbf{u}_h$ and $p_h$. Additionally, this method facilitates parallelism, as evaluating local unknowns $\mathbf{u}_h$ and $p_h$ using $\hat{p}_h$ can be done independently for each element. Solving Eq. (B.14) for $\mathbf{u}_h$ and $p_h$ yields approximations for global pressure $p$ and total Darcy velocity $\mathbf{u}$ at a fixed time.

The implementation of the finite element method is built using the deal.II library (Arndt et al., 2020), which provides a comprehensive framework for developing finite element applications. This library offers robust tools for managing grid structures, defining function spaces, and implementing linear and nonlinear solvers. Additionally, deal.II supports parallel computing, ensuring scalability for large-scale problems, and includes efficient utilities for data handling and post-processing.

### B.2.2 Transport subsystem

The transport subsystem models foam flow is governed by:

$$\phi\frac{\partial \mathbf{U}}{\partial t} + \nabla\cdot\mathbf{F} = \nabla\cdot(\mathbf{B}\nabla\mathbf{U}) + \mathbf{R}, \tag{B.15}$$

where, for the general foam model described in Section 2.3, these matrices are given by:

$$\mathbf{U} = \begin{bmatrix} S_w \\ S_g n_D \end{bmatrix}, \quad \mathbf{F} = \begin{bmatrix} f_w \mathbf{u} \\ f_g n_D \mathbf{u} \end{bmatrix}, \quad \mathbf{R} = \begin{bmatrix} 0 \\ S_g \Phi \end{bmatrix}, \quad \mathbf{B} = \mathbf{k} f_w \frac{k_{rg}}{\mu_g}\frac{\mathrm{d}P_c}{\mathrm{d}S_w}\begin{bmatrix} -1 & 0 \\ n_D & 0 \end{bmatrix}. \tag{B.16}$$

Notice that (B.16) is a general form of the system of equations (B.9) which RCD solves in the one-dimensional homogeneous case.

FOSSIL implements the conservative central-upwind scheme Kurganov-Noelle-Petrova (KNP) (Kurganov et al., 2001), suitable for stability and handling sharp solutions. The finite volume discretization for a cell $l$ is:

$$\phi\frac{\partial \mathbf{U}}{\partial t} + \frac{\mathbf{H}^x_{l+1/2} - \mathbf{H}^x_{l-1/2}}{\Delta x} + \frac{\mathbf{H}^y_{l+1/2} - \mathbf{H}^y_{l-1/2}}{\Delta y} = \frac{\mathbf{P}^x_l}{\Delta x^2} + \frac{\mathbf{P}^y_l}{\Delta y^2} + \mathbf{R}_l\,. \tag{B.17}$$

where $\mathbf{H}_{l\pm1/2}$ is numerical flux at the interface $l \pm 1/2$ and $\mathbf{P}_l$ is the diffusive numerical flux at cell $l$. The upper index $x$ and $y$ represent the direction of the cell's flux. The numerical flux is given by:

$$\mathbf{H}_{l\pm1/2} = \left(\frac{a^+\mathbf{F}^- - a^-\mathbf{F}^+ + a^+a^-(\mathbf{U}^+ - \mathbf{U}^-)}{a^+ - a^-}\right)_{l\pm1/2}, \tag{B.18}$$

where $a^+$ and $a^-$ are the interface's maximum and minimum wave speeds. The diffusive numerical fluxes $\mathbf{P}_l$ are given by:

$$\mathbf{P}_l = \mathbf{B}_{l+1}\mathbf{U}_{l+1} - (\mathbf{B}_{l+1} + \mathbf{B}_l)\mathbf{U}_l + \mathbf{B}_l\mathbf{U}_{l-1}\,. \tag{B.19}$$

The ODE in (B.17) is solved numerically using the Backward Differentiation Formula (BDF), an implicit multistep method particularly suited for stiff differential equations (Curtiss and Hirschfelder, 1952). BDF methods excel in maintaining stability for problems where rapid changes in solution components could lead to numerical instabilities. The nonlinear system generated by BDF is solved using the Newton-Raphson method. FOSSIL incorporated the BDF implementation available in the CVODE package from the SUNDIALS library (Hindmarsh et al., 2019).

# APPENDIX C – SOLVING THE FOAM TEXTURE ODE FOR MODEL B

Substituting (2.29) into (5.7) we obtain the ODE:

$$\begin{cases} \dfrac{\mathrm{d}n_D}{\mathrm{d}t} = \Phi(n_D) = \dfrac{k_1^0}{n_{\max}} \left(1 - n_D^3\right) \|\mathbf{v}_w\| \, \|\mathbf{v}_g\|^{\frac{1}{3}} - k_{-1}^0 \left(\dfrac{P_c}{P_c^* - P_c}\right)^2 \|\mathbf{v}_g\| \, n_D \,, \\ n_D(0) = 0 \,, \end{cases} \tag{C.1}$$

which can be written, for simplicity, as:

$$n'(t) = an^3 + bn + c \equiv \Phi(n) \,, \quad n(0) = 0 \,, \tag{C.2}$$

where the main variable is redefined as $n = n_D$ and the constants are

$$a = -\frac{k_1^0}{n_{\max}} \|\mathbf{v}_w\| \, \|\mathbf{v}_g\|^{\frac{1}{3}} \,, \quad b = -k_{-1}^0 \left(\frac{P_c}{P_c^* - P_c}\right)^2 \|\mathbf{v}_g\| \,, \quad \text{and} \quad c = -a \,. \tag{C.3}$$

Equation (C.2) is a separable ODE rewritten as

$$\int \frac{1}{\Phi(n)} \, \mathrm{d}n = \int \mathrm{d}t \,. \tag{C.4}$$

The integral in (C.4) can be rewritten using partial fraction decomposition as:

$$\int \left(\frac{\mathcal{A}}{n - N_1} + \frac{\mathcal{B}}{n - N_2} + \frac{\mathcal{C}}{n - N_3}\right) \mathrm{d}n = \int \mathrm{d}t \,, \tag{C.5}$$

where $N_1$, $N_2$, and $N_3$ are the roots of $\Phi$, and $\mathcal{A}$, $\mathcal{B}$, and $\mathcal{C}$ are constants to be determined. After integrating (C.4) and applying the initial condition $n(0) = 0$, the result is:

$$\mathcal{A} \ln(1 - n/N_1) + \mathcal{B} \ln(1 - n/N_2) + \mathcal{C} \ln(1 - n/N_3) = t \,. \tag{C.6}$$

That exact solution of (C.2) does not provide an explicit expression for $n$ as a function of $t$, making it difficult to compare with the solution (5.8) of Model A. To address this, we approximate $\Phi$ using the first-order Taylor expansion around its real root $N$, resulting in:

$$\Phi(n) \approx \Phi(N) + \Phi'(N)(n - N) = (3aN^2 + b)(n - N) \,. \tag{C.7}$$

Substituting (C.7) into (C.4) and applying the initial condition $n(0) = 0$ results in:

$$\frac{\ln(1 - n/N)}{3aN^2 + b} \approx t \quad \Rightarrow \quad n(t) \approx N \left(1 - \exp\left\{(3aN^2 + b)\, t\right\}\right) \,. \tag{C.8}$$

Figure C.1 – Comparison between exact solution (C.6) and the approximation (C.9) for the initial value problem (C.1) with phase velocities, water saturation, and parameters presented in Section *5.1.2.1* and Table 5.1.

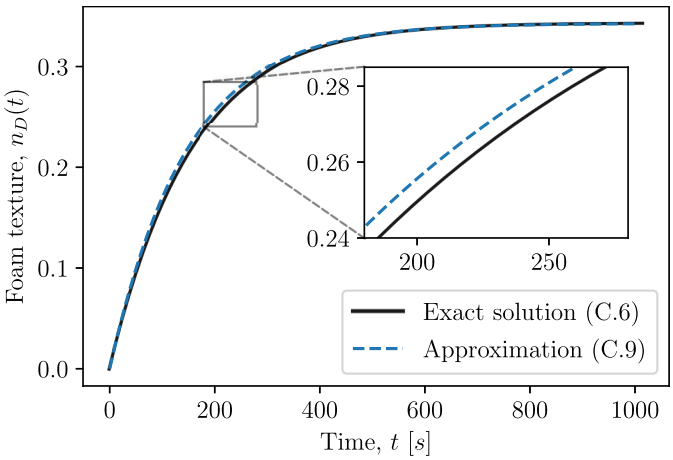


Source: Elaborated by the author (2025).

As discussed in Section **5.1.2**, Model B (2.29) features a single real root for $\Phi$, given by $N = [n_D^{\mathrm{LE}}]_{\mathrm{B}}$ in (5.4). By defining $\mathcal{K}_c = -3aN^2 - b$, we write an approximate solution for the original ODE (C.1) as:

$$\begin{cases} n_D(t) \approx [n_D^{\mathrm{LE}}]_{\mathrm{B}} \left(1 - \exp\left\{-\mathcal{K}_c\, t\right\}\right), \\ \mathcal{K}_c = \dfrac{3k_1^0}{n_{\max}} \|\mathbf{v}_w\| \, \|\mathbf{v}_g\|^{\frac{1}{3}} {[n_D^{\mathrm{LE}}]_{\mathrm{B}}}^2 + k_{-1}^0 \left(\dfrac{P_c}{P_c^* - P_c}\right)^2 \|\mathbf{v}_g\|. \end{cases} \tag{C.9}$$

Figure C.1 compares the exact solution obtained implicitly from (C.6) with the approximation (C.9). For the case shown in this figure, the relative error of the approximation in $\mathrm{L}^2$-norm is 1.13%.

Notice that substituting Model A's source term $\Phi$ (Eq. (2.26)) into Eq. (C.2) yields the coefficients $a = 0$, $b = -K_c$, and $c = K_c[n_D^{\mathrm{LE}}]_{\mathrm{A}}$. Consequently, the solution provided by Eq. (C.2) is also valid for Model A, resulting in the exact solution given in Eq. (5.8). Similarly, applying the source term of Model C (Eq. (2.30) with $K_d = 0$) to Eq. (C.2) yields the exact solution in Eq. (5.12), with $a = 0$, $b = -K_g$, and $c = K_g[n_D^{\mathrm{LE}}]_{\mathrm{C}}$.

# APPENDIX D – MODEL A'S SENSIBILITY TO LOW $S_w^*$ VALUES

Chapter 5 introduced a method for fitting the limiting water saturation $S_w^*$ in Model A based on the limiting capillary pressure $P_c^*$ of Model B, using the capillary pressure function in (2.24) – see Section *5.1.2.1*. This approach may result in $S_w^*$ being lower than the connate water saturation, *i.e.*, $S_w^* < S_{wc}$, which is the case for the parameters in Table 5.1 and the permeability fields described in Section **5.1.1**. Although we can discuss whether modeling $S_w^* < S_{wc}$ is nonphysical, this appendix demonstrates that variations in $S_w^*$ do not significantly impact Model A when the simulation's saturation range remains sufficiently far from $S_w^*$. Section **2.4.1** explains that the local equilibrium foam texture $n_D^{\mathrm{LE}}(S_w)$ is approximately zero or one, except near $S_w = S_w^*$. In the simulations presented in Section 5.2, minimum water saturation values across the entire domain are 0.5341 and 0.5064 for Fields 1 and 2, respectively. These saturation levels are sufficiently high for $n_D^{\mathrm{LE}}$ to approximate one when $S_w^* \lessapprox 0.50$. Given that this study focuses on comparing the effects of foam flow modeling on bubble distributions in heterogeneous permeability, we retained the $S_w^*$ fitting approach described in Section *5.1.2.1*, even with $S_w^* < S_{wc}$, as it does not significantly influence the results within the analyzed scenarios.

To exemplify how this range of $S_w^*$ values does not affect our observations in Chapter 5, we conducted simulations of Model A in Fields 1 and 2 using three different values of limiting water saturation: $S_w^* = 0.16 < 0.38 = S_{wc}$, $S_w^* = 0.38 = S_{wc}$, and $S_w^* = 0.50 > 0.38 = S_{wc}$. The bubble density profiles ($S_g \cdot n_D$) at 0.6 PV (after breakthrough in all cases) are depicted in Figures D.1 and D.2, with no visual difference between them. We compare these profiles quantitatively using the $L^2$-norm distance, with the results summarized in Tables D.1 and D.2. For reference, the tables also include the distances between Models B and C, whose bubble density profiles are depicted in Figures 5.4 and 5.5.

Tables D.1 and D.2 demonstrate that Model A produces nearly identical results for $S_w^*$ values of 0.16 and 0.38. A slight difference is observed when $S_w^*$ is increased to 0.50. This small deviation arises because $S_w^* = 0.50$ approaches the minimum water saturation achieved during the simulations, which is 0.5341 in Field 1 and 0.5064 in Field 2. The impact of using $S_w^* = 0.50$ is more noticeable in Field 2 due to its proximity to the minimum saturation. Additionally, the tables show that the $L^2$-distances in bubble density profiles between different $S_w^*$ cases of Model A are at least two orders of magnitude smaller

Table D.1 – $L^2$-norm distance of bubble density ($S_g \cdot n_D$) between models for simulations on Field 1 at 0.45 PV.

| | Model A ($S_w^* = 0.16$) | Model A ($S_w^* = 0.38$) | Model A ($S_w^* = 0.50$) | Model B | Model C |
|---|---|---|---|---|---|
| Model A ($S_w^* = 0.16$) | 0 | | | | |
| Model A ($S_w^* = 0.38$) | $< 10^{-15}$ | 0 | | | |
| Model A ($S_w^* = 0.50$) | $3.06 \cdot 10^{-3}$ | $3.06 \cdot 10^{-3}$ | 0 | | |
| Model B | $3.03 \cdot 10^{1}$ | $3.03 \cdot 10^{1}$ | $3.03 \cdot 10^{1}$ | 0 | |
| Model C | $1.29 \cdot 10^{0}$ | $1.29 \cdot 10^{0}$ | $1.29 \cdot 10^{0}$ | $3.05 \cdot 10^{1}$ | 0 |

Table D.2 – $L^2$-norm distance of bubble density ($S_g \cdot n_D$) between models for simulations on Field 2 at 0.5 PV.

| | Model A ($S_w^* = 0.16$) | Model A ($S_w^* = 0.38$) | Model A ($S_w^* = 0.50$) | Model B | Model C |
|---|---|---|---|---|---|
| Model A ($S_w^* = 0.16$) | 0 | | | | |
| Model A ($S_w^* = 0.38$) | $< 10^{-15}$ | 0 | | | |
| Model A ($S_w^* = 0.50$) | $4.03 \cdot 10^{-1}$ | $4.03 \cdot 10^{-1}$ | 0 | | |
| Model B | $1.16 \cdot 10^{1}$ | $1.16 \cdot 10^{1}$ | $1.15 \cdot 10^{1}$ | 0 | |
| Model C | $3.50 \cdot 10^{0}$ | $3.50 \cdot 10^{0}$ | $3.59 \cdot 10^{0}$ | $1.19 \cdot 10^{1}$ | 0 |

than those between Models A and B and one order smaller than between A and C. The differences between all models are more pronounced in Field 1, as one can see by comparing Figures 5.4 and 5.5.

Figure D.1 – Comparison of foam behavior of Models A for some values of $S_w^*$ in Field 1 at 0.45 PV.

(a) Bubble density $S_g \cdot n_D$ predicted by Model A ($S_w^* = 0.16$) for Field 1.

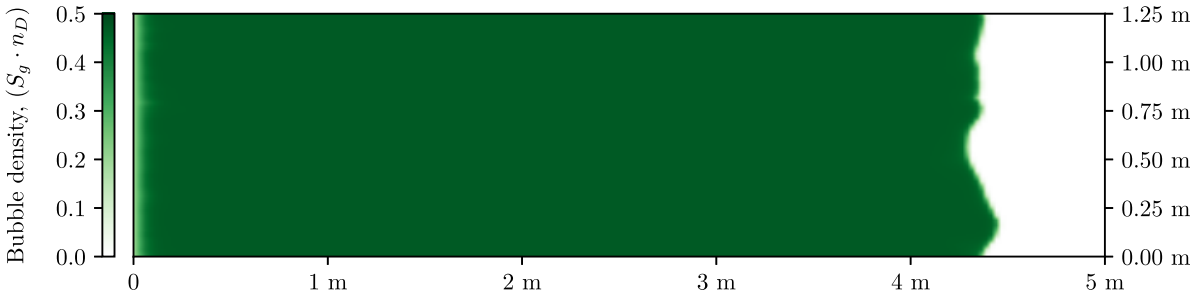


(b) Bubble density $S_g \cdot n_D$ predicted by Model A ($S_w^* = 0.38$) for Field 1.

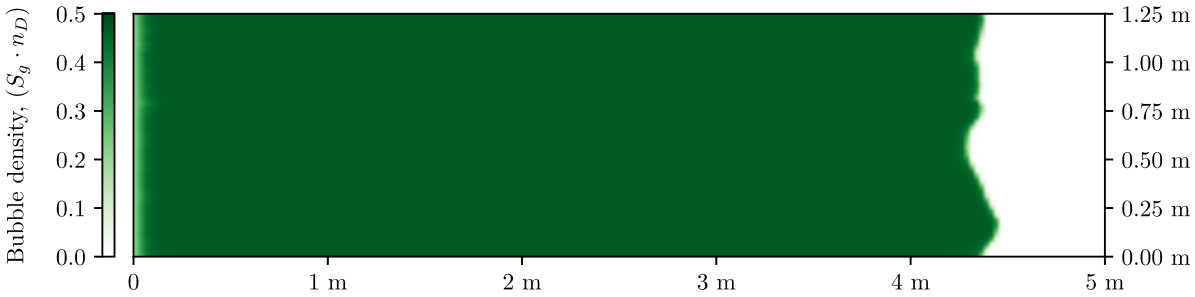


(c) Bubble density $S_g \cdot n_D$ predicted by Model A ($S_w^* = 0.50$) for Field 1.

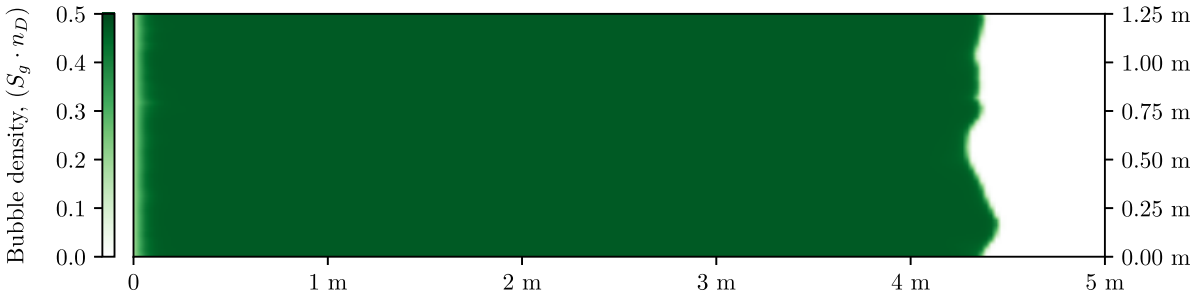


Source: Elaborated by the author (2025).

Figure D.2 – Comparison of foam behavior of Models A for some values of $S_w^*$ in Field 2 at 0.5 PV.

(a) Bubble density $S_g \cdot n_D$ predicted by Model A ($S_w^* = 0.16$) for Field 2.

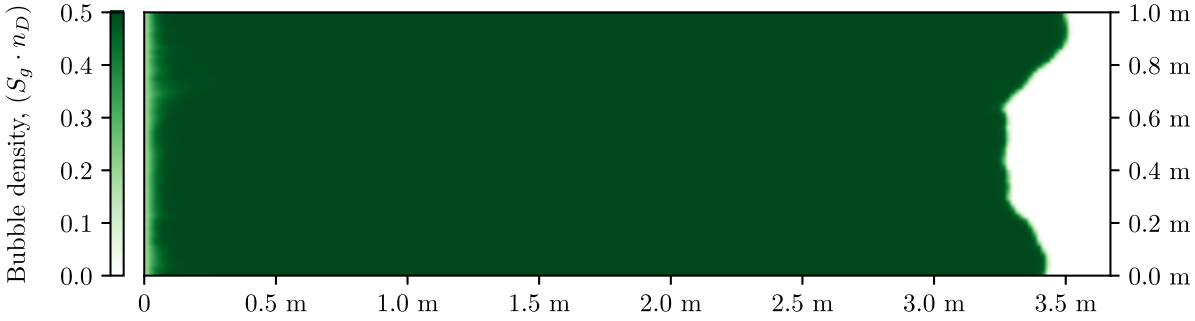


(b) Bubble density $S_g \cdot n_D$ predicted by Model A ($S_w^* = 0.38$) for Field 2.

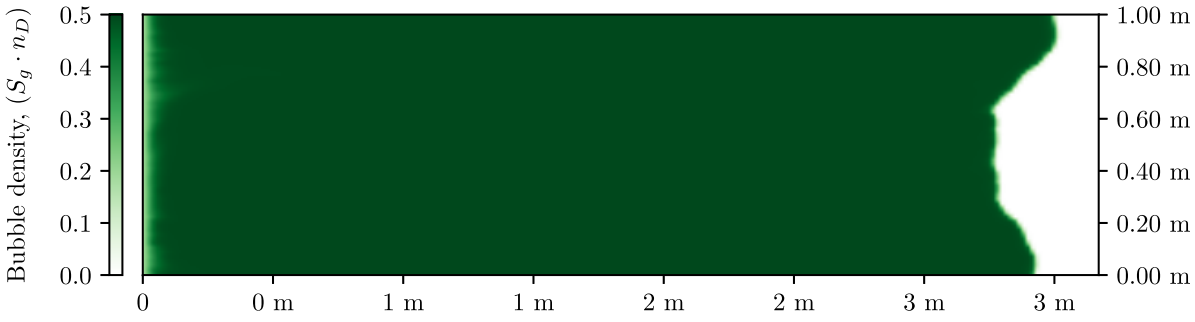


(c) Bubble density $S_g \cdot n_D$ predicted by Model A ($S_w^* = 0.50$) for Field 2.

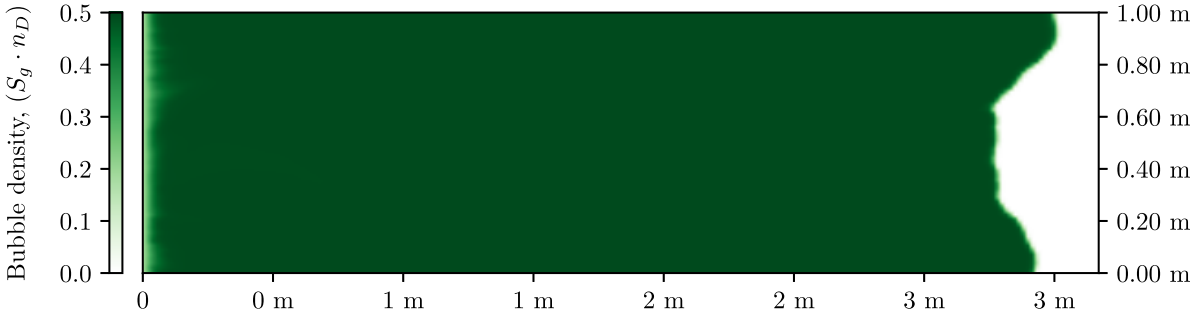


Source: Elaborated by the author (2025).

# REFERENCES


Abdelgawad, K. Z., Adebayo, A. R., Isah, A., and Muhammed, N. S. (2022). A literature review of strength and stability of foam and their relationship with the absolute permeability of porous media. *Journal of Petroleum Science and Engineering*, 211:110195.

Abernethy, E. R. (1976). Production increase of heavy oils by electromagnetic heating. *Journal of Canadian Petroleum Technology*, 15(03).

Afsharpoor, A., Lee, G. S., and Kam, S. I. (2010). Mechanistic simulation of continuous gas injection period during surfactant-alternating-gas (sag) processes using foam catastrophe theory. *Chemical Engineering Science*, 65(11):3615–3631.

Alvarez, J. M., Rivas, H. J., and Rossen, W. R. (2001). Unified model for steady-state foam behavior at high and low foam qualities. *SPE Journal*, 6(3):325–333.

Arndt, D., Bangerth, W., Blais, B., Clevenger, T. C., Fehling, M., Grayver, A. V., Heister, T., Heltai, L., Kronbichler, M., Maier, M., Munch, P., Pelteret, J.-P., Rastak, R., Thomas, I., Turcksin, B., Wang, Z., and Wells, D. (2020). The `deal.II` library, version 9.2. *Journal of Numerical Mathematics*. in press.

Ashoori, E., Marchesin, D., and Rossen, W. R. (2011). Roles of transient and local equilibrium foam behavior in porous media: traveling wave. *Colloids and Surfaces A: Physicochemical and Engineering Aspects*, 377:228–242.

Barenblatt, G. I., Entov, V. M., and Ryzhik, V. M. (1989). *Theory of fluid flows through natural rocks*, volume 395. Springer.

Bear, J. (2018). *Modeling Phenomena of Flow and Transport in Porous Media*. Theory and Applications of Transport in Porous Media. Springer International Publishing.

Bedrikovetsky, P. (1993). *Mathematical theory of oil and gas recovery*, volume 4 of *Petroleum Engineering and Development Studies*. Springer Science & Business Media, Dordrecht.

Bertin, H. J., Quintard, M. Y., and Castanier, L. M. (1998). Development of a bubble-population correlation for foam-flow modeling in porous media. *SPE Journal*, 3(04):356–362.

Bikerman, J. J. (1973). *Foams*. Applied Physics and Engineering, v. 10. Springer-Verlag, New York.

Boeije, C. S. and Rossen, W. R. (2015). Fitting foam-simulation-model parameters to data: I. Coinjection of gas and liquid. *SPE Reservoir Evaluation & Engineering*, 18(02):264–272.

Bretherton, F. P. (1961). The motion of long bubbles in tubes. *Journal of Fluid Mechanics*, 10(2):166–188.

Brooks, R. H. and Corey, A. T. (1964). *Hydraulic Properties of Porous Media*. Colorado State University Hydrology Paper. Colorado State University.

Brooks, R. H. and Corey, A. T. (1966). Properties of porous media affecting fluid flow. *Journal of the Irrigation and Drainage Division*, 92(2):61–90.

Bruining, H. (2021). *Upscaling of Single- and Two-Phase Flow in Reservoir Engineering*. CRC Press.

Bruining, J. and Van Duijn, C. (2000). Uniqueness conditions in a hyperbolic model for oil recovery by steamdrive. *Computational Geosciences*, 4(1):65–98.

Buckley, S. E. and Leverett, M. C. (1942). Mechanism of fluid displacement in sands. *Transactions of the AIME*, 146.

Canić, S. (2002). Nonexistence of riemann solutions for a quadratic model deriving from petroleum engineering. *Nonlinear analysis: real world applications*, 3(4):629–665.

Cassie, A. B. D. and Baxter, S. (1944). Wettability of porous surfaces. *Transactions of the Faraday society*, 40:546–551.

Cedro, J. B. and Chapiro, G. (2022). Numerical observation of traveling wave solution in a non-newtonian foam model. In *XLIII Ibero-Latin-American Congress on Computational Methods in Engineering (CILAMCE)*, Foz do Iguaçu, Brazil.

Cedro, J. B. and Chapiro, G. (2024). Traveling wave solutions for a realistic non-newtonian foam flow model. *Geoenergy Science and Engineering*, 232:212478.

Cedro, J. B., de Paula, F. F., and Chapiro, G. (2025). On the modeling of the foam dynamics in heterogeneous porous media. *Advances in Water Resources*, 196:104882.

Cedro, J. B., Quispe, R. V., Coaquira, M. C., Lozano, L. F., and Chapiro, G. (2019). Estudo de um modelo cinético para escoamento de espuma em meios porosos. In *XL Ibero-Latin-American Congress on Computational Methods in Engineering (CILAMCE)*, Natal, Brazil.

Chapiro, G. and Bruining, J. (2015). Combustion enhance recovery of shale gas. *Journal of Petroleum Science and Engineering*, 127:179–189.

Chapiro, G. and Lozano, L. (2022). Analytical solution for the population-balance model describing foam displacement considering surfactant dispersion. In *ECMOR 2022*, volume 2022, pages 1–12. European Association of Geoscientists & Engineers.

Chapiro, G., Mailybaev, A. A., Souza, A., Marchesin, D., and Bruining, J. (2012). Asymptotic approximation of long-time solution for low-temperature filtration combustion. *Computational Geosciences*, 16:799–808.

Chavent, G. and Jaffré, J. (1986). *Mathematical models and finite elements for reservoir simulation: single phase, multiphase and multicomponent flows through porous media*, volume 17. North-Holland, Amsterdam.

Chen, Q., Gerritsen, M. G., and Kovscek, A. R. (2010). Modeling foam displacement with the local-equilibrium approximation: theory and experimental verification. *SPE Journal*, 15(01):171–183.

Chen, Z. and Ewing, R. E. (1997). Fully discrete finite element analysis of multiphase flow in groundwater hydrology. *SIAM J. Numer. Anal.*, 34(6):2228–2253.

Chen, Z., Huan, G., and Ma, Y. (2006). *Computational Methods for Multiphase Flows in Porous Media*. Computational Science and Engineering. Society for Industrial and Applied Mathematics.

Cheng, L., Reme, A. B., Shan, D., Coombe, D. A., and Rossen, W. R. (2000). Simulating foam processes at high and low foam qualities. volume SPE/DOE Improved Oil Recovery Symposium of *SPE Improved Oil Recovery Conference*, pages SPE–59287–MS.

Chierici, G. L. (1984). Novel relations for drainage and imbibition relative permeabilities. *Society of Petroleum Engineers Journal*, 24.

Christie, M. A. and Blunt, M. J. (2001). Tenth SPE comparative solution project: A comparison of upscaling techniques. *SPE Reservoir Evaluation & Engineering*, 4(04):308–317.

CMG, C. M. G. (2019). STARS users manual; version 2019.10.

Collins, R. E. (1976). *Flow of fluids through porous materials*. Petroleum Publishing Co., Tulsa, OK.

Conn, C. A., Ma, K., Hirasaki, G. J., and Biswal, S. L. (2014). Visualizing oil displacement with foam in a microfluidic device with permeability contrast. *Lab Chip*, 14(20):3968–3977.

Couto, H. J. B., Massarani, G., Biscaia, E. C., and Sant'Anna, G. L. (2009). Remediation of sandy soils using surfactant solutions and foams. *Journal of Hazardous Materials*, 164(2):1325–1334.

Crank, J. and Nicolson, P. (1947). A practical method for numerical evaluation of solutions of partial differential equations of the heat-conduction type. *Mathematical Proceedings of the Cambridge Philosophical Society*, 43(1):50–67.

Curtiss, C. F. and Hirschfelder, J. O. (1952). Integration of stiff equations. *Proceedings of the National Academy of Sciences of the United States of America*, 38(3):235.

Darcy, H. (1856). *Les fontaines publiques de la ville de Dijon*. Dalmont.

Daripa, P. and Dutta, S. (2017). Modeling and simulation of surfactant–polymer flooding using a new hybrid method. *Journal of Computational Physics*, 335:249–282.

DataPhysics Instruments (2020). Surfactants & critical micelle concentration (CMC). Available in: https://www.dataphysics-instruments.com/knowledge/understanding-interfaces/surfactants-cmc.

Davarzani, H., Aranda, R., Colombano, S., Laurent, F., and Bertin, H. (2021). Experimental study of foam propagation and stability in highly permeable porous media under lateral water flow: Diverting groundwater for application to soil remediation. *Journal of Contaminant Hydrology*, 243:103917.

Davarzani, H., Aranda, R., Colombano, S., Laurent, F., and Bertin, H. (2022). Modeling and monitoring of foam propagation in highly permeable porous media under lateral water flow. *Advances in Water Resources*, 166:104225.

de Paula, F. F., Igreja, I., Quinelato, T., and Chapiro, G. (2023). A numerical investigation into the influence of the surfactant injection technique on the foam flow in heterogeneous porous media. *Advances in Water Resources*, 171:104358.

de Paula, F. F., Quinelato, T., Igreja, I., and Chapiro, G. (2020). A numerical algorithm to solve the two-phase flow in porous media including foam displacement. In *Computational Science – ICCS 2020*, volume 12143, pages 18–31. Springer.

Dholkawala, Z. F., Sarma, H. K., and Kam, S. I. (2007). Application of fractional flow theory to foams in porous media. *Journal of Petroleum Science and Engineering*, 57(1-2):152–165.

Evans, D. F. and Wennerström, H. (1999). *The Colloidal Domain*. Advances in Interfacial Engineering. Wiley-VCH, USA.

Falls, A. H., Hirasaki, G. J., Patzek, T. W., Gauglitz, D. A., Miller, D. D., and Ratoulowski, T. (1988). Development of a mechanistic foam simulator: The population balance and generation by snap-off. *SPE Reservoir Engineering*, 3:884–892.

Falls, A. H., Musters, J. J., and Ratulowski, J. (1989). The apparent viscosity of foams in homogeneous bead packs. *SPE Reservoir Engineering*, 4(02):155–164.

Farajzadeh, R., Andrianov, A., Krastev, R., Hirasaki, G., and Rossen, W. R. (2012). Foam–oil interaction in porous media: implications for foam assisted enhanced oil recovery. *Advances in colloid and interface science*, 183:1–13.

Farajzadeh, R., Eftekhari, A. A., Hajibeygi, H., Kahrobaei, S., Van der Meer, J. M., Vincent-Bonnieu, S., and Rossen, W. R. (2016). Simulation of instabilities and fingering in surfactant alternating gas (sag) foam enhanced oil recovery. *Journal of Natural Gas Science and Engineering*, 34:1191–1204.

Farajzadeh, R., Lotfollahi, M., Eftekhari, A. A., Rossen, W. R., and Hirasaki, G. J. H. (2015). Effect of permeability on implicit-texture foam model parameters and the limiting capillary pressure. *Energy & Fuels*, 29(5):3011–3018.

Fejoli, R. F. and Romero, O. J. (2014). Modelagem computacional da injeção de espumas em reservatórios de petróleo. *Latin American Journal of Energy Research*, 1(1):1–9.

Fernø, M. A., Gauteplass, J., Pancharoen, M., Haugen, Å., Graue, A., Kovscek, A. R., and Hirasaki, G. (2016). Experimental study of foam generation, sweep efficiency, and flow in a fracture network. *SPE J.*, 21(4):1140–1150.

Fritis, G., Lozano, L. F., and Chapiro, G. (2022). Enhanced oil recovery analysis using foam through new analytical tools. In *Proceedings of the Rio Oil & Gas Expo and Conference*.

Gassara, O., Douarche, F., Braconnier, B., and Bourbiaux, B. (2020). Calibrating and scaling semi-empirical foam flow models for the assessment of foam-based EOR processes (in heterogeneous reservoirs). *Transport in Porous Media*, 131:193–221.

Ghazaryan, A. R., Lafortune, S., and Manukian, V. (2022). *Introduction to Traveling Waves*. CRC Press.

Guckenheimer, J. and Holmes, P. (1986). *Nonlinear Oscillations, Dynamical Systems, and Bifurcations of Vector Fields*. Springer-Verlag, New York.

Heller, J. P. and Kuntamukkula, M. S. (1987). Critical review of the foam rheology literature. *Ind. Eng. Chem. Res.*, 26(2):318–325.

Hematpur, H., Mahmood, S. M., Nasr, N. H., and Elraies, K. A. (2018). Foam flow in porous media: Concepts, models and challenges. *Journal of Natural Gas Science and Engineering*, 53:163–180.

Hindmarsh, A. C., Serban, R., and Reynolds, D. R. (2019). Cvode user guide. Technical report, Lawrence Livermore National Laboratory.

Hirasaki, G. J. (1989). A review of the steam foam process mechanisms. Paper SPE 19518.

Hirasaki, G. J. (1991). Wettability: fundamentals and surface forces. *SPE Formation Evaluation*, 6(2):217–226.

Hirasaki, G. J. and Lawson, J. B. (1985). Mechanisms of foam flow in porous media: apparent viscosity in smooth capillaries. *SPE Journal*, 25(02):176–190.

Hirasaki, G. J., Miller, C. A., Szafranski, R., Lawson, J. B., and Akiya, N. (1997). Surfactant/foam process for aquifer remediation. In *International symposium on oilfield chemistry*. Society of Petroleum Engineers.

Hou, J., Du, Q., Li, Z., Pan, G., Lu, X., and Zhou, K. (2013). Experiments on foam texture under high pressure in porous media. *Flow Measurement and Instrumentation*, 33:68–76.

Hu, J., Lan, J. W., Chen, Y. M., Xu, W. J., Meng, M., Ma, P. C., and Ke, H. (2023). Foam flow model of municipal solid waste and its application in landfill gas pressure prediction. *Journal of Geotechnical and Geoenvironmental Engineering*, 149(3):04023004.

Janssen, M. T. G., Pilus, R. M., and Zitha, P. L. J. (2020). A comparative study of gas flooding and foam-assisted chemical flooding in bentheimer sandstones. *Transport in Porous Media*, 131(1):101–134.

Johansen, T. and Winther, R. (1988). The solution of the riemann problem for a hyperbolic system of conservation laws modeling polymer flooding. *SIAM Journal on Mathematical Analysis*, 19(3):541–566.

Kam, S. I. (2008). Improved mechanistic foam simulation with foam catastrophe theory. *Colloids and Surfaces A: Physicochemical and Engineering Aspects*, 318(1):62–77.

Kam, S. I., Nguyen, Q. P., Li, Q., and Rossen, W. R. (2007). Dynamic simulations with an improved model for foam generation. *SPE Journal*, 12(1):35–48.

Kapetas, L., Vincent Bonnieu, S., Farajzadeh, R., Eftekhari, A. A., Shafian, S. R. M., Bahrim, R. Z. K., and Rossen, W. R. (2017). Effect of permeability on foam-model parameters: An integrated approach from core-flood experiments through to foam diversion calculations. *Colloids and Surfaces A: Physicochemical and Engineering Aspects*, 530:172–180.

Kendall, M. G. (1943). *The advanced theory of statistics*, volume 1. Charles Griffin and Co., Ltd., London.

Khatib, Z. I., Hirasaki, G. J., and Falls, A. H. (1988). Effects of capillary pressure on coalescence and phase mobilities in foams flowing through porous media. *SPE Reservoir Engineering*, 3(3):919–926.

Kile, D. E. and Chiou, C. T. (1989). Water solubility enhancements of DDT and trichlorobenzene by some surfactants below and above the critical micelle concentration. *Environmental Science & Technology*, 23(7):832–838.

Kovscek, A. R., Patzek, T. W., and Radke, C. J. (1995). A mechanistic population balance model for transient and steady-state foam flow in Boise sandstone. *Chemical Engineering Science*, 50(23):3783–3799.

Kovscek, A. R. and Radke, C. J. (1994). Fundamentals of foam transport in porous media. In Schramm, L. L., editor, *Foams: Fundamentals and Applications in the Petroleum Industry*, chapter 3, pages 115–163. American Chemical Society, Washington, DC.

Kurganov, A., Noelle, S., and Petrova, G. (2001). Semidiscrete central-upwind schemes for hyperbolic conservation laws and Hamilton-Jacobi equations. *SIAM Journal on Scientific Computing*, 23(3):707–740.

Lake, L. (1989). *Enhanced oil recovery*. Prentice Hall, New Jersey.

Lambert, W., Alvarez, A., Ledoino, I., Tadeu, D., Marchesin, D., and Bruining, J. (2020). Mathematics and numerics for balance partial differential-algebraic equations (PDAEs). *Journal of Scientific Computing*, 84(2):1–56.

LeVeque, R. J. (2002). *Finite volume methods for hyperbolic problems*. Cambridge University Press.

Leverett, M. C. (1941). Capillary behavior in porous solids. *Transactions of AIME*, 142(01):152–169.

Li, K., Wolf, K.-H. A. A., and Rossen, W. R. (2021). Effects of gas trapping on foam mobility in a model fracture. *Transport in Porous Media*, 138(1):185–200.

Li, S., Qiao, C., Ji, G., Wang, Q., and Tao, L. (2019). Experimental study of profile control with foam stabilized by clay particle and surfactant. *Energies*, 12(5):781.

Liontas, R., Ma, K., Hirasaki, G. J., and Biswal, S. L. (2013). Neighbor-induced bubble pinch-off: novel mechanisms of in situ foam generation in microfluidic channels. *Soft Matter*, 9(46):10971–10984.

Lomeland, F., Ebeltoft, E., and Thomas, W. H. (2005). A new versatile relative permeability correlation. In *Proceedings of the International Symposium of the Society of Core Analysts*. Paper SCA2005-32.

Lotfollahi, M., Farajzadeh, R., Delshad, M., Varavei, A., and Rossen, W. R. (2016). Comparison of implicit-texture and population-balance foam models. *Journal of Natural Gas Science and Engineering*, 31:184–197.

Lovett, S., Monmont, F., and Nikiforakis, N. (2015). An experimentally-based in-situ combustion model with adaptive meshing. *Combustion and Flame*, 162(4):960–977.

Lozano, L. F., Cedro, J. B., Zavala, R. V. Q., and Chapiro, G. (2022). How simplifying capillary effects can affect the traveling wave solution profiles of the foam flow in porous media. *International Journal of Non-Linear Mechanics*, 139:103867.

Lozano, L. F., Zavala, R. Q., and Chapiro, G. (2021). Mathematical properties of the foam flow in porous media. *Computational Geosciences*, 25(1):515–527.

Lv, M., Liu, Z., Jia, L., and Ji, C. (2020). Visualizing pore-scale foam flow in micromodels with different permeabilities. *Colloids and Surfaces A: Physicochemical and Engineering Aspects*, 600:124923.

Ma, K., Farajzadeh, R., Lopez-Salinas, J. L., Miller, C. A., Biswal, S. L., and Hirasaki, G. J. (2014a). Non-uniqueness, numerical artifacts, and parameter sensitivity in simulating steady-state and transient foam flow through porous media. *Transport in porous media*, 102(3):325–348.

Ma, K., Mateen, K., Ren, G., Luo, H., Neillo, V., Blondeau, C., Bourdarot, G., Morel, D., M'barki, O., and Nguyen, Q. (2019). Parameter estimation of a population-balance foam model using two-step multi-variable search. In *IOR 2019–20th European Symposium on Improved Oil Recovery*, pages 1–21. European Association of Geoscientists & Engineers.

Ma, K., Ren, G., Mateen, K., Morel, D., and Cordelier, P. (2014b). Literature review of modeling techniques for foam flow through porous media. In *Conference Proceedings*, Tulsa, OK. SPE Improved Oil Recovery Symposium, OnePetro.

Ma, K., Ren, G., Mateen, K., Morel, D., and Cordelier, P. (2015). Modeling techniques for foam flow in porous media. *SPE Journal*, 20(3):453–470.

Marsden, S. S. and Khan, S. A. (1966). The flow of foam through short porous media and apparent viscosity measurements. *SPE Journal*, pages 17–25.

Matos, V., Azevedo, A. V., da Mota, J. C., and Marchesin, D. (2015). Bifurcation under parameter change of riemann solutions for nonstrictly hyperbolic systems. *Zeitschrift für angewandte Mathematik und Physik*, 66(4):1413–1452.

Ministry of Mines and Energy, National Agency of Petroleum, Natural Gas and Biofuels, Pré-Sal Petróleo S.A., Energy Research Company, and National Bank for Economic and Social Development (2020). Study on the use of the pre-salt natural gas. Available in: https://www.gov.br/anp/pt-br/centrais-de-conteudo/publicacoes/livros-e-revistas/arquivos/inglesaproveitamentognpresal.pdf.

Ministry of the Environment (2020). Paris agreement. Available in: https://antigo.mma.gov.br/clima/convencao-das-nacoes-unidas/acordo-de-paris.html.

Moradi-Araghi, A., Johnston, E. L., Zornes, D. R., and Harpole, K. J. (1997). Laboratory evaluation of surfactants for CO2-foam applications at the South Cowden unit. In *SPE International Conference on Oilfield Chemistry*, volume All Days, pages SPE–37218–MS.

Mualem, Y. (1976). A new model for predicting the hydraulic conductivity of unsaturated porous media. *Water resources research*, 12(3):513–522.

Mulligan, C. N. and Eftekhari, F. (2003). Remediation with surfactant foam of PCP-contaminated soil. *Engineering Geology*, 70(3):269–279. Third British Geotechnical Society Geoenvironmental Engineering Conference.

Muskat, M. and Meres, M. W. (1936). The flow of heterogeneous fluids through porous media. *Physics*, 7(9):346–363.

Paz, P. Z. S., Hollmann, T. H., Kermen, E., Chapiro, G., Slob, E., and Zitha, P. L. J. (2017). EM heating-stimulated water flooding for medium–heavy oil recovery. *Transport in Porous Media*, 119(1):57–75.

Pereira, W. S. and Chapiro, G. (2017). Numerical validation of analytical estimates for propagation of thermal waves generated by gas-solid combustion. *Geofluids*, 2017(1):1806052.

Pereira, W. S. and Chapiro, G. (2023). Traveling wave solutions for non-newtonian foam flow in porous media. *Transport in Porous Media*, 148(2):247–265.

Persoff, P., Radke, C. J., Pruess, K., Benson, S. M., and Witherspoon, P. A. (1989). A laboratory investigation of foam flow in sandstone at elevated pressure. In *SPE California Regional Meeting*. Society of Petroleum Engineers.

Persoff, P., Radke, C. J., Pruess, K., Benson, S. M., and Witherspoon, P. A. (1991). A laboratory investigation of foam flow in sandstone at elevated pressure. *SPE Reservoir Engineering*, 6(03):365–372.

Raviart, P. A. and Thomas, J. M. (1977). A mixed finite element method for 2-nd order elliptic problems. In Galligani, I. and Magenes, E., editors, *Mathematical Aspects of Finite Element Methods*, volume 606, pages 292–315. Springer.

Rossen, W. R. (1991). Rheology of foam in porous media at the "limiting capillary pressure". In *6th European Symposium on IOR*. EAGE.

Rossen, W. R. (1996). Foams in enhanced oil recovery. In Prud'homme, R. K. and Khan, S., editors, *Foams: Theory, Measurements and Applications*, chapter 11, pages 414–464. Marcel Dekker, New York.

Rossen, W. R. (2013). Numerical challenges in foam simulation: A review. In *Proceedings - SPE Annual Technical Conference and Exhibition*. Society of Petroleum Engineers.

Rossen, W. R. and Bruining, J. (2007). Foam displacements with multiple steady states. *SPE Journal*, 12(01):5–18.

Rossen, W. R., Farajzadeh, R., Hirasaki, G. J., and Amirmoshiri, M. (2024). Potential and challenges of foam-assisted CO2 sequestration. *Geoenergy Science and Engineering*, 239:212929.

Rossen, W. R., Venkatraman, A., Johns, R. T., Kibodeaux, K. R., Lai, H., and Tehrani, N. M. (2011). Fractional flow theory applicable to non-Newtonian behavior in EOR processes. *Transport in porous media*, 89(2):213–236.

Rossen, W. R., Zeilinger, S. C., Shi, J. X., and Lim, M. T. (1999). Simplified mechanistic simulation of foam processes in porous media. *SPE Journal*, 4(03):279–287.

Rossen, W. R. and Zhou, Z. H. (1995). Modelling foam mobility at the "limiting capillary pressure". *SPE Advanced Technology Series*, 3(1):146–153.

Schlumberger (2010). Eclipse reservoir simulation software. *technical description*, 2010(2).

Shah, S. Y., As Syukri, H., Wolf, K.-H., Pilus, R. M., and Rossen, W. R. (2020). Foam generation in flow across a sharp permeability transition: Effect of velocity and fractional flow. *SPE Journal*, 25(01):451–464.

Shojaei, M. J., Or, D., and Shokri, N. (2022). Localized delivery of liquid fertilizer in coarse-textured soils using foam as carrier. *Transport in Porous Media*, 143(3):787–795.

Simjoo, M., Dong, Y., Andrianov, A., Talanana, M., and Zitha, P. L. J. (2013a). CT scan study of immiscible foam flow in porous media for enhancing oil recovery. *Industrial & Engineering Chemistry Research*, 52(18):6221–6233.

Simjoo, M., Dong, Y., Andrianov, A., Talanana, M., and Zitha, P. L. J. (2013b). Novel insight into foam mobility control. *SPE Journal*, 18(3).

Simjoo, M. and Zitha, P. L. J. (2015). Modeling of foam flow using stochastic bubble population model and experimental validation. *Transport in Porous Media*, 107(3):799–820.

Sumnu-Dindoruk, D. and Dindoruk, B. (2006). Analytical and numerical solution of nonisothermal buckley-leverett flow including tracers. volume SPE Annual Technical Conference and Exhibition, pages SPE–102266–MS.

Thorat, R. and Bruining, H. (2016). Foam flow experiments. I. Estimation of the bubble generation-coalescence function. *Transport in Porous Media*, 112(1):53–76.

Trogus, F. J., Sophany, T., Schechter, R. S., and Wade, W. H. (1977). Static and Dynamic Adsorption of Anionic and Nonionic Surfactants. *Society of Petroleum Engineers Journal*, 17(05):337–344.

United Nations Framework Convention on Climate Change (2020). The paris agreement. Available in: https://unfccc.int/process-and-meetings/the-paris-agreement.

van Genuchten, M. T. (1980). A Closed-form Equation for Predicting the Hydraulic Conductivity of Unsaturated Soils. *Soil Science Society of America Journal*, 44(5):892–898.

Vásquez, A. J. C., Lozano, L. F., Pereira, W. S., Cedro, J. B., and Chapiro, G. (2022). The traveling wavefront for foam flow in two-layer porous media. *Computational Geosciences*, 26(6):1549–1561.

Volpert, A. I., Volpert, V. A., and Volpert, V. A. (2000). *Traveling Wave Solutions of Parabolic Systems*, volume 140 of *Translations of Mathematical Monographs*. AMS.

Wang, C. and Li, H. A. (2016). Stability and mobility of foam generated by gas-solvent/surfactant mixtures under reservoir conditions. *Journal of Natural Gas Science and Engineering*, 34:366–375.

Wang, S. and Mulligan, C. N. (2004). An evaluation of surfactant foam technology in remediation of contaminated soil. *Chemosphere*, 57(9):1079–1089.

Willhite, G. P. (1967). Over-all heat transfer coefficients in steam and hot water injection wells. *Journal of Petroleum technology*, 19(05):607–615.

Willman, B., Valleroy, V. V., Runberg, G. W., Cornelius, A. J., and Powers, L. W. (1961). Laboratory studies of oil recovery by steam injection. *Journal of Petroleum Technology*, 13(07):681–690.

Zavala, R. Q., Lozano, L. F., and Chapiro, G. (2024). Traveling wave solutions describing the foam flow in porous media for low surfactant concentration. *Computational Geosciences*, 28(2):323–340.

Zavala, R. Q., Lozano, L. F., Zitha, P. L. J., and Chapiro, G. (2022). Analytical solution for the population-balance model describing foam displacement. *Transport in Porous Media*, 144(1):211–227.

Zeng, Y., Kamarul Bahrim, R. Z., Groot, J. A. W. M., Vincent-Bonnieu, S., Groenenboom, J., Mohd Shafian, S. R., Abdul Manap, A. A., Tewari, R. D., Mohammadian, E., Azdarpour, A., Hamidi, H., and Biswal, S. L. (2020). Probing methane foam transport in heterogeneous porous media: An experimental and numerical case study of permeability-dependent rheology and fluid diversion at field scale. *SPE Journal*, 25(04):1697–1710.

Zhang, Z. F., Freedman, V. L., and Zhong, L. (2009). Foam transport in porous media – A review. Technical report, Pacific Northwest National Lab. (PNNL), Richland, WA.

Zhou, Z. and Rossen, W. R. (1995). Applying fractional-flow theory to foam processes at the "limiting capillary pressure". *SPE Advanced Technology Series*, 3(01):154–162.

Zitha, P. L. J. and Du, D. X. (2010). A new stochastic bubble population model for foam flow in porous media. *Transport in Porous Media*, 83(3):603–621.

Zitha, P. L. J., Du, D. X., Uijttenhout, M., and Nguyen, Q. P. (2006). Numerical analysis of a new stochastic bubble population foam model. In *SPE/DOE Symposium on Improved oil recovery*. Society of Petroleum Engineers.